

Copyright © 2002, by the author(s).
All rights reserved.

Permission to make digital or hard copies of all or part of this work for personal or classroom use is granted without fee provided that copies are not made or distributed for profit or commercial advantage and that copies bear this notice and the full citation on the first page. To copy otherwise, to republish, to post on servers or to redistribute to lists, requires prior specific permission.

**COMPREHENSIVE MODEL FOR PROJECTION
PHOTOLITHOGRAPHY: RIGOROUS, FAST
AND NOVEL PROCESSING**

by

Mosong Cheng

Memorandum No. UCB/ERL M02/1

29 January 2002

**COMPREHENSIVE MODEL FOR PROJECTION
PHOTOLITHOGRAPHY: RIGOROUS, FAST
AND NOVEL PROCESSING**

by

Mosong Cheng

Memorandum No. UCB/ERL M02/1

29 December 2002

ELECTRONICS RESEARCH LABORATORY

College of Engineering
University of California, Berkeley
94720

**Comprehensive Model for Projection Photolithography: Rigorous, Fast and Novel
Processing**

Copyright © 2002

by

Mosong Cheng

Comprehensive Model for Projection Photolithography: Rigorous, Fast and Novel

Processing

By

Mosong Cheng

B.S. (University of Science and Technology of China) 1997

A dissertation submitted in partial satisfaction of the requirement for the degree of

Doctor of Philosophy

In

Engineering – Electrical Engineering and Computer Sciences

In the

GRADUATE DIVISION

Of the

University of California, Berkeley

Committee in charge:

Professor Andrew R. Neureuther, Chair

Professor Avidesh Zakhor

Professor Raymond Chiao

Spring 2002

Abstract

Comprehensive Model for Projection Photolithography: Rigorous, Fast and Novel

Processing

By

Mosong Cheng

Doctor of Philosophy in Engineering – Electrical Engineering and Computer Sciences

University of California, Berkeley

Professor Andrew R. Neureuther, Chair

The central theme of this thesis is comprehensively modeling projection photolithography and identifying how process factors such as the mask, lens and resist impact the lithographic resolution. In addition, a novel electric-field enhanced post exposure bake process that improves resolution is introduced. First a methodology of modeling line-end shortening (LES) effects in KrF 248nm resists is described, which combines optics and resist post exposure bake (PEB) simulation and matches the experimental data to better than 10% of the nominal linewidth. The results show that LES in KrF resists results from optical proximity and acid diffusion. Then a fast algorithm is developed for solving the non-linear partial differential equations in resist reaction/diffusion. Using high order partial differential expansion, this algorithm achieves a time step 100 times larger than the Finite Difference Method and is more than 10 times faster than Finite Element Method. An image processing algorithm is also developed which retrieves the physically fine contours of patterns from noisy Scanning Electron Microscope (SEM) pictures. Then contours are compared with those from simulation to effectively extract the model parameters.

A main contribution of the thesis is the extension of the comprehensive model using a divide-and-conquer strategy to ArF lithography of 120nm critical dimension (CD) with the emerging exposure tools and resists. Extensive linewidth measurements and SEMs were made at Texas Instruments and merged with data on lens aberrations and resist models from SEMATECH. For the 100nm node, when adjusting for mask error, the model fit through dose, focus and feature types and size (DFS) CDs within 5% for lines and matched the SEM areas of 2D patterns within 15%. The most important factors were image position in the resist and threshold. A strong DFS variation for the low light intensity images of small gaps was observed. Adding trajectory dissolution model allowed the gap prediction error of 25nm over 80 DFS cases. This error is large but reasonable given that the SEM LES error in 193nm resists is greater than 10nm.

This thesis also presents a novel electric-field-enhanced post exposure bake technique which uses alternating electric field to aggressively modify or control the profile of photoresist. In PEB process the presence of an alternating field leads to an order of magnitude greater arc length of the proton in the preferred direction than in the unwanted lateral directions. In experiments a resist profile improvement effect was clearly observed and the resist resolution was significantly improved. This technique is of practical interest and a patent application was filed by the University of California.

Professor Andrew R. Neureuther

Committee Chairman

Table of Contents

1	<u>Introduction</u>	1
2	<u>Methodology of Modeling Line-End Shortening Effect in KrF Resists</u>	9
2.1	<u>Introduction</u>	9
2.2	<u>Post Exposure Bake Model for Deep-UV Resist</u>	10
2.3	<u>Extraction of PEB Parameters</u>	11
2.4	<u>Simulation Process of Exposure and Post Exposure Bake</u>	14
2.5	<u>Process Optimization and Parameter Extraction</u>	16
2.6	<u>Compare Simulation with Experiment</u>	17
2.7	<u>A Quick Approach to Predict Line-End Shortening in the Presence of Lens Imperfections</u>	27
2.8	<u>Application of Image in Resist Approach to Different Scanners</u>	29
2.9	<u>Conclusion</u>	33
3	<u>Fast Algorithm for Simulating Post Exposure Baking Process</u>	35
3.1	<u>Introduction</u>	35
3.2	<u>Post Exposure Bake Model</u>	36
3.3	<u>Fast Algorithm to Solve Partial Differential Equations</u>	37
3.4	<u>Generalization of the Algorithm</u>	45
3.5	<u>Implementation of Post Exposure Bake Simulator with the Algorithm</u>	48
3.6	<u>Performance Comparison of RIAR and STORM</u>	50
3.7	<u>Application of RIAR in Line-End Shortening Simulations</u>	57
3.8	<u>Conclusions</u>	59
4	<u>Automatic Resist Parameter Extraction by Pattern Matching</u>	60

4.1	<u>Introduction</u>	60
4.2	<u>Concept of Pattern Matching</u>	62
4.3	<u>Converting SEM Pictures to Monochromatic</u>	64
4.4	<u>SEM/SIM Comparator and Model Tuner</u>	67
4.5	<u>Conclusions</u>	71
5	<u>Modeling Projection Lithography through Resist Simulation and Pattern Matching</u>	72
5.1	<u>Introduction</u>	72
5.2	<u>Experimental Setup</u>	77
5.3	<u>Simulation Setup</u>	80
5.4	<u>Identifying Imaging Location in Resist</u>	81
5.5	<u>Simulating Linewidths in the Presence of Lens Aberrations</u>	89
5.6	<u>Analysis of Experimental and Simulated Images</u>	92
5.7	<u>Analysis of PEB Models</u>	102
5.8	<u>Analysis of Dissolution Model</u>	104
5.9	<u>Conclusions</u>	110
6	<u>Electric-Field-Enhanced Post Exposure Bake Technique: Theory and Simulation</u>	113
6.1	<u>Introduction</u>	113
6.2	<u>Post Exposure Bake Model</u>	114
6.3	<u>Rigorous Solution to Electric-Field-Enhanced Post Exposure Bake Model</u> ..	117
6.4	<u>Numerical Picture of Electric-Field-Enhanced Post Exposure Bake</u>	124
6.5	<u>The Role of Alternating Field in EFE-PEB</u>	129

7	<u>Electric-Field-Enhanced Post Exposure Bake Technique: Experiment</u>	134
7.1	<u>Introduction</u>	134
7.2	<u>Experiment Setup in Electron-Beam Lithography</u>	135
7.3	<u>Experiment Results and Analysis</u>	136
7.4	<u>Experiments of the Impact of Field Polarity in Electron Beam Lithography</u> .	144
7.5	<u>Experimental Results and Analysis</u>	145
7.6	<u>Experiments in KrF Lithography</u>	151
7.7	<u>Experimental Results in KrF Lithography</u>	152
7.8	<u>Conclusions</u>	155
8	<u>Conclusions</u>	156
8.1	<u>Summary</u>	156
8.2	<u>Improvements and Extensions of Lithography Modeling</u>	160
	Bibliography161

List of Figures

<u>Figure 2-1</u>	<u>Schematic of experimental procedure for broad area exposure data collection</u>	12
<u>Figure 2-2</u>	<u>Schematic of top-to-top contact experiment</u>	13
<u>Figure 2-3</u>	<u>Schematic of exposure and PEB simulation</u>	15
<u>Figure 2-4</u>	<u>An example of LES simulation</u>	15
<u>Figure 2-5</u>	<u>Simulation vs experiment for APEX-E, feature A, elbow</u>	21
<u>Figure 2-6</u>	<u>Simulation vs. experiment for APEX-E, feature B, end at line</u>	22
<u>Figure 2-7</u>	<u>Simulation vs. experiment for APEX-E, feature C, post in square</u>	23
<u>Figure 2-8</u>	<u>Simulation vs. experiment for APEX-E, feature D, post</u>	24
<u>Figure 2-9</u>	<u>Simulation vs. experiment for UVIIHS, feature A, elbow</u>	25
<u>Figure 2-10</u>	<u>Simulation vs. experiment for UVIIHS, feature D, post</u>	26
<u>Figure 2-11</u>	<u>The calculation of line-end shortening</u>	30
<u>Figure 2-12</u>	<u>Line-end shortening simulations vs. experiments of dense lines</u>	31
<u>Figure 2-13</u>	<u>Line-end shortening simulations vs. experiments of isolated lines</u>	32
<u>Figure 4-1</u>	<u>The diagram of SEM/SIM comparator</u>	64
<u>Figure 4-2</u>	<u>The process of extracting black/white representations from SEM pictures</u>	69
<u>Figure 4-3</u>	<u>Overlaying SEM with simulated image</u>	70
<u>Figure 4-4</u>	<u>The framework for tuning models based on minimizing IMF</u>	70
<u>Figure 5-1</u>	<u>D11H, the mask pattern used for calibrating simulation models</u>	79
<u>Figure 5-2</u>	<u>D18H, the mask pattern used for verification of simulation models</u>	79
<u>Figure 5-3</u>	<u>Wafer CD vs. pitch</u>	82

<u>Figure 5-4</u>	<u>Simulated light intensity of 130nm line in resist</u>	82
<u>Figure 5-5</u>	<u>Mask CD vs. pitch</u>	83
<u>Figure 5-6</u>	<u>Linewidths vs. defocus at 350nm pitch</u>	83
<u>Figure 5-7</u>	<u>Light intensity of 140nm line at 350nm pitch</u>	84
<u>Figure 5-8</u>	<u>Simulated linewidths vs. defocus at 350nm pitch</u>	86
<u>Figure 5-9</u>	<u>Diagram of a 1X exposure/resist system</u>	87
<u>Figure 5-10</u>	<u>Simulated linewidth vs. defocus at 350nm pitch, aberrations included</u>	90
<u>Figure 5-11</u>	<u>Experimental and simulated linewidth vs. defocus at 350nm and 1750nm pitch, lens aberrations included</u>	91
<u>Figure 5-12</u>	<u>SEM pictures of D11H exposed at 9.5mJ/cm²</u>	93
<u>Figure 5-13</u>	<u>The monochromatic representations of the SEM pictures of D11H exposed at 9.5mJ/cm²</u>	94
<u>Figure 5-14</u>	<u>The experimental line-end spacing of D11H</u>	95
<u>Figure 5-15</u>	<u>The smoothed line-end spacing of D11H</u>	96
<u>Figure 5-16</u>	<u>Overlay of simulated and experimental images</u>	98
<u>Figure 5-17</u>	<u>The simulated line-end spacing of D11H</u>	99
<u>Figure 5-18</u>	<u>Light intensity across lines and line-end gaps</u>	101
<u>Figure 5-19</u>	<u>The line-end spacing of D11H simulated with PEB model</u>	102
<u>Figure 5-20</u>	<u>The linewidths simulated by PEB model</u>	103
<u>Figure 5-21</u>	<u>The correlation of threshold acid concentration with peak acid intensity and acid intensity slope</u>	105
<u>Figure 5-22</u>	<u>Dissolution rate of PAR710 vs. normalized activated site concentration</u>	107
<u>Figure 5-23</u>	<u>Comparing experiment with simulation using Dissolution model</u>	110

<u>Figure 6-1</u>	<u>Chemical reactions of resist in exposure and PEB.</u>	115
<u>Figure 6-2</u>	<u>Principle of electric-field-enhanced post-exposure baking.</u>	116
<u>Figure 6-3</u>	<u>The coordinate system used in solving EFE-PEB model.</u>	118
<u>Figure 6-4</u>	<u>An example of acid distribution profile.</u>	125
<u>Figure 6-5</u>	<u>Acid distribution after standard PEB.</u>	127
<u>Figure 6-6</u>	<u>Acid distribution after EFE-PEB, $V=0.2V$ or $E=3.310^5$ V/m.</u>	128
<u>Figure 6-7</u>	<u>Acid distribution after EFE-PEB, $V=0.3V$ or $E=5.010^5$ V/m.</u>	128
<u>Figure 6-8</u>	<u>The acid lateral diffusion after standard PEB and 0.2V EFE-PEB.</u>	129
<u>Figure 6-9</u>	<u>One-dimensional EFE-PEB model.</u>	130
<u>Figure 7-1</u>	<u>The setup of electric-field-enhanced PEB.</u>	135
<u>Figure 7-2</u>	<u>Comparison of EFE-PEB and Standard PEB for 0.5μm L/S, dose</u> <u>20μC/cm².</u>	139
<u>Figure 7-3</u>	<u>Comparison of EFE-PEB and Standard PEB for 0.1μm L/S, dose 9μC/cm²</u>	140
<u>Figure 7-4</u>	<u>Comparison of EFE-PEB and Standard PEB for 0.2μm L/S, dose 9μC/cm²</u>	141
<u>Figure 7-5</u>	<u>Comparison of EFE-PEB and standard PEB for 0.3μm L/S, dose 9μC/cm²</u>	142
<u>Figure 7-6</u>	<u>Comparison of EFE-PEB and Standard PEB for 0.5μm L/S, dose</u> <u>15μC/cm².</u>	143
<u>Figure 7-7</u>	<u>Comparison of upward/downward EFE-PEB and Standard PEB for 0.3,</u> <u>0.2 and 0.1 μm L/S, dose 12μC/cm².</u>	147

<u>Figure 7-8</u>	<u>Comparison of EFE-PEB and Standard PEB for 0.2μm L/S, dose 9μC/cm²</u>	148
<u>Figure 7-9</u>	<u>Comparison of EFE-PEB and Standard PEB for 0.3μm L/S, dose 9μC/cm²</u>	149
<u>Figure 7-10</u>	<u>Comparison of EFE-PEB for 0.2μm L/S, dose 16μC/cm²</u>	150
<u>Figure 7-11</u>	<u>Comparison of EFE-PEB and Standard PEB in DUV lithography, 0.4μm</u> <u>L/S, dose 27mJ/cm²</u>	153
<u>Figure 7-12</u>	<u>Comparison of upward EFE-PEB and Standard PEB in DUV lithography,</u> <u>0.4μm L/S, dose 27mJ/cm²</u>	154

List of Tables

<u>Table 2-1</u>	<u>Reaction/Diffusion parameters for APEX-E and UVIIHS</u>	14
<u>Table 2-2</u>	<u>Reaction/Diffusion/Threshold parameters for APEX-E and UVIIHS</u>	17
<u>Table 2-3</u>	<u>The error analysis of simulations versus experiments for APEX-E</u>	20
<u>Table 2-4</u>	<u>The error analysis of simulations vs. experiments for UVIIHS</u>	20
<u>Table 5-1</u>	<u>Measured CDs on the mask</u>	78
<u>Table 5-2</u>	<u>IMFs of the simulations applied to two patterns</u>	97
<u>Table 7-1</u>	<u>Line/Space values from EFE-PEB and standard PEB (unit: nm)</u>	138

1 Introduction

Optical lithography has been a key enabling technology for the miniaturization of semiconductor devices. This has been made possible by the use of shorter wavelengths of light to pattern submicron features. At each move towards a shorter wavelength, new lens, exposure tools and resist materials are developed. With the semiconductor device dimension shrinking below the exposure wavelength, Resolution Enhancement Techniques (RET) are playing a more and more important role in integrated circuit (IC) manufacturing, since they offer viable extensions of optical lithography tools for future generations of ICs.

During the optical lithography step in IC manufacturing, a mask pattern comprised of dark and clear areas is transferred to the photoresist on the wafer surface through the use of imaging optics. Resist chemistry as well as underlying film types will affect the final resist profile on the wafer. Because of the complexities associated with this mask/lens/resist system, modeling has been used extensively to investigate the effects of different operating parameters. Modeling and simulation is also useful for understanding factors responsible for various issues associated with the implementation of advanced lithography processes and emerging technologies. Semiconductor process simulators including COMPOSITE [1], SAMPLE [2], DEPICT [3], PROLITH [4], SOLID-C [5] and SUPREM [6] have become important tools in process development and optimization. Given the reduction in cost of computation and increase in cost of experimentation trend,

process simulators will continue to provide a cost effective means of understanding physical aspects of processing steps to allow for process optimization.

The most difficult aspect of modeling advanced lithography processes at one point was the formidable difficulty in emulating the complex optical diffraction of high-NA lens or reaction state dependent transport that occurs in the post exposure bake (PEB) process of chemically amplified resists (CARs). In the PEB process, for example, the model-equations result in a system of highly nonlinear partial differential equations (PDEs) that degrade the performance of numerical methods severely. With the many advances on simulators, including work at University of California, Berkeley, by Phil Flanner, Kenny Toh, David Newmark, Derek Lee on SPLAT [7][8], Marco Zuniga [9], Ebo Croffie [10] and Lei Yuan on STORM [11], the computational complexity of lithography simulation is becoming a secondary concern. The major difficulty arises from the calibration of models and identification of process factors that limit the pattern transfer quality. Particularly, with the rapid progress of sub-wavelength lithography, all aspects of the lithography process are becoming limiting factors of printing resolution. Besides diffraction limited imaging, mask accuracy, lens imperfection, imaging location, resist optics, photoacid diffusion and resist dissolution all have big impacts on pattern formation. To model these effects physically means to develop a predictive model for each effect and then integrate these models to predict the final resist patterns. Decoupling the complexities brought forth by these entangled factors presents a formidable challenge. The central theme of this thesis is to address these complexities through divide-and-conquer strategy.

This thesis begins by discussing a methodology for modeling line-end shortening (LES) effects in 248nm resists. The fact that 248nm resists have been well developed simplified the LES modeling work and nevertheless provides a base for understanding much more complicated 193nm imaging process. Using SPLAT, STORM and a threshold activated site concentration model, the LES in APEX-E and UVIIHS resists is successfully predicted in this thesis with error less than 10% of nominal linewidth. The resist PEB parameters are also effectively extracted in the process of fitting simulated LES with experimental data though Method of Feasible Direction (MFD) [12].

Then in this thesis, the high nonlinearity of PDEs used to describe the PEB of CARs is addressed through a fast algorithm that is a modification of Finite Difference Method (FDM). A new algorithm is introduced that uses high order partial differential expansion to represent unknown functions in PDE so this allows a much larger time step than in FDM and ends of simulating by an order of magnitude faster than FEM. The algorithm was implemented in RIAR, which stands for Rapid Imaging Algorithm for Resist [14]. With this rapid PEB simulation capability, the incorporation of CAR simulation into model parameter extraction, physical process verification and optical proximity correction (OPC) becomes feasible.

One of the main contributions of this thesis is to use the pattern fidelity in 2D to evaluate the effectiveness of simulation models and/or extract the model parameters. Traditionally, a 1-dimensional metric, critical dimension (CD), is used to evaluate the lithography performance as well as the effectiveness of simulation models. Also, CD control is the primary concern of lithographers and reticle designers who rely heavily on OPC software for sub-wavelength printing capability. With the increasing demand of printing sub-

200nm random logic devices, however, the 1-D CD metric is becoming less adequate. The control of pattern fidelity, which is a 2-dimensional metric, is becoming more and more important to ensure IC yield and performance. To facilitate direct comparison of SEMs and simulations, an image processing algorithm was developed which retrieves the physically fine contours of patterns from noisy SEM pictures, and then computes the difference of the extracted contours with those simulated by a given model. By fine tuning the parameters to minimize the difference between experimental and simulated contours, the model parameters can be effectively and efficiently extracted. This approach is essential to 2-dimensional calibration of models.

A systematic divide-and-conquer strategy with fast simulation capability and image matching algorithm is presented in this thesis to comprehensively model 193nm lithography, in which lens design and resist properties are not as mature as 248nm lithography. The experimental work were done in summer 2000 and summer 2001 at Texas Instruments (TI). Based on the enormous amount of experimental data and SEM pictures obtained at TI and resist parameters from International SEMATECH, the main process factors were identified individually. These factors affecting printing quality include mask accuracy, choice of imaging imaging focal plane, lens aberrations, resist PEB process and resist dissolution mechanism. Practically, the SEM measurement error is also not negligible in calibrating models due to the large LER and resist slimming [15]. In this divide-and-conquer strategy, the actual mask CDs were measured and incorporated in all simulations to eliminate the mask error effect. It is found that the unexpected isolated-dense line bias is mostly determined by mask CD variations. Then by inspecting the CD vs. defocus curves of isolated and dense lines, the location of focal

plane in the resist can be determined. When adding lens aberrations measured by Litel in-situ technique at Texas Instruments [16], it was found that the actual focal plane location was 0.1mm lower than calculated under the assumption of aberration-free lens. The error of simulated CDs is further reduced after including lens aberrations.

Using the measured mask CDs, lens aberrations and the imaging location found above, the light intensity in resist of lines at different defocus, different pitch and 9.5mJ/cm² dose are simulated. A threshold light intensity model was used to determine the line CDs. By fitting line CD vs. defocus simulations with experimental curves, the threshold was extracted. The Root Mean Square (RMS) of the simulation error was 5.26nm, or 5% of the smallest linewidth. Thus this single-threshold model is adequate in predicting line CDs through focus, dose and linewidths.

The calibrated single-threshold resist imaging model was further used to simulate 2-dimensional patterns. The simulated images matched the experimental SEM pictures within less than 15% error. However, the line-end gaps predicted by this model were much larger than experimental, which indicates the resist PEB or dissolution process may have big impact on opening gaps. PEB and an assumed trajectory dissolution models were tested to separately identify the impact of the two processes. In PEB model, the acid diffusivity, the deprotection rate constant and the threshold activated site concentration were tuned to determine the line-end gaps. The PEB model reduced RMS error of line-end gap prediction to 37nm while increase linewidth prediction error to 20%. The assumed trajectory dissolution model proposed that the dissolvability of resist at a certain location is enhanced by the maximum acid concentration in its neighborhood. While keeping the error of line width simulation within 6nm, the dissolution model reduces the

error of predicting gaps to 26nm over 80 different dose, focus and feature-type cases. Given the fact that SEM measurement error in 193nm resists is greater than 10nm, the dissolution model fit experiment fairly well. The residual error may be due to the incompleteness of dissolution simulation.

Besides the comprehensive modeling work on projection photolithography, the thesis also presents a novel resist processing technique, termed “Electric-Field-Enhanced Post Exposure Bake” (EFE-PEB), to improve resist resolution and sensitivity. This technique uses alternating electric field to aggressively modify or control the profile of photoresist. The resist material becomes soluble in reactions catalyzed by protons generated by exposure. In this process, the presence of an alternating field leads to an order of magnitude greater arc length of the proton in the preferred direction than in the unwanted lateral directions. This technique uses similar principle as electrophoresis, which uses electric field to separate nucleic acids and proteins by size and charge [17][18]. Compared with electrophoresis, the EFE-PEB technique uses electric field to enhance not only physical motion, but also chemical reaction cross-section. In experiments a resist profile improvement effect was clearly observed and the resist resolution was significantly improved. The method provides a promising solution to the problem of lack of single layer resist facing 157nm and Extreme Ultraviolet (EUV) lithography [19]. With this method, current commercial deep-UV resists could be used in 157nm and EUV lithography with little modification. A patent of this invention was filed by University of California on July 18, 2001.

This dissertation is a result of several collaboration works. The initial project leading to the work in this dissertation was the modeling line-end shortening (LES) effects in deep-

UV resists based on optics and resist simulation. Collaboration work with Texas Instruments (TI) on the investigation of LES in 248nm resists led to the conclusion that the incorporation of lens aberrations and resist optics into lithography models is needed. The advent of transparent materials at 193nm lithography directed this dissertation work to develop development of efficient chemically amplified resist simulators and pattern matching algorithm to address 193nm resist issues. Further collaboration with TI on modeling pattern fidelity in 193nm lithography provided enormous experimental data and made possible the comprehensive methodology of modeling ArF 193nm lithography based on optics/resist simulation and image calibration.

Collaboration work with Ebo Croffie and Lei Yuan on algorithm improvements of the finite element method (FEM) implementation has greatly improved the efficiency of CAR simulation. The collaborative work between University of California at Berkeley TCAD Group and Texas Instruments C035 Photo Group on modeling KrF and ArF lithography and investigating mask/lens/resist impacts motivated the modeling framework presented in this thesis and provided experimental basis to validate the modeling methodology. The modeling framework was developed in collaboration with Mark Terry, Keeho Kim, Mark Ma and Maureen Hanratty of Texas Instruments.

A general overview of pattern distortion issues in optical lithography, followed by the line-end shortening simulation and model calibration is presented in Chapter 2. This chapter also presents a quick method of predicting LES in 248nm resists by calculating image intensity inside resists. Chapter 3 presents a general purpose fast algorithm for solving non-linear PDEs used to describe the PEB process of CARs, along with numerical examples of algorithm performance. In Chapter 4, the image processing

algorithm is presented for comparing simulated images with noisy SEM pictures. By minimizing the contour difference, the simulation model parameters can be extracted. This 2-dimensional calibration framework is further employed in Chapter 5 to comprehensively model projection photolithography on the basis of mask/lens/resist simulations. The impacts such as mask variation, lens aberrations and resist deprotection/diffusion characteristic on pattern fidelities are also identified.

Chapter 6 discusses the theory of the novel technique EFE-PEB, which uses vertical alternating electric field to maintain the dominance of vertical deprotection/transportation of acid over lateral reaction. In Chapter 7, the experimental Scanning Electron Microscope (SEM) pictures of EFE-PEB and standard PEB in electron-beam and KrF lithography are compared and analyzed, which validates this resist processing technique.

2 Methodology of Modeling Line-End Shortening Effect in KrF Resists

2.1 Introduction

Extension of optical lithography into deep sub-micron regime exacerbates the finite spatial bandwidth effects of the various lithography subsystems. These effects are illustrated by so-called corner rounding and, if severe enough, by the line-end shortening phenomenon (LES). Several processes contribute to this phenomenon, mask fabrication, optical imagery, resist systems and wafer etch. Line-end shortening has been described and modeled, based on aerial image and Fickian acid-diffusion in post exposure bake (PEB). For chemically amplified resist (CAR) used in deep-UV lithography, however, acid diffusion is non-Fickian. Hence a more general model of LES based on PEB in CARs is desired.

Historically, many efforts have been made in modeling projection optics and deep-UV resists and simulating LES. T. Brunner found that the degree of LES was a strong function of linewidth [20]. C. Mack et al developed PROLITH, a widely accepted lithography simulator, and applied PROLITH in modeling line end shortening [21]. SOLID-C, a widely used lithography simulator developed by SIGMA-C Co, has proved very useful for 2D developed-resist image problems. J. Byers presented several

methodologies in calibrating chemically amplified resist models [22]. At University of California, Berkeley, M. Zuniga proposed a non-Fickian-diffusion resist model [23], based on which two post exposure bake (PEB) simulators, STORM was were developed by E. Croffie [24]. A physical model of LES using SPLAT and STORM was thereafter developed by the author [25].

2.2 Post Exposure Bake Model for Deep-UV Resist

Presently, resist models attempt to capture their behavior by converting an exposure dose to an initial acid concentration through Dill's ABC model[26][27][28]. During the post exposure bake, this initial acid catalyzes a deprotection/cross-linking reaction, which alters the solubility of the resist film. Meanwhile, the acid also diffuses throughout the resist, which accounts for the disappearance of standing wave effects existing in exposure. Dissolution models then predict development rates as a function of deprotection level, or activated site concentration. Traditionally, PEB model parameters have been obtained with FTIR traces of large, flood-exposed areas.

The simulation described in this paper adopts the reaction equations proposed by M. Zuniga [29][30] to describe deprotection kinetics in DUV resists.

$$\begin{aligned}
 \frac{\partial}{\partial t} C_{as} &= K_1(1 - C_{as})C_a^m \\
 \frac{\partial}{\partial t} C_a &= \frac{\partial}{\partial x} \left(D \frac{\partial}{\partial x} C_a \right) - K_2 C_a \\
 D &= D_0 e^{\omega C_{as}}
 \end{aligned}$$

Equation 2-1

Here K_1 is the reaction rate, K_2 is the acid loss rate, m is a fitting parameter, C_{as} and C_a are the activated (deprotected) site concentration and acid concentration, respectively. D is the acid diffusivity, which is an exponential function of C_{as} .

2.3 Extraction of PEB Parameters

Marco Zuniga et al presented a methodology for extracting PEB reaction and diffusivity parameters through broad area exposures without the need for FTIR measurement [29][30].

In the absence of diffusion, Equation 2-1 can be solved analytically to obtain the following expression of C_{as} , which describes the FTIR traces monitoring the disappearance of a carbonyl group to within a few percent in large flood exposed area:

$$\text{Equation 2-2} \quad C_{as}(t) = 1 - \exp\left\{-C_a^m \cdot \frac{K_1}{mK_2} (1 - e^{-mK_2})\right\}$$

Equation 2-2 states that the same level of activation in a broad area exposure can be reached by varying either exposure dose or PEB time as determined by the reaction parameters. Based on this fact, the following matrix of experiments was performed. PEB times were chosen in reference to the nominal PEB time by increasing the value by 50%. The exposure dose required to clear the resist under the given PEB time was determined by exposing a matrix of doses in steps of $1\text{mJ}/\text{cm}^2$. Then the PEB times and corresponding dose-to-clear were fitted with equation (4) to obtain K_1 , K_2 and m . The approximation methodology is illustrated in Figure 2-1.

The top-to-top contact experiment was used to determine acid diffusivity in an unexposed film, where the experiment set-up has been previously reported. It is illustrated in Figure 2-2. Resist was coated on a wafer, exposed, and then placed on the top of another wafer

which was coated with unexposed resist. With the two layers of resist in contact, the two wafers were baked. During the bake, acid diffused into the unexposed layer, hence in the develop process following PEB, part of the unexposed resist dissolved. By measuring the top loss of the unexposed resist, the diffusivity can be extracted.

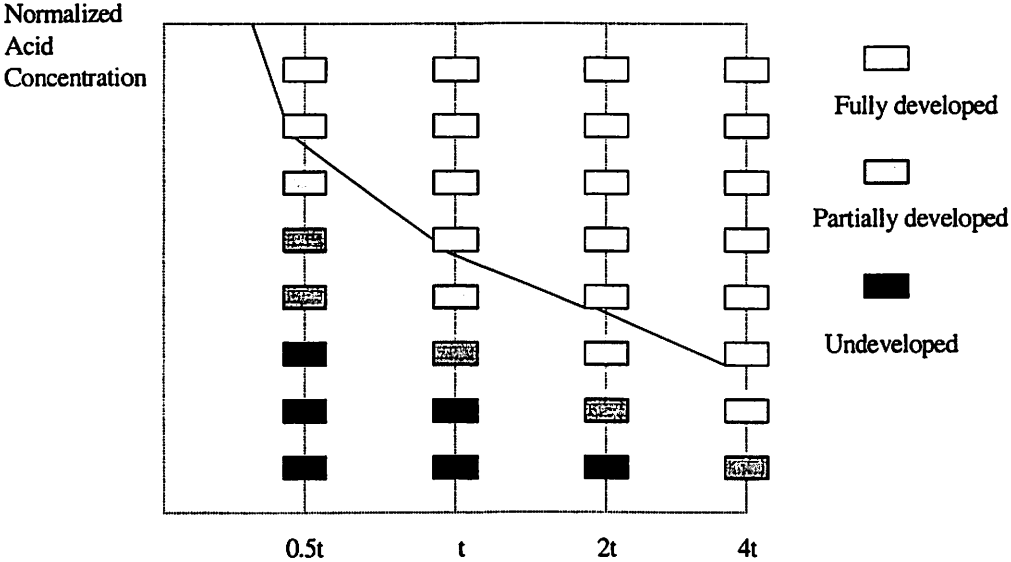


Figure 2-1 Schematic of experimental procedure for broad area exposure data collection

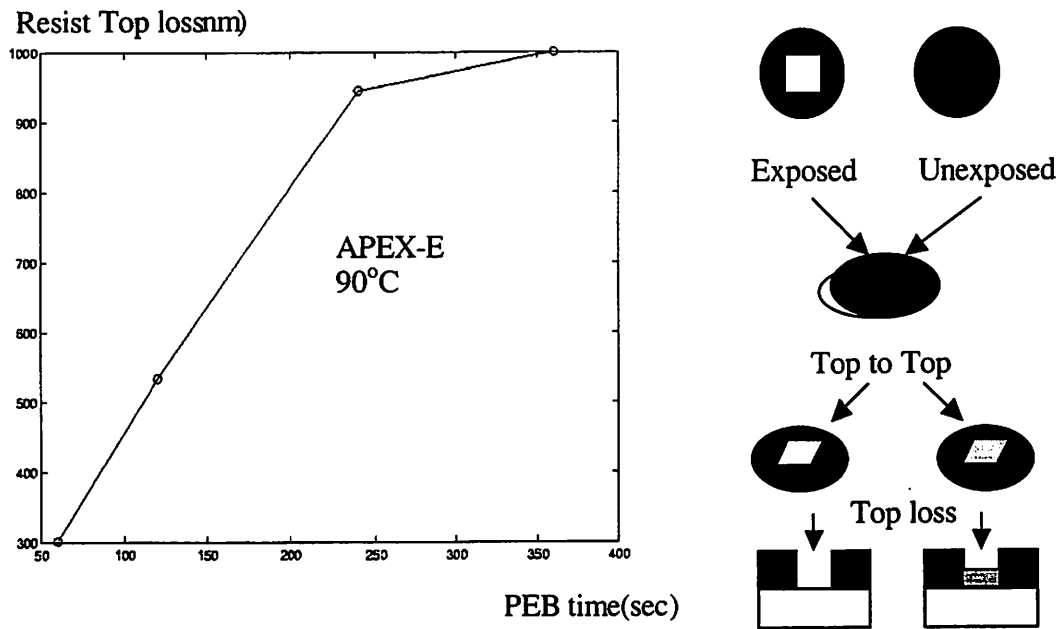


Figure 2-2 Schematic of top-to-top contact experiment

Both reaction and diffusion in DUV resist are activated-energy-driven processes, therefore the experiments described above were also conducted under different PEB temperatures in order to extract activation energy of reaction and diffusion parameters.

In our experiments, APEX-E and UVIIHS were coated at 3000 rpm for 30 sec and prebaked at 100°C and 140°C for 60 sec, respectively. The nominal PEB condition is 90°C for 60 sec for APEX-E, 140°C for 90 sec for UVIIHS. Standard development conditions were 0.25N tetramethylammoniumhydroxide (TMAH) for 50 sec, 0.263 N TMAH for 60sec, for APEX-E and UVIIHS, respectively. The methodology discussed previously was applied and Table 2-1 shows the extracted reaction and diffusion parameters for APEX-E and UVIIHS.

Table 2-1 Reaction/Diffusion parameters for APEX-E and UVIIHS

	$\ln K_1 (s^{-1})$	$E_{K1} (eV)$	$\ln K_2 (s^{-1})$	$E_{K2} (eV)$	m	$D_0 (nm^2/s)$	ω
APEX-E	55	1.7	5.56	0.34	1.7	11	5
UVIIHS	22	0.8	56	3.25	1.5	9	0

2.4 Simulation Process of Exposure and Post Exposure Bake

To simulate line-end shortening effects, a 2D simulator was developed and applied, which links SPLAT and STORM to simulate the exposure and PEB processes. Given the design pattern and optical parameters (NA, wavelength, coherence, dose, etc), SPLAT was used to obtain aerial image profiles on the top of the resist layer. Then the light intensity profile was converted into initial acid distribution through Dill's ABC model. Thereafter, STORM, a 2D reaction/diffusion simulator, was used to obtain the final activated site concentration profile, starting from the initial acid distribution which had been obtained previously. Finally, a threshold model was used to determine critical dimension. That means resist at which the activated site concentration is higher than a given threshold is considered to dissolve, otherwise the resist is considered to remain.

Figure 2-3 illustrates the whole simulation flow. Figure 2-4 shows an example of the simulation.

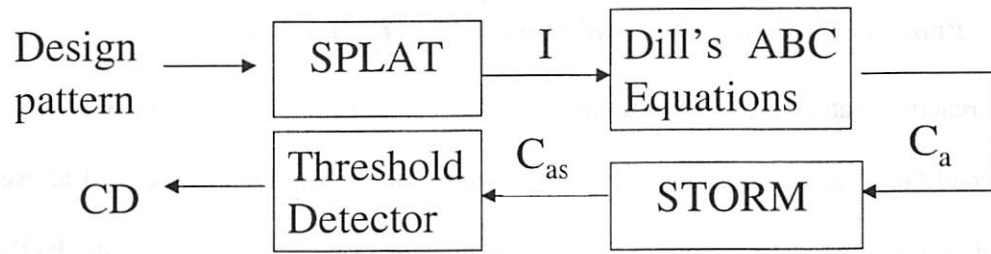


Figure 2-3 Schematic of exposure and PEB simulation.

In the diagram, I is the light intensity, C_a is the initial acid concentration, C_{as} is the final activated site concentration

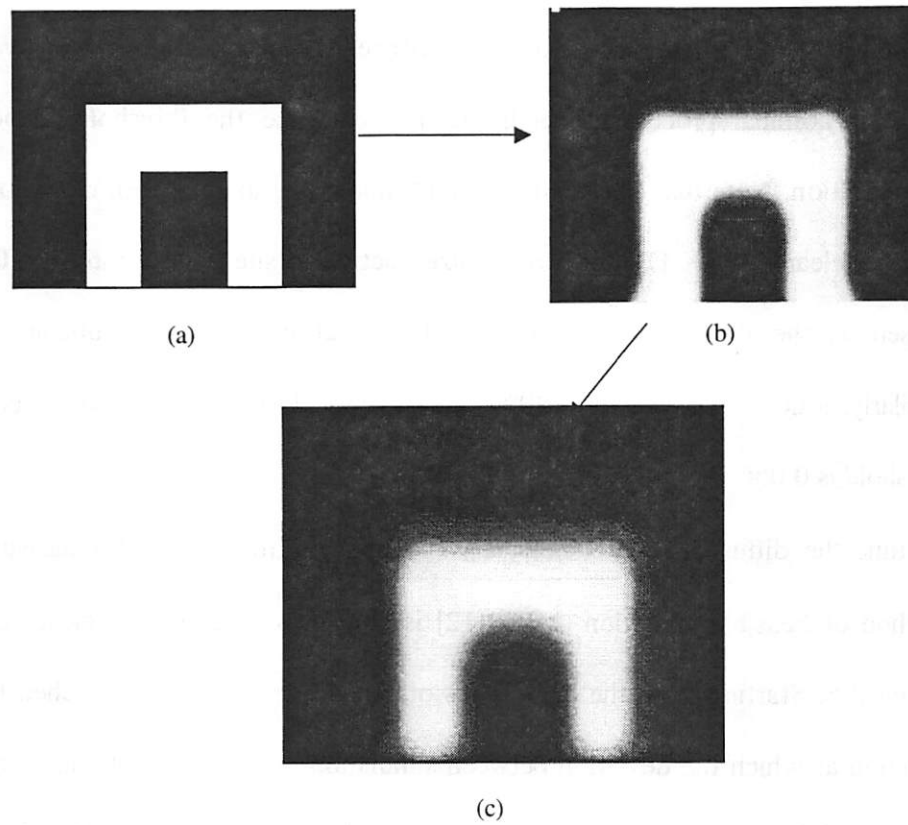


Figure 2-4 An example of LES simulation

Here (a) is the design pattern, (b) is the aerial image obtained by SPLAT, (c) is the activated site concentration obtained by STORM.

2.5 Process Optimization and Parameter Extraction

The reaction rate, acid loss rate and reaction power, namely K_1 , K_2 and m , can be obtained fairly accurately from the broad-area-exposure experiment described above. One proof is the coincidence between the experimental results and those from FTIR. The diffusivity, however, is not known with high confidence because of the large variance of the top-to-top experimental data, i.e., the high noise in the experiments. Hence a large-scale optimization technique was created to fit the diffusivity parameters with CD measurements.

To obtain the threshold of activated site concentration, the dose-to-clear values can be used for nominal processing conditions to determine the threshold of activated site concentration. Note that a dose of 8 mJ/cm^2 , under the nominal PEB conditions, 90°C , 60 sec, just clears APEX-E, thus a normalized activated site concentration of 0.046 can be chosen as the threshold, according to the reaction parameters obtained previously. Similarly, a dose of 8 mJ/cm^2 , 140°C , 90 sec, just clears UVIIHS, so the corresponding threshold is 0.056.

To tune the diffusivity parameters, D_0 and ω so as to fit the LES measurements, the Method of Feasible Direction (MFD)[12] is applied on a given design feature shown in Figure 2-5. Starting from the parameters obtained previously, we searched for a feasible direction at which the deviation between simulation and experiment can be reduced until a local minimum is reached. Many other randomly chosen starting points were also tested, then all the local optimums were compared so as to give a global optimum.

2.6 Compare Simulation with Experiment

Four types of features, named A to D, were tested. Figure 2-5 to 2-10 show the design patterns, LES from simulation and from SEM measurements. All wafers were exposed by Microstepper, wavelength 248 nm, NA 0.6, partial coherence 0.5, dose 10 mJ/cm². Top view SEMs and CD measurements using the top of the resist profile were then made.

Diffusivity parameters were then fine tuned by applying MFD to feature A. The linewidths for six different sizes, from 500 nm to 1000 nm, and two different PEB times, 30 sec and 60 sec, were simulated for a total of 12 measurements. The goal function is the root mean square error (RMSE) between the 12 CD measurements obtained from simulation and from SEM. It took 2 to 3 minutes to simulate one example which uses 10×75 grid. So it took more than 30 minutes to complete “one round”, i.e., simulation of the 12 examples. The optimization process took more than 150 rounds for APEX-E and about 20 rounds for UVIIHS. The RMSE for APEX-E and UVIIHS were reduced from 44 to 13, 27 to 24, respectively. Table 2-2 shows the optimized reaction/diffusion/threshold parameters for the two resists.

Table 2-2 Reaction/Diffusion/Threshold parameters for APEX-E and UVIIHS

	$\ln K_1(s^{-1})$	$E_{K1}(eV)$	$\ln K_2(s^{-1})$	$E_{K2}(eV)$	m	$D_0(nm^2/s)$	ω	Th
APEX-E	55	1.7	5.56	0.34	1.7	200	1	0.046
UVIIHS	22	0.8	56	3.25	1.5	0.6	0	0.056

From the figures, we found that the simulation for feature A and B matches very well with the SEM data while it is not so good for feature C and D. This can be explained by the fact that the CD of feature A is determined by a 1D process, in other words, it is only affected by the reaction and diffusion normal to the lines. Similarly, the CD of feature B is a 1.5D process-determined variable, the kinetics along the vertical direction plays a major role and the kinetics along the horizontal direction plays an additional minor role. While the CDs of feature C and D are actually 2D process-determined. The intrinsic complexity of C and B makes their simulation less accurate.

Table 2-3 shows the error analysis of APEX-E simulation. The second column shows the dimension index corresponding to the feature, which has been described above. The third column shows Δ LES values obtained from SEM data, and the fourth column shows Δ LES values from simulation. The Δ LES is defined in the next paragraph. RMS errors and relative errors are shown in column 5 and 6. The relative error is calculated by dividing RMSE with 400 nm, because we used 400 nm as a reference linewidth. Column 7 shows the R-square values of our simulation. The small RMSE and high R-square indicate that our simulation matched the experiment within an error of a few percent. Only for isolated dots, the error is higher than 20% when predicting features smaller than 400 nm.

An interesting index is the change in the dimension measured with bake time, which is defined as Δ LES:

Equation 2-3 Δ LES = Average of | CD of nominal PEB time - CD of half nominal PEB time | over all feature sizes

For APEX-E, the Δ LES is about 100 nm, and Δ LES of features A, B and C are close. They are all higher than the corresponding predictions but the differences between simulation and experiment results are small, which indicates that our simulation is reasonably close to the actual optical and chemical processes.

Table 2-4 shows the error analysis of UVIIHS simulation. For UVIIHS, our simulation still matched the SEM well. However, the DLES is not close to the experimental value. This, plus the fact that the diffusivity of UVIIHS listed in Table 2-2 is rather small, may be an indication that diffusion is not important for LES in UVIIHS, and that a prediction solely based on exposure could be sufficient.

Δ LES of feature D in both APEX-E and UVIIHS, however, is much higher than the corresponding prediction. This phenomenon can be explained by several factors. One is the “top tapering “ effect which is more severe in dots than in lines. Another factor is the more rapid degradation of dot image quality with feature size which is further exaggerated by the presence of lens aberration of our microstepper. Systematic errors also exist in the simulation process. First, the simulation is 2D while the actual exposure and PEB processes are 3D, thus the simulation tends to over-evaluate the diffusion length. Second, an ideal mask was presumed so the mask error is not taken into account.

An approach to overcome some of the errors discussed above will be presented in next Section. However, in order to comprehensively address all the main sources contributing to pattern distortion, a model including mask, lens and resist is absolutely necessary. The details of the comprehensive modeling framework will be discussed in Chapter 5.

Table 2-3 The error analysis of simulations versus experiments for APEX-E

Feature Type	Dimension	Δ LES of SEM (nm)	Δ LES of SIM (nm)	RMSE (nm)	Relative Error	R-Square
A, elbow	1D	112	93	26	0.06	0.90
B, line end	1.5D	147	134	18	0.04	0.85
C, post in square	2D	107	112	59	0.14	0.77
D, post	2D	221	125	101	0.25	0.66

Table 2-4 The error analysis of simulations vs. experiments for UVIHS

Feature Type	Dimension	Δ LES of SEM (nm)	Δ LES of SIM (nm)	RMSE (nm)	Relative Error	R-Square
A, elbow	1D	8	29	26	0.06	0.89
B, end at line	1.5D	49	17	71	0.18	0.68

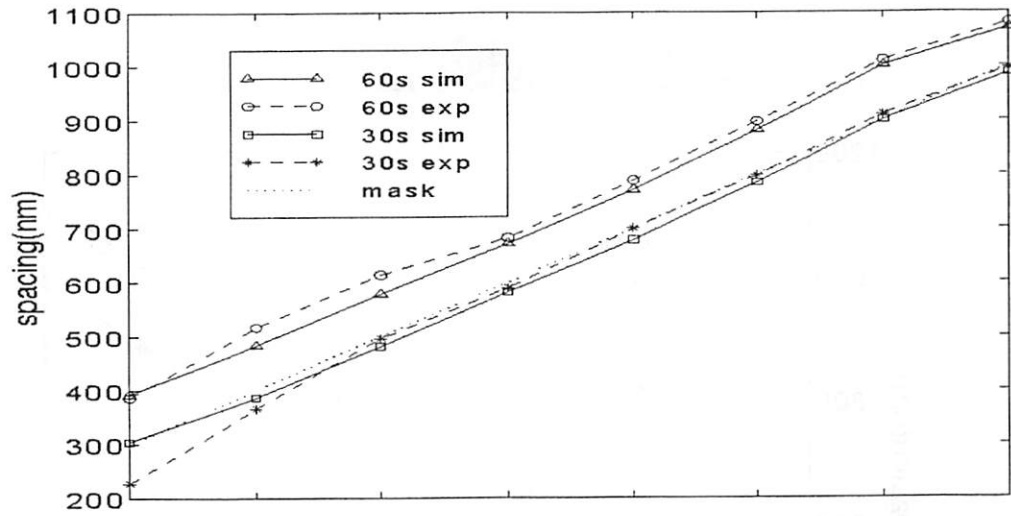
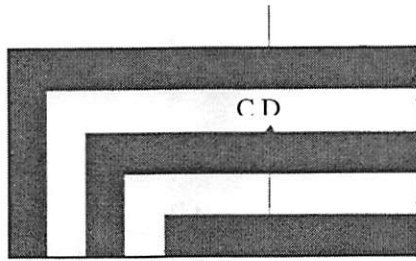


Figure 2-5 Simulation vs experiment for APEX-E, feature A, elbow

PEB temperature is 90°C. The upper graph is the mask pattern showing where the CD was measured. The lower graph shows the simulated CD vs. measured CD.

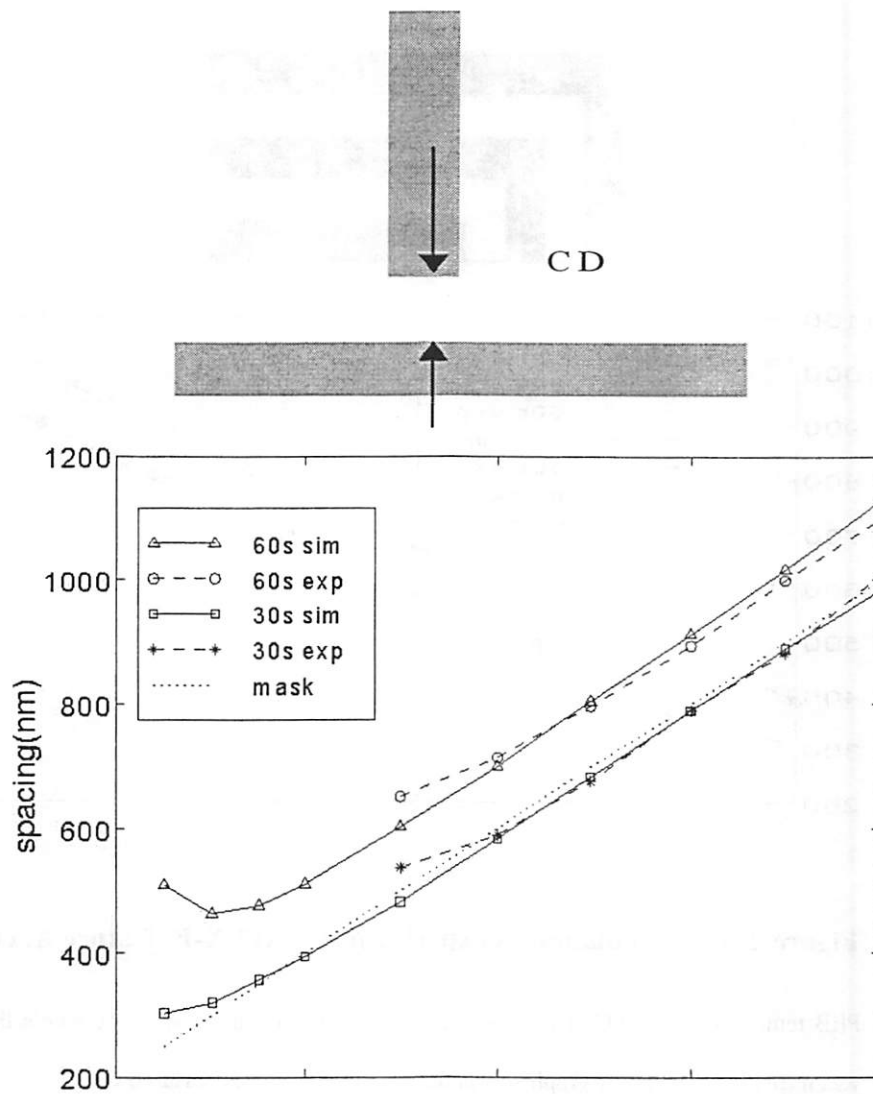


Figure 2-6 Simulation vs. experiment for APEX-E, feature B, end at line.

PEB temperature is 90°C. The upper graph is the mask pattern showing where the CD was measured. The lower graph shows the simulated CD vs. measured CD.

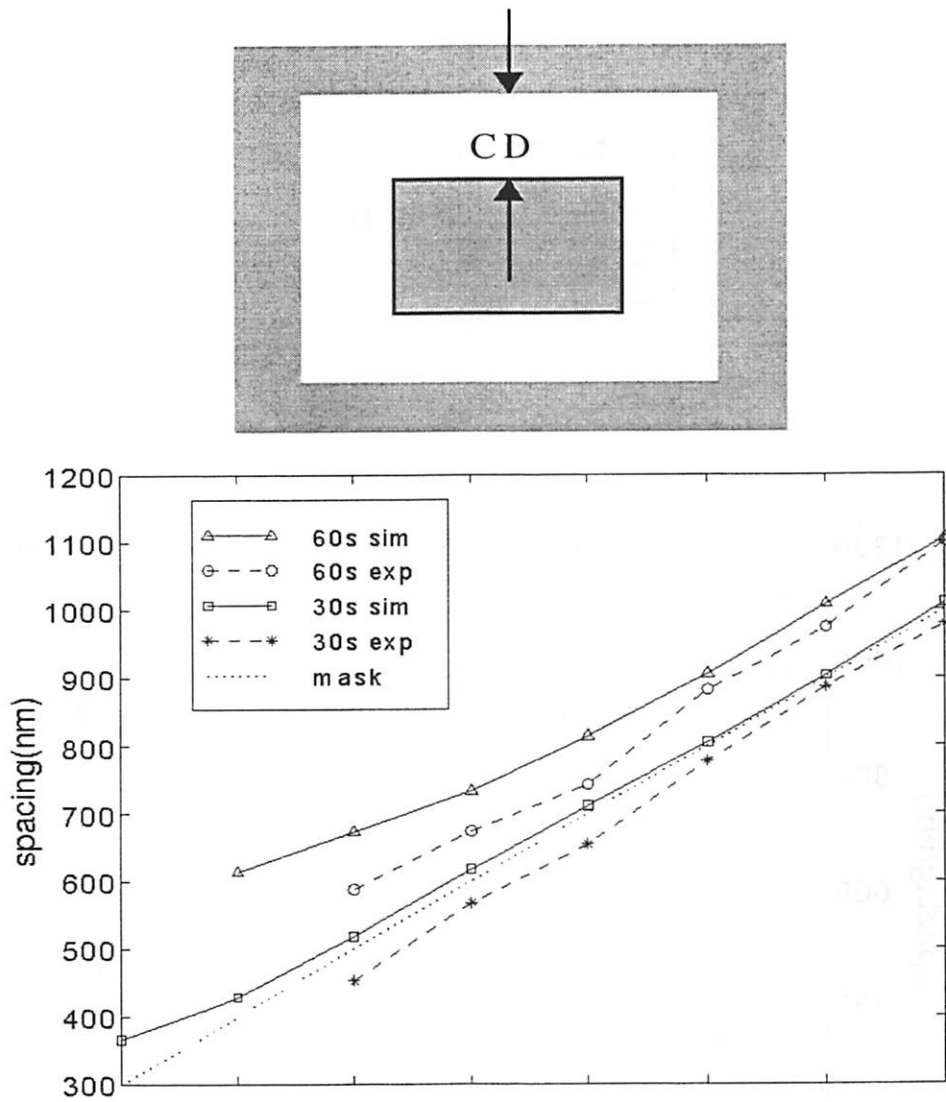


Figure 2-7 Simulation vs. experiment for APEX-E, feature C, post in square.

PEB temperature is 90°C. The upper graph is the mask pattern showing where the CD was measured. The lower graph shows the simulated CD vs. measured CD.

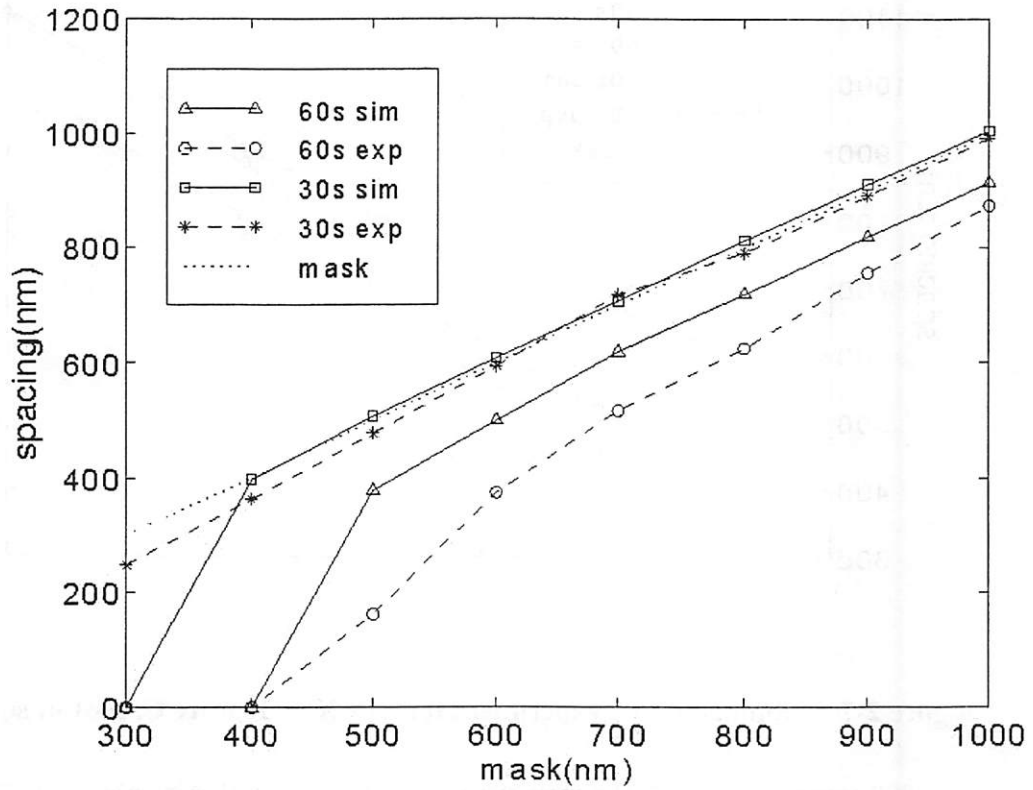
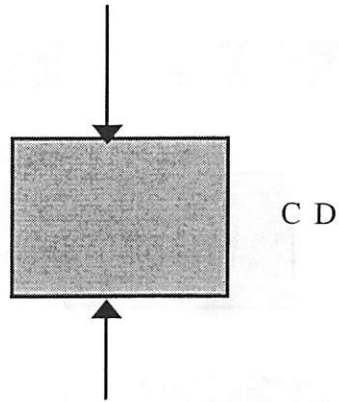


Figure 2-8 Simulation vs. experiment for APEX-E, feature D, post.

PEB temperature is 90°C. The upper graph is the mask pattern showing where the CD was measured. The lower graph shows the simulated CD vs. measured CD.

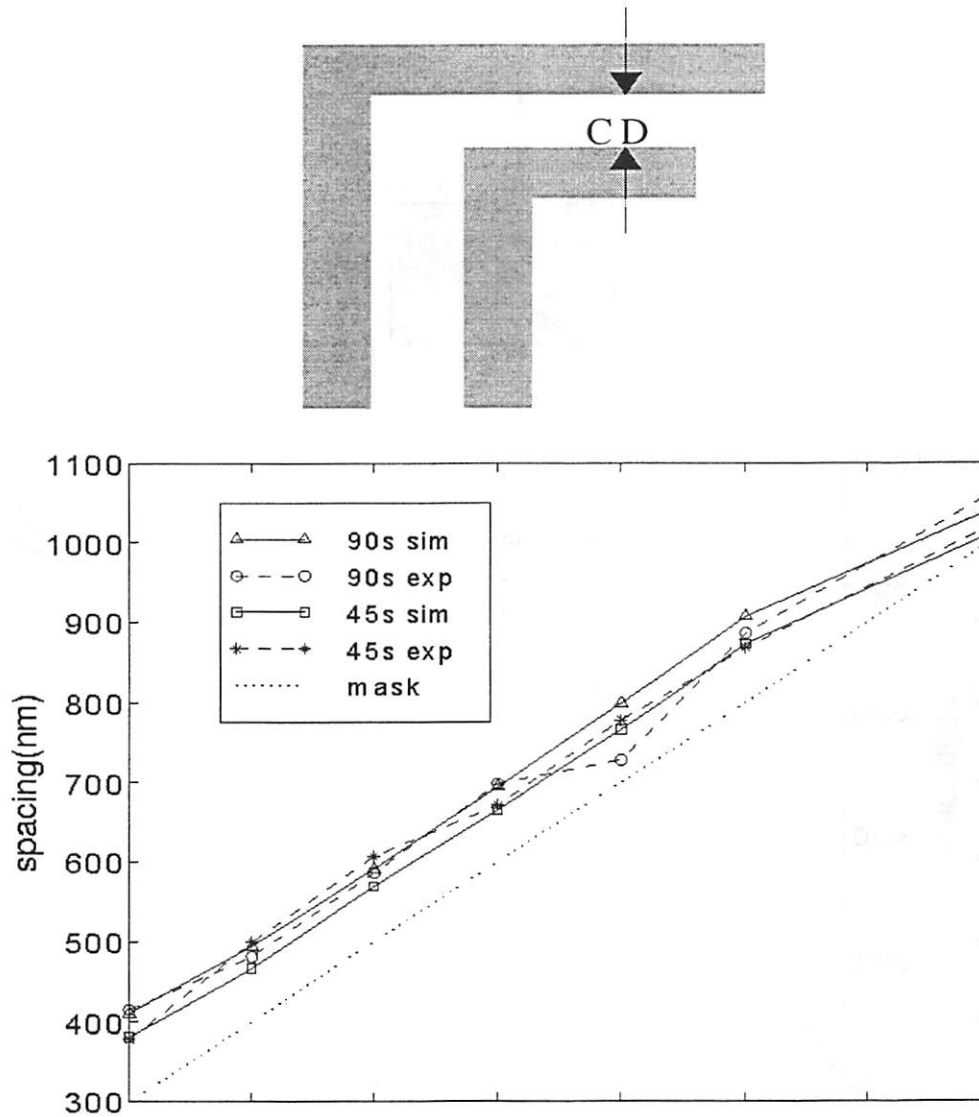


Figure 2-9 Simulation vs. experiment for UVIHS, feature A, elbow.

PEB temperature is 140°C. The upper graph is the mask pattern showing where the CD was measured. The lower graph shows the simulated CD vs. measured CD.

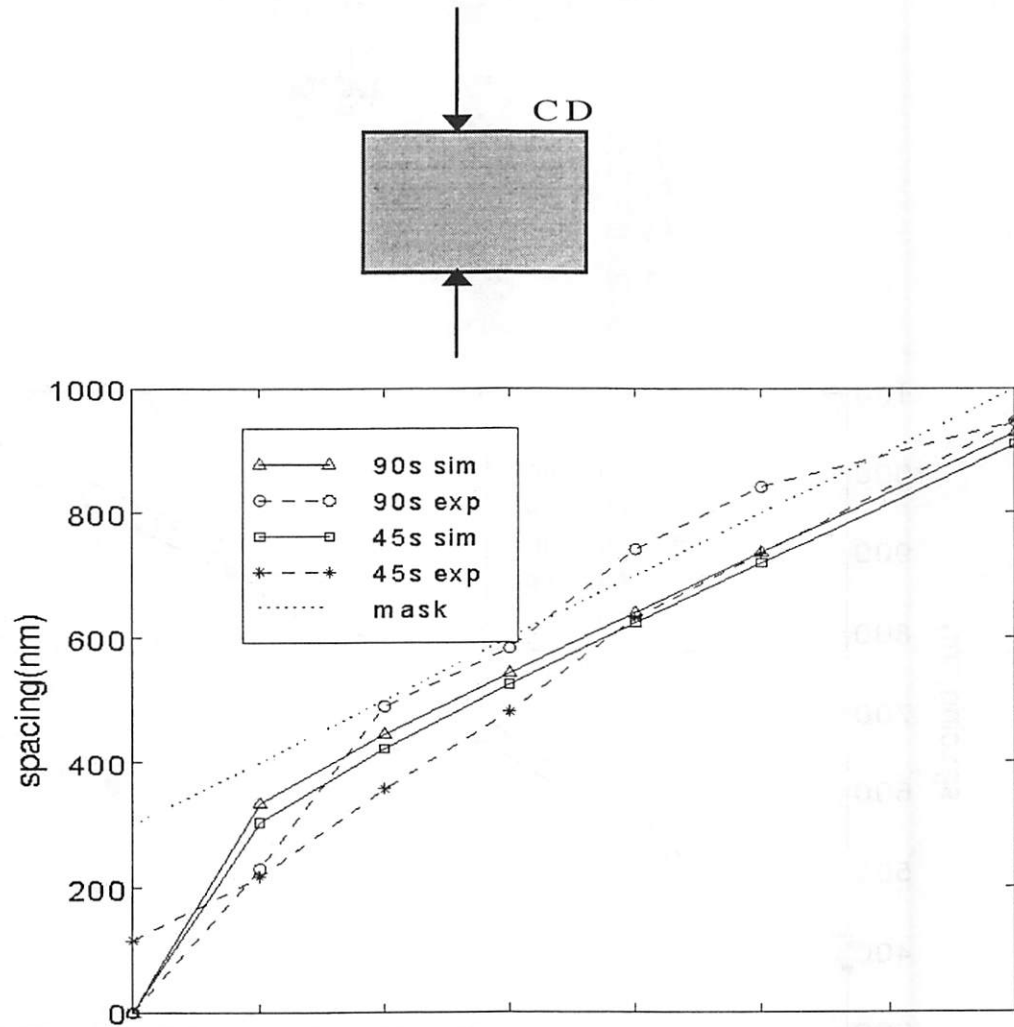


Figure 2-10 Simulation vs. experiment for UVIHS, feature D, post.

PEB temperature is 140°C. The upper graph is the mask pattern showing where the CD was measured. The lower graph shows the simulated CD vs. measured CD.

2.7 A Quick Approach to Predict Line-End Shortening in the Presence of Lens Imperfections

In the Section 2.2 to 2.6, a methodology of modeling LES in deep-UV resists is discussed, which uses simulation of optical exposure and PEB to predict LES. Due to the limit on computational complexity, the simulation is 2-dimensional, which means the aerial image simulation is employed. The aerial image simulation is frequently used in lithography to estimate the imaging results, process window, and so on. The use of aerial image is based on the assumption that the resist thickness is thin compared with exposure wavelength. The assumption is no more valid in 248 nm lithography, however, when the resist thickness is usually greater than $0.5\ \mu\text{m}$, or in other words, 2 wavelengths. Though 3D simulation of the electromagnetic field in resist is a promising solution [31], it is not practical for industrial applications. PROLITH, a lithography simulator developed by FINLE, overcome this difficulty by approximating latent image from aerial image [32]. In this section, a rapid approach is presented to calculate LES or line CDs based on 2D imaging simulation, which was verified by experimental data at Texas Instruments.

In general, the recording media in lithography is a stack composed of resist, anti-reflective coating (ARC) and wafer. Given the optical parameters and the thickness of these materials, including the complex refractive index and Dill's ABC parameters of resist, SPLAT can calculate the image intensities on any plane inside the resist and parallel to the wafer surface. Due to the optical absorption of resist, using the image intensity on the top surface plane of resist to predict CDs will underestimate line CDs while using image intensity on the bottom plane will overestimate line CDs, as is confirmed by SEM metrology. To correctly estimate the line CDs, a threshold

corresponding to a plane between top and bottom surfaces is setup in SEM metrology software at which the line CDs are measured. Thus using the image intensity on a plane located between the top and bottom surfaces will result in reasonable CD estimation. Intuitively, the plane should be chosen close to the middle of the resist. This is also confirmed by the litho engineers responsible for setting up recipes, who, for example, chose the plane 200 nm below the resist top surface as the “best focus” when the resist thickness was 350 nm.

Based on the above discussion, the approach for estimating CDs is presented as following:

Step 1: Choose an anchor line and its target CD, say, a 140nm wide isolated line which is needed to print as 140 nm wide on wafer. By adjusting dose/defocus, this anchoring process can be achieved with enough process latitude. The anchored recipe (dose/best focus) will be used in the later processes. In fact, this is a standard industrial process for setting up a litho recipe and is not part of our approach. It is listed here as a ground.

Step 2: With the optical parameters (refractive index, ABC parameters) and thickness of the recording materials (resist, ARC and wafer), use SPLAT to calculate the image intensities on the plane in the middle of the resist film. Here the mask pattern is chosen to be the anchor line (140nm isolated line). Since the anchor line is a 1D structure, we are only interested in the image intensity across the line. Denote the image intensity across the line to be $I(x)$, where x is the axis perpendicular to the line. Then the resist profile after develop can be calculated under the assumption of a threshold model:

Equation 2-4
$$J(x) = \begin{cases} 1 & I(x) \geq Th \\ 0 & I(x) < Th \end{cases}$$

Where Th is a predetermined threshold of image intensity, $J(x) = 1$ means to the resist is developed, whereas $J(x) = 0$ means the resist is not developed.

Then the line CD is given by

Equation 2-5
$$CD = \int_{-\infty}^{+\infty} [1 - J(x)] dx$$

Choose proper Th such that CD calculated in Equation 2-5 is the target CD obtained in Step 1.

Step 3: Given any mask pattern, use SPLAT to calculate the corresponding image intensity on the plane in the middle of the resist film. Denote the image intensity to be $A(x, y)$. Then the resist profile after develop is given by

Equation 2-6
$$B(x, y) = \begin{cases} 1 & A(x, y) \geq Th \\ 0 & A(x, y) < Th \end{cases}$$

Then any CD can be calculated correspondingly.

We will use the term ‘Image in Resist’ to refer to this rapid approach in this thesis.

2.8 Application of Image in Resist Approach to Different Scanners

The rapid Image in Resist approach presented in Section 2.7 gives reasonable estimation of CDs. However, to estimate CDs through the defocus range, the knowledge of lens aberrations is necessary, because lens aberrations degrade the image quality rapidly when the focal plane deviates from the best focus. Thus, we must include the lens aberrations to get correct image intensities when using SPLAT to calculate the image intensity on a

plane in resist. In this chapter, the simulations using Image in Resist approach are all including lens aberrations unless otherwise noted.

To validate the effectiveness of the Image in Resist Approach, a set of experiments were done at Texas Instruments. Three 248nm scanners named LS31D, LS32D and LS33D were used, NA 0.68, σ 0.75. The resist UV-5 was used, refractive index $n=1.71$, $k=0.0476$, Dill's parameters are $A=0.5389$, $B=0.00968$, thickness 750 nm. In between UV-5 resist and Si wafer is bottom anti-reflective coating (BARC) DUV30L, refractive index $n=1.55$, $k=0$, thickness 160 nm. The lens aberration data of the three scanners were measured via Litel technology[33].

A 150nm wide isolated line was used as the anchor line. The target CD was 180 nm to compensate the litho-etch bias. The actual wafer CDs may not be exactly 180 nm. Then the actual CD, for example, 179.1 nm, was used to calibrate the threshold model.

After obtaining the threshold, the Image in Resist Approach was used to predict the LES through the defocus range. The pattern showing LES is depicted in Figure 2-11.

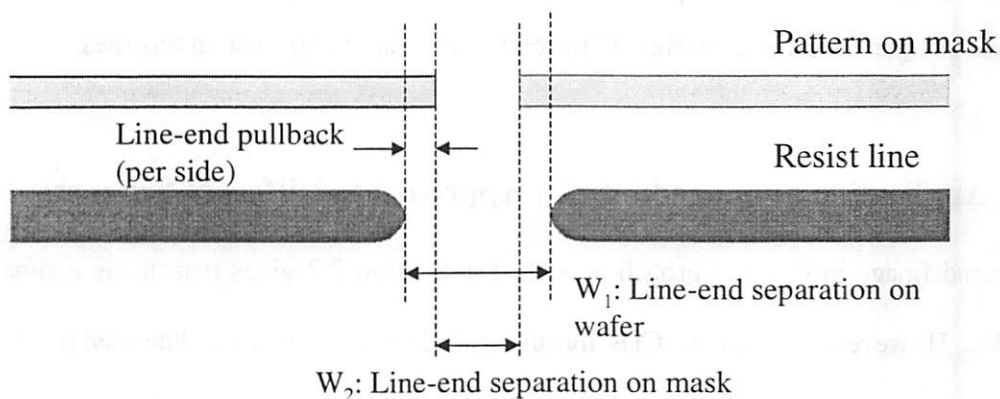
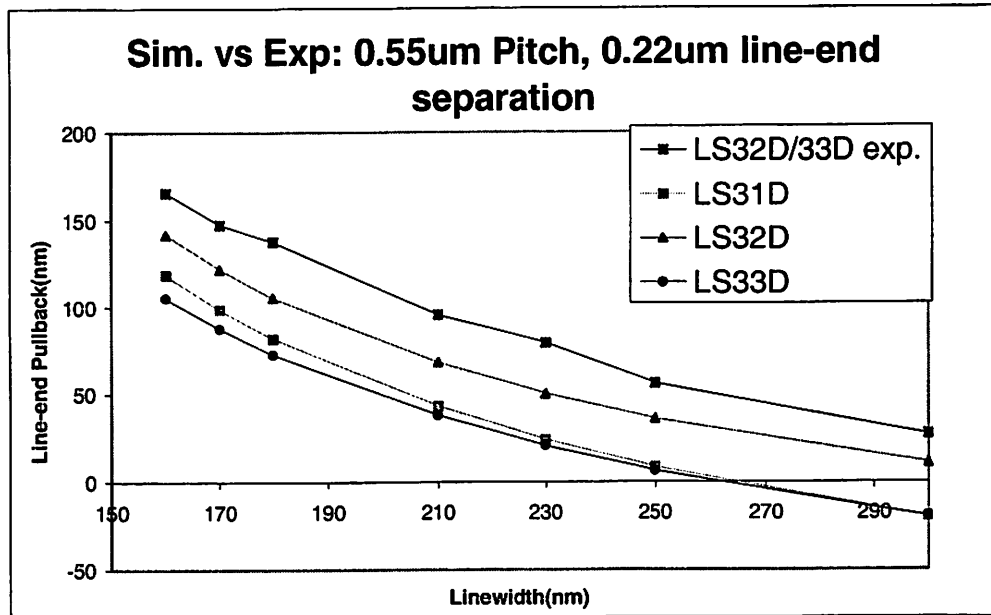


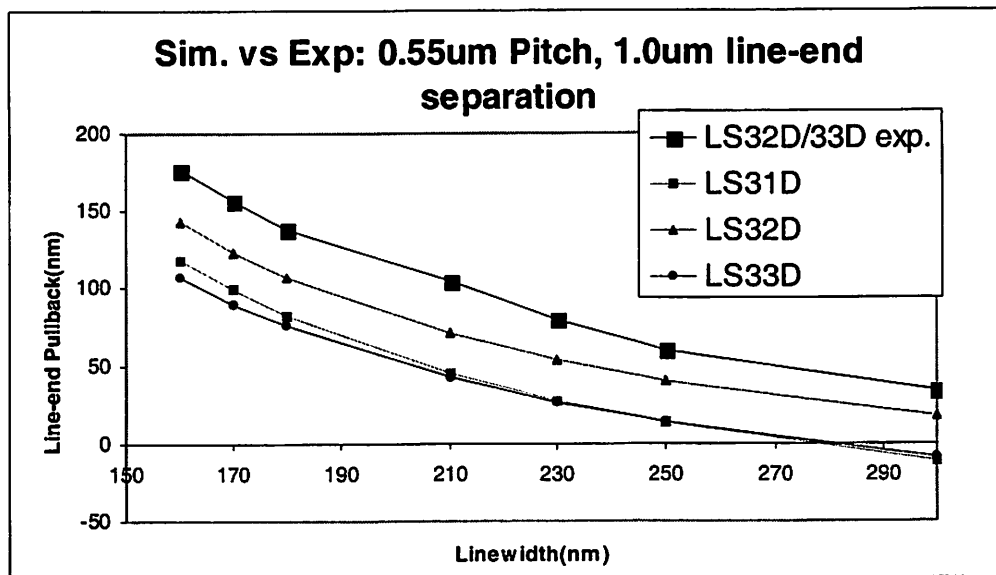
Figure 2-11 The calculation of line-end shortening

LES is defined as the pullback of the resist line ends compared with the line ends on mask. In this pattern, total LES = $W_1 - W_2 = 2 * (\text{LES per side})$

Figure 2-12 and 2-13 compare the simulated LES with experimental data.



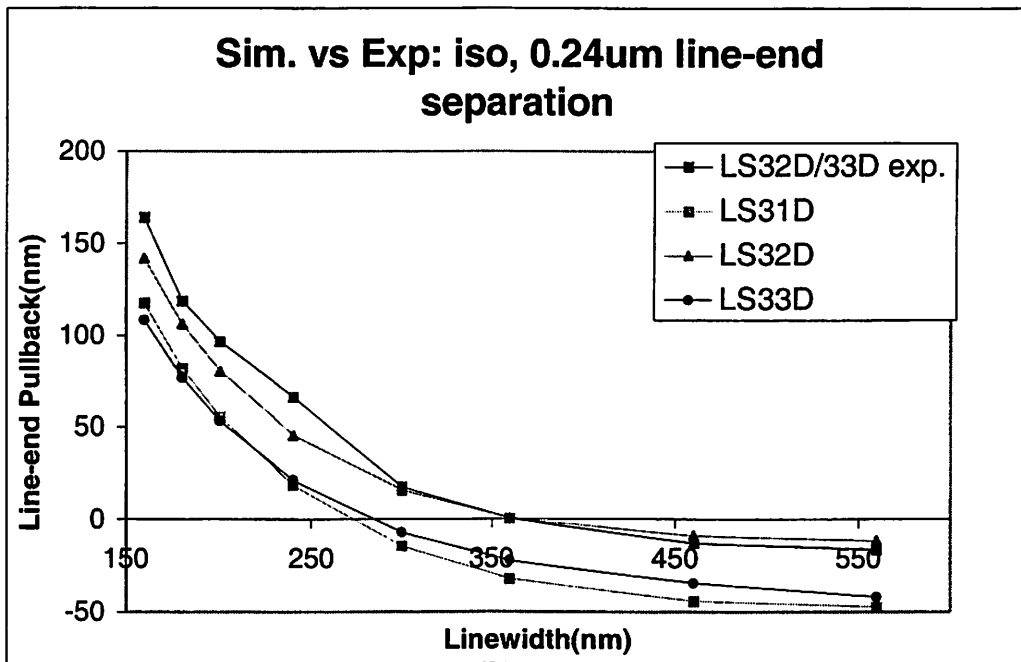
(a)



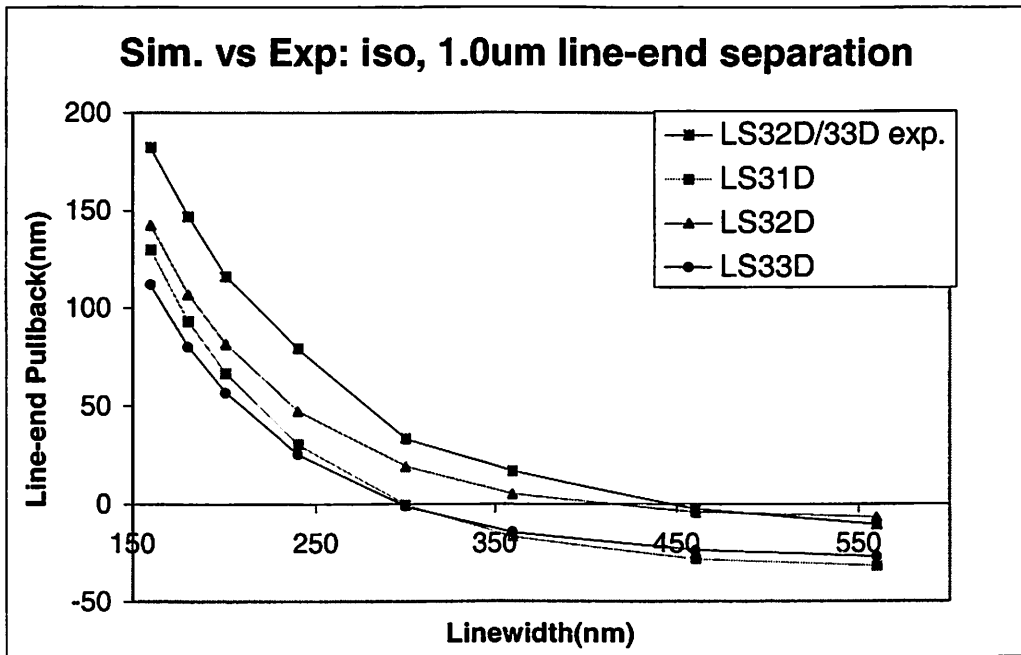
(b)

Figure 2-12 Line-end shortening simulations vs. experiments of dense lines.

The pitch of the dense lines is $0.55\mu\text{m}$. In (a), the spacing between line ends is $0.22\mu\text{m}$, and in (b), the spacing is $1\mu\text{m}$.



(a)



(b)

Figure 2-13 Line-end shortening simulations vs. experiments of isolated lines.

In (a), the spacing between line ends is 0.24 μ m, and in (b), the spacing is 1 μ m.

It can be seen that the simulated LES is consistently smaller than that of experiment, which indicates that the optical model is not very effective in the area of line-ends, although it is quite effective in predicting the linewidth. This is not surprising because the line-end is basically a 2D structure whereas the line-width is a 1D structure. The simple single threshold model is no more valid due to the more complex resist/developer chemistry in 2D structures. Multi-threshold models were proposed in [34][35] to fix the discrepancy between optical simulation and experiment. In this thesis, this discrepancy will be addressed through combination of optics and resist modeling in Chapter 5.

Nevertheless, the simulation captures the trends of LES with linewidth and line-end spacing varying. LES is particularly severe in the region where linewidth is less than 250nm. LS33D has much smaller lens aberrations or larger Strehl ratio than LS32D, which results in a smaller LES shown by simulation. Experimentally, however, the LES of LS33D and LS32D are almost identical, which indicates that the resist chemistry could play a more important role in LES than lens aberrations do. The focal plane in these simulations and experiments was chosen to be the best focus. In the case of defocused exposure, the lens aberrations are expected to make significant impact on LES and other pattern distortions.

2.9 Conclusion

In this chapter a methodology for extracting PEB parameters and simulating line-end shortening effects is described. PEB parameters for APEX-E and UVIIHS were extracted and then tuned to fit LES measurement. Simulation and SEM measurement of LES in

APEX-E and UVIIHS are compared. The simulation results considerably matched the SEM data to better than 10% of linewidth.

The verification experiment was not sufficiently completed in the small K_1 region, and for this reason we are conducting new verification experiments on commercial scanners. A rapid Image in Resist Approach is presented which use the image intensity in resist to predict LES in the presence of lens imperfection. The simulation results of Image in Resist Approach is compared with experimental data at Texas Instruments. The simulation captures the trends of LES vs. CD, and is consistent with the experiments. The lack of fitness is expected to be fixed by incorporation of resist PEB models.

A 3D simulator is needed to simulate the actual exposure and PEB processes, which is not feasible without a algorithm at least 10 times faster than conventional methods. Furthermore, the above two methodologies are both calibrated with 1-dimensionanl CD data, which leads to discrepancy between experiments when the calibrated model is extrapolated to 2-dimensionanl structures. If the models are calibrated with 2D SEM pictures, the simulation of 2D structures will be an interpolation problem in which users have much more confidence.

After all, the two key enabling components for comprehensive model of projection lithography are fast algorithm and 2D calibration method, which will be discussed in Chapter 3 and 4, respectively. The methodology of comprehensive modeling and the implications the model delivers will be discussed in Chapter 5.

3 Fast Algorithm for Simulating Post Exposure Baking Process

3.1 Introduction

This chapter presents a novel and fast algorithm for numerically solving partial differential equations and applies this algorithm to simulation of post exposure baking. Post exposure bake involves many physical and chemical processes, such as acid-catalyzed deblocking reaction, acid diffusion, free volume generation, acid trapping and neutralization, and so on[36]. Most of the processes have to be described by nonlinear partial differential equations (PDE). The coupled PDE system presents a formidable challenge to PEB modeling in that a complete physical-chemical simulation by solving the PDE system is computationally intensive. This computational time-complexity has restricted PEB simulation as well as its applications in OPC. In 1996, Marco Zuniga used this exponential-diffusion model to simulate PEB process[30]. Then in 1998, Ebo. Croffie released STORM 2.0, which solves the same equations with much higher speed [11]. However, it still takes STORM several minutes to complete a small-scale simulation. Though it is numerically accurate, STORM is not satisfying in industrial applications considering that an OPC validation of a single structure requires a lot of small-scale simulations. In this chapter, an imaging algorithm for 2D PEB simulation is presented that achieves high speed and also maintains physical accuracy.

3.2 Post Exposure Bake Model

During the post exposure bake (PEB) step, several chemical and physical processes take place. Photoacid catalyzes the deblocking process[37], in which the blocked insoluble polymer is converted to a soluble polymer with hydroxyl group and a volatile component. The volatile group then generates free volume that enhances the photoacid diffusivity. Meanwhile, the photoacid can be deactivated by neutralization and evaporation, or be trapped due to lack of free volume. Some resist systems also suffer from substrate or air contamination[38].

In spite of the complexity of PEB process, essentially it can be modeled as two simultaneous processes. One process is the diffusion and/or loss of photoacid, and the other is the deprotection of the blocking groups catalyzed by photoacid. In this thesis, the exponential-diffusion model is adopted, which was first proposed by R. Ferguson and then thoroughly studied by M. Zuniga[23].

$$\text{Equation 3-1} \quad \frac{\partial C_{as}}{\partial t} = K_1 (1 - C_{as}) C_a^m$$

$$\text{Equation 3-2} \quad \frac{\partial C_a}{\partial t} = \nabla \cdot (D \nabla C_a) - K_2 C_a$$

$$\text{Equation 3-3} \quad D = D_0 \exp(\omega C_{as})$$

Equation 3-1 describes the acid catalyzed deblocking reaction. C_{as} is the normalized activated site concentration, defined as the percent of blocking groups that have been deblocked. C_a is the normalized photoacid concentration, K_1 is the reaction rate constant, and m is the order of the reaction.

Equation 3-2 describes the acid diffusion and loss process. K_2 is the acid loss rate constant, which is determined by acid loss mechanisms such as neutralization,

evaporation and trapping inside resist. D is the acid diffusivity, which is given in Equation 3-3.

In general, the acid diffusivity is determined by the amount of diffusion paths in resist [7]. In PEB, the amount of diffusion paths increases as free volume is generated in deprotection process. The more extent to which resist is deprotected, the more free volume is generated. Thus the activated site concentration, C_{as} , is a measure of the amount of free volume. According to the above arguments, Equation 3-3 links the acid diffusivity D to the activated site concentration C_{as} .

A more general model is discussed in [39]. As will be shown in later chapters, this simplified exponential-diffusion model is sufficient for predicting the pattern fidelity in optical lithography. The general models can be easily integrated into the modeling framework with the same methodologies presented in this thesis. So I will focus on this simplified PEB model.

3.3 Fast Algorithm to Solve Partial Differential Equations

Modeling PEB process is to solve the PDE system described by Equation 3-1, 3-2 and 3-3. STORM, written by E. Croffie using Finite Element Method (FEM), is a solver of this PDE system[40]. To achieve higher speed, however, it is helpful to take advantage of the characteristic of PEB. In PEB, C_{as} and C_a evolve smoothly. The curves of C_{as} and C_a vs. time can be approximated by polynomials. Thus an algorithm is presented in this thesis for solving any PDE systems whose solution can be approximated by polynomials. In fact, any PDE systems that can be solved by finite difference method satisfy this condition.

Consider the following PDE system:

$$\frac{\partial \psi_1}{\partial t} = f_1(\bar{\psi}, \bar{\psi}_x, \bar{\psi}_{xx})$$

Equation 3-4

...

$$\frac{\partial \psi_n}{\partial t} = f_n(\bar{\psi}, \bar{\psi}_x, \bar{\psi}_{xx})$$

Given the boundary conditions:

Equation 3-5 $\Psi_1(\mathbf{x}, 0), \dots, \Psi_n(\mathbf{x}, 0)$

Equation 3-6 $\mathbf{G}(\Psi, \Psi_x)|_S = 0$, where S is the boundary.

Here $\mathbf{x} = (x_1, \dots, x_m)$ is an m -variable vector. $\Psi_1 = \Psi_1(\mathbf{x}, t)$, ..., $\Psi_n = \Psi_n(\mathbf{x}, t)$ are the functions to be solved.

For simplicity, denote $\Psi = (\Psi_1, \dots, \Psi_n)$. Also, denote $\Psi_x = (\frac{\partial \Psi_1}{\partial x}, \dots, \frac{\partial \Psi_n}{\partial x})$ is the

Jacobian of Ψ with respect to \mathbf{x} . Let $\Psi_{xx} = (\frac{\partial^2 \Psi_1}{\partial x^2}, \dots, \frac{\partial^2 \Psi_n}{\partial x^2})$ be the second partial differential of Ψ with respect to \mathbf{x} .

To numerically solve the PDE system, the simulation domain is discretized into a uniform grid. Without loss of generality, x_1 is discretized at $x_{11}, x_{12}, \dots, x_{1,N_1}$, x_2 is discretized at $x_{21}, x_{22}, \dots, x_{2,N_2}, \dots$. x_m is discretized at $x_{m1}, x_{m2}, \dots, x_{m,N_m}$. Thus the functions $\Psi_1, \Psi_2, \dots, \Psi_n$ are represented by their values sampled at the grid $\Psi(x_{1,i_1}, x_{2,i_2}, \dots, x_{m,i_m})$, $1 \leq i_1 \leq N_1, \dots, 1 \leq i_m \leq N_m$.

Given the initial functions sampled at the grid, $\Psi(x_{1i_1}, x_{2i_2}, \dots, x_{mi_m}, 0)$, $1 \leq i_1 \leq N_1, \dots, 1 \leq i_m \leq N_m$, $\Psi(\mathbf{x}, 0)$ can be approximated by cubic splines:

Equation 3-7
$$\Psi(x_1, \dots, x_n, 0) = \sum_{j_1=0}^3 \sum_{j_2=0}^3 \dots \sum_{j_m=0}^3 C_{i_1 i_2 \dots i_m}^{j_1 j_2 \dots j_m} x_1^{j_1} x_2^{j_2} \dots x_m^{j_m}$$

When $x_{1,i_1} \leq x_1 \leq x_{1,i_1+1}, \dots, x_{m,i_m} \leq x_m \leq x_{m,i_m+1}$

In Equation 3-7, $C_{i_1 i_2 \dots i_m}^{j_1 j_2 \dots j_m}$ is a constant n-vector, each element of which corresponds to the coefficient of $x_1^{j_1} x_2^{j_2} \dots x_m^{j_m}$ in Ψ_1, \dots, Ψ_n , respectively. Note that the whole simulation domain is divided into $(N_1 - 1) \times (N_2 - 1) \dots \times (N_m - 1)$ regions. In each region $\Psi(x, 0)$ is written as an m-variable, 3rd order polynomial. Meanwhile, $\Psi(x, 0)$ is C^2 all over the simulation domain.

The characteristics and calculation of splines can be found in [41]. Now that $\Psi(x, 0)$ has been represented by cubic splines, the first and second partial differential can be calculated by

Equation 3-8
$$\Psi_x(x_1, \dots, x_m, 0) = \begin{pmatrix} \frac{\partial \Psi}{\partial x_1} \Big|_{x_1, \dots, x_m, t=0} \\ \dots \\ \frac{\partial \Psi}{\partial x_m} \Big|_{x_1, \dots, x_m, t=0} \end{pmatrix}$$

$$\frac{\partial \Psi}{\partial x_1} \Big|_{x_1, \dots, x_m, t=0} = \sum_{j_1=0}^3 \sum_{j_2=0}^3 \dots \sum_{j_m=0}^3 C_{i_1 i_2 \dots i_m}^{j_1 j_2 \dots j_m} (j_1 x_1^{j_1-1}) x_2^{j_2} \dots x_m^{j_m}$$

$$\frac{\partial \Psi}{\partial x_2} \Big|_{x_1, \dots, x_m, t=0} = \sum_{j_1=0}^3 \sum_{j_2=0}^3 \dots \sum_{j_m=0}^3 C_{i_1 i_2 \dots i_m}^{j_1 j_2 \dots j_m} x_1^{j_1} (j_2 x_2^{j_2-1}) \dots x_m^{j_m}$$

...

$$\frac{\partial \Psi}{\partial x_m} \Big|_{x_1, \dots, x_m, t=0} = \sum_{j_1=0}^3 \sum_{j_2=0}^3 \dots \sum_{j_m=0}^3 C_{i_1 i_2 \dots i_m}^{j_1 j_2 \dots j_m} x_1^{j_1} x_2^{j_2} \dots (j_m x_m^{j_m-1})$$

When $x_{1,i_1} \leq x_1 \leq x_{1,i_1+1}, \dots, x_{m,i_m} \leq x_m \leq x_{m,i_m+1}$

Equation 3-9

$$\Psi_{xx}(x_1, \dots, x_m, 0) = \begin{pmatrix} \frac{\partial^2 \Psi}{\partial x_1^2} & \frac{\partial^2 \Psi}{\partial x_1 \partial x_2} & \dots & \frac{\partial^2 \Psi}{\partial x_1 \partial x_m} \\ \frac{\partial^2 \Psi}{\partial x_2 \partial x_1} & \frac{\partial^2 \Psi}{\partial x_2^2} & \dots & \frac{\partial^2 \Psi}{\partial x_2 \partial x_m} \\ \dots & \dots & \dots & \dots \\ \frac{\partial^2 \Psi}{\partial x_m \partial x_1} & \frac{\partial^2 \Psi}{\partial x_m \partial x_2} & \dots & \frac{\partial^2 \Psi}{\partial x_m^2} \end{pmatrix}$$

$$\frac{\partial^2 \Psi}{\partial x_k^2} \Big|_{x_1, \dots, x_m, t=0} = \sum_{j_1=0}^3 \sum_{j_2=0}^3 \dots \sum_{j_m=0}^3 C_{i_1 i_2 \dots i_m}^{j_1 j_2 \dots j_m} x_1^{j_1} \dots [j_k (j_k - 1) x_k^{j_k - 2}] \dots x_m^{j_m}$$

$$1 \leq k \leq m$$

$$\frac{\partial^2 \Psi}{\partial x_k \partial x_l} \Big|_{x_1, \dots, x_m, t=0} = \sum_{j_1=0}^3 \sum_{j_2=0}^3 \dots \sum_{j_m=0}^3 C_{i_1 i_2 \dots i_m}^{j_1 j_2 \dots j_m} x_1^{j_1} \dots (j_k x_k^{j_k - 1}) \dots (j_l x_l^{j_l - 1}) \dots x_m^{j_m}$$

$$1 \leq k, l \leq m, k \neq l$$

When $x_{1,i_1} \leq x_1 \leq x_{1,i_1+1}, \dots, x_{m,i_m} \leq x_m \leq x_{m,i_m+1}$

After obtaining $\Psi_x = \left(\frac{\partial \Psi_1}{\partial x}, \dots, \frac{\partial \Psi_n}{\partial x} \right)$ and $\Psi_{xx} = \left(\frac{\partial^2 \Psi_1}{\partial x^2}, \dots, \frac{\partial^2 \Psi_n}{\partial x^2} \right)$ from Equation 3-8 and

3-9, the partial differential of Ψ with respect to t is given by Equation 3-4.

$$\frac{\partial \psi_1}{\partial t} = f_1(\Psi, \Psi_x, \Psi_{xx})$$

...

$$\frac{\partial \psi_n}{\partial t} = f_n(\Psi, \Psi_x, \Psi_{xx})$$

With $\frac{\partial \psi}{\partial t}$, $\Psi(x, t = \tau)$ can be obtained by Taylor expansion cut off at the second order:

Equation 3-10 $\Psi(x, \tau) = \Psi(x, 0) + \tau \cdot \frac{\partial \psi}{\partial t} \Big|_{x,0} + \frac{1}{2} \tau^2 \frac{\partial^2 \psi}{\partial t^2} \Big|_{x,0}$

In Equation 3-10, only $\frac{\partial^2 \psi}{\partial t^2} \Big|_{x,0}$ is unknown. $\frac{\partial^2 \psi}{\partial t^2}$ must satisfy the following equations.

Equation 3-11
$$\frac{\partial \psi}{\partial t} \Big|_{x,t} = \frac{\partial \psi}{\partial t} \Big|_{x,0} + \tau \cdot \frac{\partial^2 \psi}{\partial t^2} \Big|_{x,0}$$

$$\frac{\partial \psi_1}{\partial t} \Big|_{x,\tau} = f_1(\Psi(x,\tau), \Psi_x(x,\tau), \Psi_{xx}(x,\tau))$$

Equation 3-12 ...

$$\frac{\partial \psi_n}{\partial t} \Big|_{x,\tau} = f_n(\Psi(x,\tau), \Psi_x(x,\tau), \Psi_{xx}(x,\tau))$$

Thus $\frac{\partial^2 \psi}{\partial t^2} \Big|_{x,0}$ can be obtained by simultaneously solving Equation 3-11 and 3-12. An

iterative method is presented to solve Equation 3-11 and 3-12:

Step 1: Let $\frac{\partial^2 \psi}{\partial t^2} \Big|_{x,0} = 0$.

Step 2: Calculate $\Psi(x,\tau)$ at the grid. That is, calculate $\Psi(x_{1i_1}, x_{2i_2}, \dots, x_{mi_m}, \tau)$, $1 \leq i_1 \leq N_1, \dots, 1 \leq i_m \leq N_m$, using Equation 3-10.

Step 3: Express $\Psi(x,\tau)$ in the form of cubic splines, i.e., write $\Psi(x,\tau)$ in the form below:

Equation 3-13
$$\Psi(x_1, \dots, x_n, \tau) = \sum_{j_1=0}^3 \sum_{j_2=0}^3 \dots \sum_{j_m=0}^3 C_{i_1 i_2 \dots i_m}^{j_1 j_2 \dots j_m} x_1^{j_1} x_2^{j_2} \dots x_m^{j_m}$$

$$\text{When } x_{1,i_1} \leq x_1 \leq x_{1,i_1+1}, \dots, x_{m,i_m} \leq x_m \leq x_{m,i_m+1}$$

Then calculate the first and second partial differentials of $\Psi(x,\tau)$ with respect to t using Equation 3-14 and 3-15:

$$\begin{aligned}
\Psi_{\mathbf{x}}(x_1, \dots, x_m, \tau) &= \begin{pmatrix} \frac{\partial \Psi}{\partial x_1} \Big|_{x_1, \dots, x_m, t=\tau} \\ \dots \\ \frac{\partial \Psi}{\partial x_m} \Big|_{x_1, \dots, x_m, t=\tau} \end{pmatrix} \\
\frac{\partial \Psi}{\partial x_1} \Big|_{x_1, \dots, x_m, t=\tau} &= \sum_{j_1=0}^3 \sum_{j_2=0}^3 \dots \sum_{j_m=0}^3 \mathbf{C}_{i_1 i_2 \dots i_m}^{j_1 j_2 \dots j_m} (j_1 x_1^{j_1-1}) x_2^{j_2} \dots x_m^{j_m} \\
\frac{\partial \Psi}{\partial x_2} \Big|_{x_1, \dots, x_m, t=\tau} &= \sum_{j_1=0}^3 \sum_{j_2=0}^3 \dots \sum_{j_m=0}^3 \mathbf{C}_{i_1 i_2 \dots i_m}^{j_1 j_2 \dots j_m} x_1^{j_1} (j_2 x_2^{j_2-1}) \dots x_m^{j_m} \\
&\dots \\
\frac{\partial \Psi}{\partial x_m} \Big|_{x_1, \dots, x_m, t=\tau} &= \sum_{j_1=0}^3 \sum_{j_2=0}^3 \dots \sum_{j_m=0}^3 \mathbf{C}_{i_1 i_2 \dots i_m}^{j_1 j_2 \dots j_m} x_1^{j_1} x_2^{j_2} \dots (j_m x_m^{j_m-1}) .
\end{aligned}$$

When $x_{1,i_1} \leq x_1 \leq x_{1,i_1+1}, \dots, x_{m,i_m} \leq x_m \leq x_{m,i_m+1}$

Equation 3-15

$$\begin{aligned}
\Psi_{\mathbf{xx}}(x_1, \dots, x_m, \tau) &= \begin{pmatrix} \frac{\partial^2 \Psi}{\partial x_1^2} & \frac{\partial^2 \Psi}{\partial x_1 \partial x_2} & \dots & \frac{\partial^2 \Psi}{\partial x_1 \partial x_m} \\ \frac{\partial^2 \Psi}{\partial x_2 \partial x_1} & \frac{\partial^2 \Psi}{\partial x_2^2} & \dots & \frac{\partial^2 \Psi}{\partial x_2 \partial x_m} \\ \dots & \dots & \dots & \dots \\ \frac{\partial^2 \Psi}{\partial x_m \partial x_1} & \frac{\partial^2 \Psi}{\partial x_m \partial x_2} & \dots & \frac{\partial^2 \Psi}{\partial x_m^2} \end{pmatrix} \\
\frac{\partial^2 \Psi}{\partial x_k^2} \Big|_{x_1, \dots, x_m, t=\tau} &= \sum_{j_1=0}^3 \sum_{j_2=0}^3 \dots \sum_{j_m=0}^3 \mathbf{C}_{i_1 i_2 \dots i_m}^{j_1 j_2 \dots j_m} x_1^{j_1} \dots [j_k (j_k - 1) x_k^{j_k-2}] \dots x_m^{j_m} \\
1 \leq k \leq m \\
\frac{\partial^2 \Psi}{\partial x_k \partial x_l} \Big|_{x_1, \dots, x_m, t=\tau} &= \sum_{j_1=0}^3 \sum_{j_2=0}^3 \dots \sum_{j_m=0}^3 \mathbf{C}_{i_1 i_2 \dots i_m}^{j_1 j_2 \dots j_m} x_1^{j_1} \dots (j_k x_k^{j_k-1}) \dots (j_l x_l^{j_l-1}) \dots x_m^{j_m} \\
1 \leq k, l \leq m, k \neq l .
\end{aligned}$$

When $x_{1,i_1} \leq x_1 \leq x_{1,i_1+1}, \dots, x_{m,i_m} \leq x_m \leq x_{m,i_m+1}$

And then calculate $\frac{\partial \Psi}{\partial t} \Big|_{\mathbf{x}, t}$ using Equation 3-16:

$$\begin{aligned} \frac{\partial \psi_1}{\partial t} \Big|_{\mathbf{x}, \tau} &= f_1(\Psi(\mathbf{x}, \tau), \Psi_{\mathbf{x}}(\mathbf{x}, \tau), \Psi_{\mathbf{xx}}(\mathbf{x}, \tau)) \\ &\dots \\ \frac{\partial \psi_n}{\partial t} \Big|_{\mathbf{x}, \tau} &= f_n(\Psi(\mathbf{x}, \tau), \Psi_{\mathbf{x}}(\mathbf{x}, \tau), \Psi_{\mathbf{xx}}(\mathbf{x}, \tau)) \end{aligned}$$

Equation 3-16

On the other hand, $\frac{\partial \psi}{\partial t} \Big|_{\mathbf{x}, t}$ is also given by Equation 3-11.

Step 4: Calculate the difference of $\frac{\partial \psi}{\partial t} \Big|_{\mathbf{x}, t}$ in Equation 3-16 and 3-11.

Equation 3-17

$$err = \sum_{i_1=0}^{N_1} \sum_{i_2=0}^{N_2} \dots \sum_{i_m=0}^{N_m} \sum_{k=1}^n \left\| f_k(\Psi(\mathbf{x}, \tau), \Psi_{\mathbf{x}}(\mathbf{x}, \tau), \Psi_{\mathbf{xx}}(\mathbf{x}, \tau)) - \left(\frac{\partial \psi_k}{\partial t} \Big|_{\mathbf{x}, 0} + \tau \cdot \frac{\partial^2 \psi_k}{\partial t^2} \Big|_{\mathbf{x}, 0} \right) \right\|_{\mathbf{x}=(x_{1i_1}, x_{2i_2}, \dots, x_{mi_m})}$$

In Equation 3-17, $\|\cdot\|$ means the norm of a scalar or vector, which can be absolute value or square or other forms. Here *err* is the difference of $\frac{\partial \psi}{\partial t} \Big|_{\mathbf{x}, t}$ between Equation 3-16 and 3-11. If $err < \varepsilon$, where ε is a predetermined small quantity, then $\Psi(\mathbf{x}, \tau)$ is a good approximation to the solution, and therefore go to Step 6 to conclude the solving process.

If $err > \varepsilon$, however, $\frac{\partial^2 \psi}{\partial t^2} \Big|_{\mathbf{x}, 0}$ needs to be refined in Step 5.

Step 5: According to Equation 3-17, $\frac{\partial^2 \psi}{\partial t^2} \Big|_{\mathbf{x}, 0}$ should satisfy the following condition to

make $err=0$:

$$\begin{aligned} \frac{\partial^2 \psi_k}{\partial t^2} \Big|_{\mathbf{x}, 0} &= \frac{1}{\tau} \left(f_k(\Psi(\mathbf{x}, \tau), \Psi_{\mathbf{x}}(\mathbf{x}, \tau), \Psi_{\mathbf{xx}}(\mathbf{x}, \tau)) - \frac{\partial \psi_k}{\partial t} \Big|_{\mathbf{x}, 0} \right) \\ 1 \leq k \leq n, \mathbf{x} &= (x_{1i_1}, x_{2i_2}, \dots, x_{mi_m}), 1 \leq i_1 \leq N_1, \dots, 1 \leq i_m \leq N_m \end{aligned}$$

Equation 3-18

Simply using Equation 3-18 to calculate new $\frac{\partial^2 \Psi}{\partial t^2} \Big|_{x,0}$ will often result in divergence of solution. Thus a less radical method is introduced to calculate the new $\frac{\partial^2 \Psi}{\partial t^2} \Big|_{x,0}$:

Equation 3-19

$$Z_k(x,0) = (1 - \omega) \frac{\partial^2 \psi_k}{\partial t^2} \Big|_{x,0} + \omega \cdot \frac{1}{\tau} \left(f_k(\Psi(x, \tau), \Psi_x(x, \tau), \Psi_{xx}(x, \tau)) - \frac{\partial \psi_k}{\partial t} \Big|_{x,0} \right)$$

Here ω is called ‘relaxation factor’. $Z_k(x,0)$ will be used as the new $\frac{\partial^2 \Psi}{\partial t^2} \Big|_{x,0}$, which is a linear combination of the old $\frac{\partial^2 \Psi}{\partial t^2} \Big|_{x,0}$ and the desired $\frac{\partial^2 \Psi}{\partial t^2} \Big|_{x,0}$ given by Equation 3-18.

Numerical experiments show that $\omega=0.2\sim 0.5$ result in fast convergence in most cases.

Having obtained the new $\frac{\partial^2 \Psi}{\partial t^2} \Big|_{x,0}$, i.e., $Z_k(x,0)$, go to Step 2 to recalculate $\Psi(x, \tau)$.

Step 6: Conclude the procedure.

If τ is too large, then the above iteration method may not converge. Therefore a constant, MNI (Max Number of Iterations), is set prior to the solving procedure. If the number of iterations exceeds MNI, then cut τ in half. First, solve $\Psi(x, \tau/2)$ from $\Psi(x,0)$. Then let $\Psi(x, \tau/2)$ be the new $\Psi(x,0)$, and solve the new $\Psi(x, \tau/2)$ from the new $\Psi(x,0)$. The new $\Psi(x, \tau/2)$ will be the solution to $\Psi(x, \tau)$. Similarly, if in either of the two steps the solution does not converge, the recursive time-division procedure will be conducted.

This algorithm is a modification of Finite Difference Method (FDM). Since it employs higher-order polynomial expansion to represent the solution, it maintains C^2 continuity of the solution with respect to x and t . The conventional FDM can only maintain C^0

continuity of the solution. In order to maintain smooth approximation to the real solution, conventional FDM has to take small time steps, while the algorithm discussed above can use much larger time steps.

In the above discussion, the solving procedure does not consider the boundary conditions Equation 3-6. The boundary conditions are considered in the process of representing $\Psi(x,0)$ and $\Psi(x,\tau)$ in splines, because solving coefficients of spline representation requires specifying boundary conditions of the functions[41].

3.4 Generalization of the Algorithm

The advantage of the algorithm is that it represents $\Psi(x,\tau)$ with smooth base functions, which are polynomials in the above sections, and thus smooth Ψ_{xx} can be obtained. The second order continuity of the representation of $\Psi(x,\tau)$ effectively enlarges the time steps needed to obtain sufficient solution precision, or in other words, reduces the number of time steps needed to obtain the solution.

The algorithm can be generalized by keeping the main scheme and changing the way of representing $\Psi(x,\tau)$. For example, $\Psi(x,\tau)$ can also be represented by sampling function *sinc*. From the point view of numerical solution, solving $\Psi(x,\tau)$ means computing a set of discrete sampling values of $\Psi(x,\tau)$ in the simulation domain given a set of initial discrete sampling values of $\Psi(x,\tau)$. The representation of $\Psi(x,\tau)$ gives the way of computing Ψ_x and Ψ_{xx} . In FDM, $\Psi(x,\tau)$ is represented by linear function of its sampling values, and thus Ψ_{xx} is 0 everywhere. In the above algorithm, $\Psi(x,\tau)$ is

represented by cubic splines, and thus $\Psi_{\mathbf{x}}$ is continuous everywhere, which is more physically realistic.

In general, the numerical algorithm for solving PDE discussed in this chapter can be described as following.

Suppose the PDE is described in Equation 3-4, and the initial sampling values are $\Psi(x_{1i_1}, x_{2i_2}, \dots, x_{mi_m}, 0)$, $1 \leq i_1 \leq N_1, \dots, 1 \leq i_m \leq N_m$. Here the discrete simulation domain S is given by

$$\text{Equation 3-20} \quad S = \{(x_{1i_1}, x_{2i_2}, \dots, x_{mi_m}) \mid 1 \leq i_1 \leq N_1, 1 \leq i_2 \leq N_2, \dots, 1 \leq i_m \leq N_m\}$$

The object of the algorithm is to compute $\Psi(x_{1i_1}, x_{2i_2}, \dots, x_{mi_m}, t)$, $1 \leq i_1 \leq N_1, \dots, 1 \leq i_m \leq N_m$.

Before starting the computing, two functions must be given to map from $\Psi(x_{1i_1}, x_{2i_2}, \dots, x_{mi_m}, \tau)$ to $\Psi_{\mathbf{x}}(x_{1i_1}, x_{2i_2}, \dots, x_{mi_m}, \tau)$ and $\Psi_{\mathbf{xx}}(x_{1i_1}, x_{2i_2}, \dots, x_{mi_m}, \tau)$, where τ is an arbitrary time. That is,

$$\begin{aligned} \text{Equation 3-21} \quad \mathbf{F}_{\mathbf{x}} : R^{N_1} \times R^{N_2} \times \dots \times R^{N_m} &\rightarrow R^{N_1} \times R^{N_2} \times \dots \times R^{N_m} \times R^m \\ \mathbf{F}_{\mathbf{x}}(\Psi(x_{1i_1}, x_{2i_2}, \dots, x_{mi_m}, \tau), 1 \leq i_1 \leq N_1, \dots, 1 \leq i_m \leq N_m) \\ &= \Psi_{\mathbf{x}}(x_{1i_1}, x_{2i_2}, \dots, x_{mi_m}, \tau), 1 \leq i_1 \leq N_1, \dots, 1 \leq i_m \leq N_m \end{aligned}$$

$$\begin{aligned} \text{Equation 3-22} \quad \mathbf{F}_{\mathbf{xx}} : R^{N_1} \times R^{N_2} \times \dots \times R^{N_m} &\rightarrow R^{N_1} \times R^{N_2} \times \dots \times R^{N_m} \times R^{m(m+1)/2} \\ \mathbf{F}_{\mathbf{xx}}(\Psi(x_{1i_1}, x_{2i_2}, \dots, x_{mi_m}, \tau), 1 \leq i_1 \leq N_1, \dots, 1 \leq i_m \leq N_m) \\ &= \Psi_{\mathbf{xx}}(x_{1i_1}, x_{2i_2}, \dots, x_{mi_m}, \tau), 1 \leq i_1 \leq N_1, \dots, 1 \leq i_m \leq N_m \end{aligned}$$

The procedure of computing $\Psi(x_{1i_1}, x_{2i_2}, \dots, x_{mi_m}, t)$ from $\Psi(x_{1i_1}, x_{2i_2}, \dots, x_{mi_m}, 0)$ is

Step 1: Calculate $\frac{\partial \Psi}{\partial t} \Big|_{\mathbf{x}, 0}$, $\mathbf{x} = (x_{1i_1}, x_{2i_2}, \dots, x_{mi_m}), 1 \leq i_1 \leq N_1, \dots, 1 \leq i_m \leq N_m$, from Equation

3-23:

$$\frac{\partial \psi_1}{\partial t} \Big|_{\mathbf{x},0} = f_1(\Psi(\mathbf{x},0), \Psi_{\mathbf{x}}(\mathbf{x},0), \Psi_{\mathbf{xx}}(\mathbf{x},0))$$

Equation 3-23

$$\frac{\partial \psi_n}{\partial t} \Big|_{\mathbf{x},0} = f_n(\Psi(\mathbf{x},0), \Psi_{\mathbf{x}}(\mathbf{x},0), \Psi_{\mathbf{xx}}(\mathbf{x},0))$$

$$\mathbf{x} = (x_{1i_1}, x_{2i_2}, \dots, x_{mi_m}), 1 \leq i_1 \leq N_1, \dots, 1 \leq i_m \leq N_m$$

Where $\Psi_{\mathbf{x}}(\mathbf{x},0), \Psi_{\mathbf{xx}}(\mathbf{x},0)$ are obtained through Equation 3-21 and 3-22.

Furthermore, let $\frac{\partial^2 \Psi}{\partial t^2} \Big|_{\mathbf{x},0} = 0$.

Step 2: Calculate $\Psi(x_{1i_1}, x_{2i_2}, \dots, x_{mi_m}, t)$, $1 \leq i_1 \leq N_1, \dots, 1 \leq i_m \leq N_m$, using the following equation:

$$\Psi(\mathbf{x}, t) = \Psi(\mathbf{x},0) + t \cdot \frac{\partial \Psi}{\partial t} \Big|_{\mathbf{x},0} + \frac{1}{2} t^2 \frac{\partial^2 \Psi}{\partial t^2} \Big|_{\mathbf{x},0}$$

Equation 3-24

$$\mathbf{x} = (x_{1i_1}, x_{2i_2}, \dots, x_{mi_m}), 1 \leq i_1 \leq N_1, \dots, 1 \leq i_m \leq N_m$$

Step 3: Calculate $\Psi_{\mathbf{x}}(\mathbf{x}, t), \Psi_{\mathbf{xx}}(\mathbf{x}, t)$, $\mathbf{x} = (x_{1i_1}, x_{2i_2}, \dots, x_{mi_m}), 1 \leq i_1 \leq N_1, \dots, 1 \leq i_m \leq N_m$, using Equation 3-21 and 3-22.

Step 4: Calculate the difference of $\frac{\partial \psi}{\partial t} \Big|_{\mathbf{x},t}$ obtained from spatial domain and from temporal domain:

Equation 3-25

$$err = \sum_{i_1=0}^{N_1} \sum_{i_2=0}^{N_2} \dots \sum_{i_m=0}^{N_m} \sum_{k=1}^n \left\| f_k(\Psi(\mathbf{x}, t), \Psi_{\mathbf{x}}(\mathbf{x}, t), \Psi_{\mathbf{xx}}(\mathbf{x}, t)) - \left(\frac{\partial \psi_k}{\partial t} \Big|_{\mathbf{x},0} + t \cdot \frac{\partial^2 \psi_k}{\partial t^2} \Big|_{\mathbf{x},0} \right) \right\|_{\mathbf{x}=(x_{1i_1}, x_{2i_2}, \dots, x_{mi_m})}$$

If $err < \epsilon$, go to **Step 6**, otherwise proceed to **Step 5**.

Step 5: Refine $\frac{\partial^2 \Psi}{\partial t^2} \Big|_{\mathbf{x},0}$ using Equation 3-26

Equation 3-26

$$Z_k(\mathbf{x},0) = (1 - \omega) \frac{\partial^2 \psi_k}{\partial t^2} \Big|_{\mathbf{x},0} + \omega \cdot \frac{1}{t} \left(f_k(\Psi(\mathbf{x},t), \Psi_{\mathbf{x}}(\mathbf{x},t), \Psi_{\mathbf{xx}}(\mathbf{x},t)) - \frac{\partial \psi_k}{\partial t} \Big|_{\mathbf{x},0} \right)$$
$$1 \leq k \leq n, \mathbf{x} = (x_{1i_1}, x_{2i_2}, \dots, x_{mi_m}), 1 \leq i_1 \leq N_1, \dots, 1 \leq i_m \leq N_m$$

Where ω is a predetermined relaxation factor.

$$\text{Let } \frac{\partial^2 \Psi}{\partial t^2} \Big|_{\mathbf{x},0} = Z_k(\mathbf{x},0), \text{ go to Step 2.}$$

Step 6: End the procedure.

If the number of iterations exceeds MNI (Max Number of Iterations), a predetermined integer constant, the time t is probably too large for the algorithm to converge. Then the problem should be recursively solved, i.e., first solve $\Psi(\mathbf{x}, t/2)$ from the initial condition $\Psi(\mathbf{x},0)$, and then solve $\Psi(\mathbf{x}, t)$ from the initial condition $\Psi(\mathbf{x}, t/2)$. Note that the PDE system is time-invariant.

3.5 Implementation of Post Exposure Bake Simulator with the Algorithm

A 2-dimensiona PEBS simulator named RIAR (Rapid Imaging Algorithm for Resist) has been implemented with the algorithm presented in Section 3.4-3.6. RIAR solves the following PDE system that describes the 2D PEBS model presented by M. Zuniga[23].

$$\frac{\partial C_{as}}{\partial t} = K_1(1 - C_{as})C_a^m$$
$$\text{Equation 3-27} \quad \frac{\partial C_a}{\partial t} = \frac{\partial}{\partial x} \left(D \frac{\partial C_a}{\partial x} \right) + \frac{\partial}{\partial y} \left(D \frac{\partial C_a}{\partial y} \right) - K_2 C_a$$
$$D = D_0 \exp(\omega C_{as})$$

Note that Equation 3-27 is the explicit 2D form of Equation 3-1, 3-2 and 3-3.

The initial photoacid concentration $C_a(x_i, y_j, 0), 1 \leq i \leq M, 1 \leq j \leq N$ should be given prior to the simulation process. The simulation domain is an M by N grid, which is not necessarily uniform. The initial activated site concentration is assumed to be 0 everywhere, i.e., $C_{as}(x_i, y_j, 0) = 0, 1 \leq i \leq M, 1 \leq j \leq N$. This assumption means no deprotection reactions occur before the PEB process. The assumption is valid if the thermal deprotection in room temperature can be ignored, or equivalently, the activation energy of the deprotection reaction is high enough. Note that the deprotection reaction, the photoacid loss process and the photoacid diffusion process all satisfy Arrhenius relations[42]:

$$\begin{aligned} K_1 &= K_{10} \exp(-E_{K1} / kT) \\ K_2 &= K_{20} \exp(-E_{K2} / kT) \\ D_0 &= D_{00} \exp(-E_{D0} / kT) \end{aligned}$$

Equation 3-28

Most resist systems satisfy the assumption that no thermal deprotection occurs in room temperature. Some low-activation-energy resists used in e-beam lithography, however, do not satisfy this assumption[38]. For these resist systems, the initial activated site concentration should be $C_{as}(x_i, y_j, 0) = c, 1 \leq i \leq M, 1 \leq j \leq N$, where c is a constant that can be experimentally determined.

RIAR uses cubic splines to approximate C_a and C_{as} , as is described in Section 3.4. In

RIAR, the boundary conditions for C_a and C_{as} are assumed to be periodical boundaries:

$$\begin{aligned} C_a(x + mL_x, y + nL_y, t) &= C_a(x, y, t) \\ C_{as}(x + mL_x, y + nL_y, t) &= C_{as}(x, y, t) \end{aligned}$$

Equation 3-29

Here the simulation domain is assumed to be $[0, L_x] \times [0, L_y]$.

The cubic spline representation of C_a and C_{as} can be solved under the restriction of periodical boundary Equation 3-29.

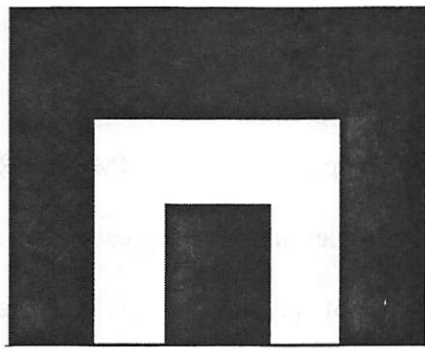
RIAR is written in standard MATLAB code and runs in both UNIX and Windows platforms.

3.6 Performance Comparison of RIAR and STORM

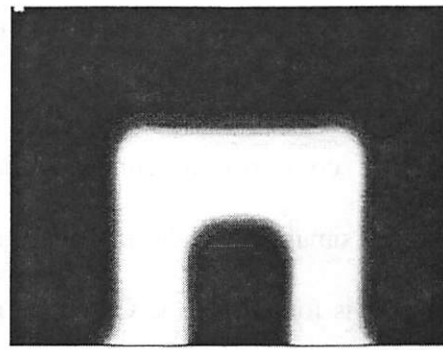
STORM developed by E. Croffie uses Finite Element Method (FEM) to solve the PEB model described by Equation 3-27. To compare the computational performance of STORM and RIAR, the advantage of the algorithm described in this chapter over conventional algorithms can be demonstrated.

The following discussion is based on APEX-E resist, whose PEB parameters are listed in [43], $K_1=1.9187$, $K_2=0.0049$, $m=1.7$, $D_0=2 \times 10^{-4} \mu\text{m}^2/\text{s}$, $w=1$, bake time $t=60\text{sec}$, bake temperature $T=90^\circ\text{C}$. The simulations were run on a 600MHz Alpha DEC Workstation.

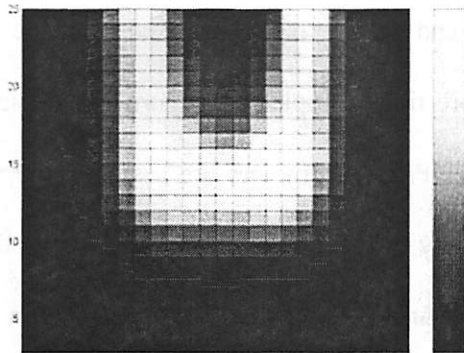
Figure 3-1 compares the output of RIAR with STORM. Figure 3-1 (a) is the mask pattern, which is input to SPLAT to obtain the light intensity distribution at the top surface of the resist layer. Then the light intensity, shown in Figure 3-1 (b), is converted into acid concentration C_a using Dill's ABC model [28]. The activated site concentration C_{as} , as a result of post exposure bake, is simulated using STORM and RIAR, respectively. Figure 3-1 (c) and (d) show the activated site concentration obtained by STORM and RIAR, respectively. It can be seen that the difference between the two simulations is quite small. Further numerical analysis shows that the RMS error between STORM and RIAR is less than 2%.



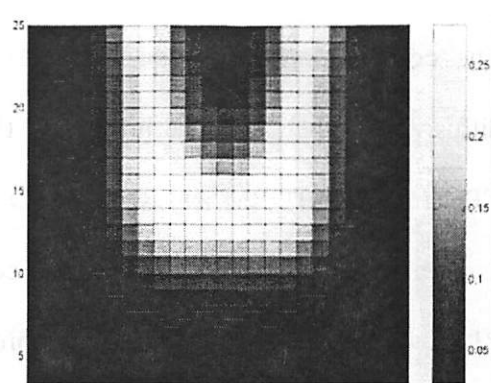
(a)



(b)



(c)



(d)

Figure 3-1 Comparison outputs of STORM and RIAR.

(a) is the mask pattern, (b) is the light intensity at the resist surface obtained through SPLAT, (c) and (d) are the activated site concentration at the resist surface obtained by STORM and RIAR, respectively.

The computational time of post exposure bake simulations are affected by several factors such as simulation domain size, reaction rate K_1 , diffusivity D_0 and exponential diffusivity constant ω , and so on. When discussing the impact of these factors on computational time complexity, it must be noted that the UNIX workstation was not fully dedicated to the PEB simulation tasks. A heavy-duty PEB simulation usually takes a

share of 40% ~ 90% CPU time, hence the computational times shown in this chapter have been averaged.

Figure 3-2 compares the computational time complexity of STORM and RIAR with respect to simulation scale, i.e., the number of nodes used to represent the x - y spatial domain. It is found that the CPU time complexity of STORM is $O(N^2)$, whereas that of RIAR is $O(N^{1.38})$. Here N is the number of nodes. As a result, the computational time of RIAR is 1/7 ~ 1/5 that of STORM in a medium-scale simulation (600~900 nodes).

The computational times of both STORM and RIAR highly depends on the initial diffusivity, namely D_0 . The higher D_0 , the more time complexity. Figure 3-3 depicts the CPU time of STORM and RIAR vs. D_0 . Other PEB parameters are assigned the values listed above. It is found that the time complexity of STORM is $O(D_0^{0.14})$, while that of RIAR is $O(D_0^{0.70})$. High diffusivity forces the time step in the RIAR algorithm to be small so as to achieve certain precision, thus introduces more time complexity.

It can be seen that the computational time of RIAR exceeds STORM when $D_0 > 700 \text{nm}^2/\text{s}$. $D_0 = 500 \text{nm}^2/\text{s}$ with a bake time of 60s corresponds to a diffusion length of 173nm, which is too large for current commercial resists designed for sub-200nm lithography. At this D_0 , RIAR achieves half computational time that of STORM. Thus in practical applications, RIAR can maintain its high-speed advantage to STORM.

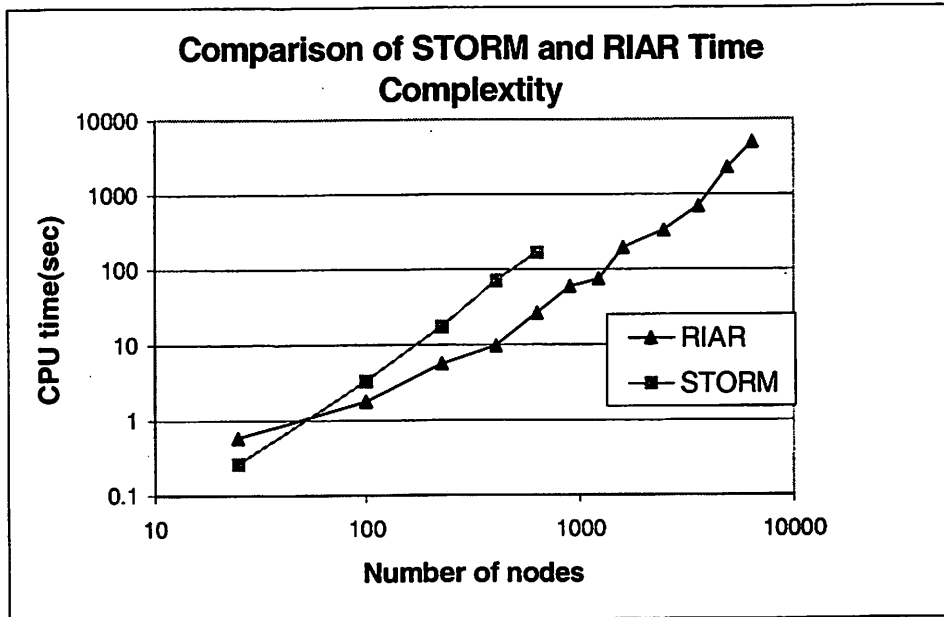


Figure 3-2 Comparison of CPU time of STORM and RIAR.

The time complexity of STORM is $O(N^2)$, while that of RIAR is $O(N^{1.38})$. Note that the STORM can not simulate more than 700 nodes due to its large memory consumption

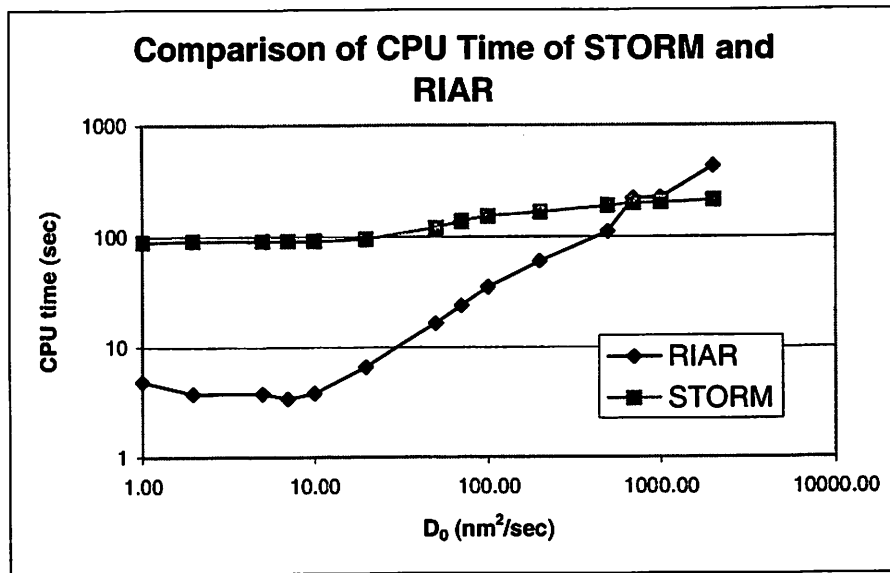


Figure 3-3 Comparison of CPU time of STORM and RIAR vs. D_0 .

All the other PEB parameters take the values of the APEX-E resist given in [43]. The simulation domain is 25*25 grid.

Neither STORM nor RIAR is significantly dependent on reaction rate, namely K_1 , as depicted in Figure 3-4. The CPU time consumption of STORM slowly increases as K_1 increases, while that of RIAR is almost a constant.

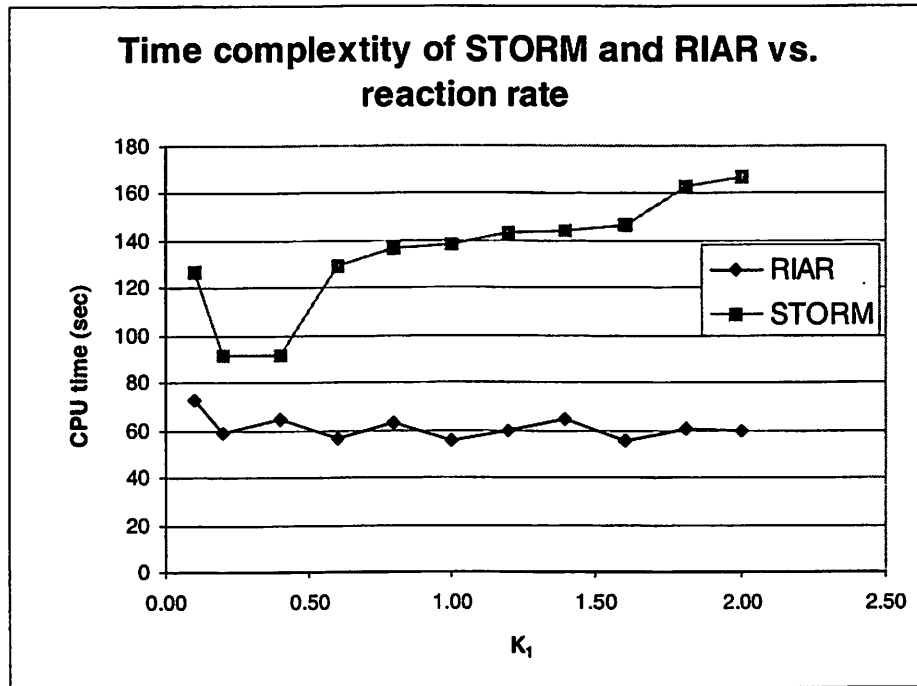


Figure 3-4 Comparison of CPU time of RIAR and STORM vs. K_1 .

All the other PEB parameters are assigned the values of APEX-E resist in [43]. The simulation domain is 25*25 grid. Note that the CPU times does not monotonically vary with K_1 , which is possibly caused by fluctuation of CPU time allocation in the UNIX workstation.

The exponential diffusion coupling coefficient ω does not significantly affect the performance of STORM or RIAR, as is depicted in Figure 3-5. This is surprising because the nonlinear diffusion part is expected to be among the most significant factors affecting the simulators' performance. This can be explained by the fact that C_{as} is always small in

APEX-E resist, the maximum C_{as} at the end of simulation is 0.3, which increases the diffusivity by $\exp(1 \times 0.3) - 1 = 0.35$, i.e., 35%. This increment is not large enough to significantly slow down the simulation. We would expect, however, ω will significantly affect the performance of the simulator in the case of large C_{as} .

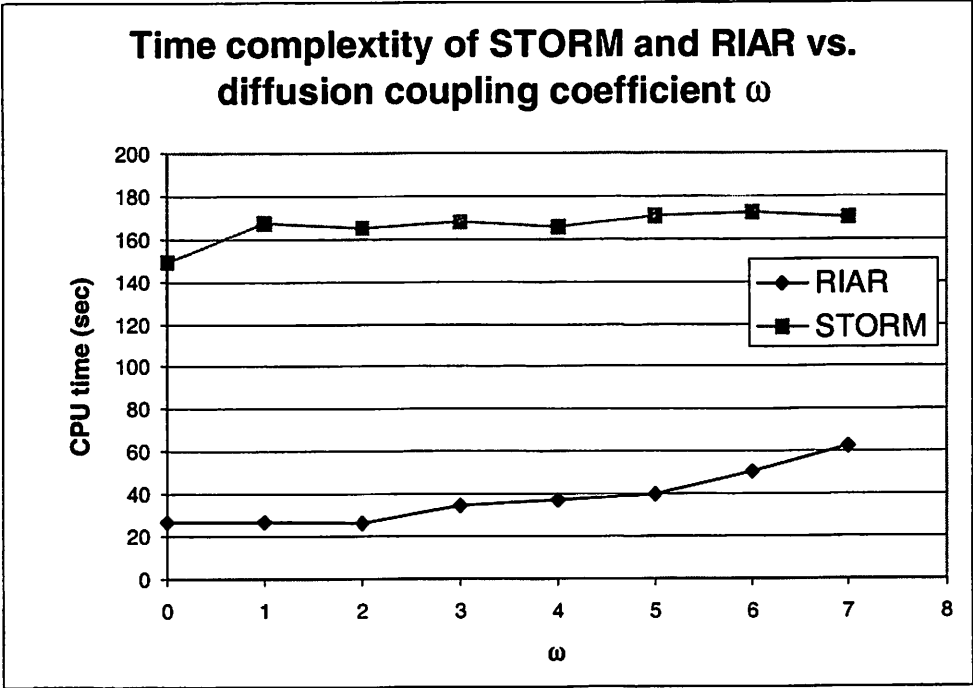


Figure 3-5 Comparison of CPU time of RIAR and STORM vs. ω .

All the other parameters take the values of APEX-E in [43]. The simulation domain is 25*25 grid. Note that the CPU time of RIAR and STORM is affected only slightly by ω .

The convergence speed and precision can be tuned by adjusting the allowed error, namely ϵ in Section 3.5. Generally, the more precision, the lower the convergence speed. As is depicted in Figure 3-6, the computational time only increases by 43% when ϵ decreases from 10^{-2} to 10^{-10} , which indicates the efficiency of RIAR is not sensitive to the precision requirement.

RIAR has much higher memory efficiency than STORM. It consumes only 1% memory that of STORM, which makes RIAR suitable for large-scale simulations. As a comparison, STORM can only run less-than-700-node simulations on a 600MHz, 512MB DEC Alpha workstation, while RIAR can run more-than-10000-node simulations without memory allocation problem.

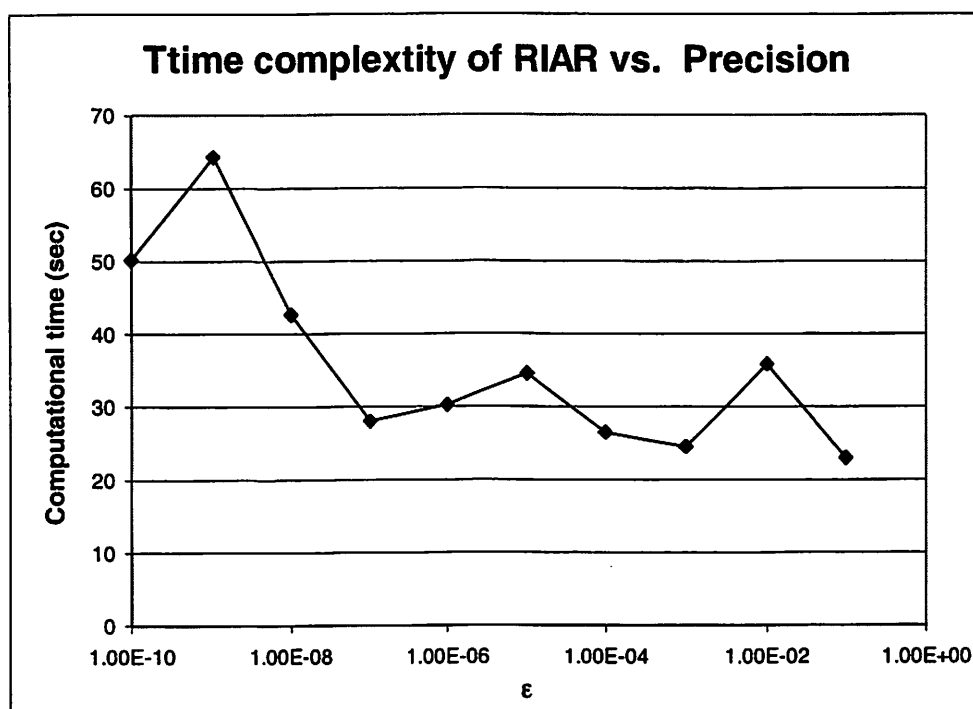


Figure 3-6 Comparison of CPU time of RIAR vs. precision requirement.

All the PEB parameters take the values of APEX-E resist in [43]. The simulation domain is 25*25 grid. Note that the CPU time does not monotonically vary with ϵ , which may be due to the fluctuation of CPU allocation in the UNIX workstation.

3.7 Application of RIAR in Line-End Shortening Simulations

It has been observed that there exists line-end shortening (LES) in both lines and trenches when the linewidth is under $0.2\mu\text{m}$. RIAR can be used to simulate the LES. As an example, two types of features on UVII resist were simulated and compared. One is dense lines, linewidth $0.15\mu\text{m}$, pitch $0.3\mu\text{m}$, end-to-end spacing $0.22\mu\text{m}$. The other has the same geometry but different polarity, i.e., it is printed as trenches. The resist parameters are $K_1=1.56$, $K_2=0$, $m=1$, $D_0=0.6\text{nm}^2/\text{s}$, $\omega=0$, resist thickness is $0.7\mu\text{m}$.

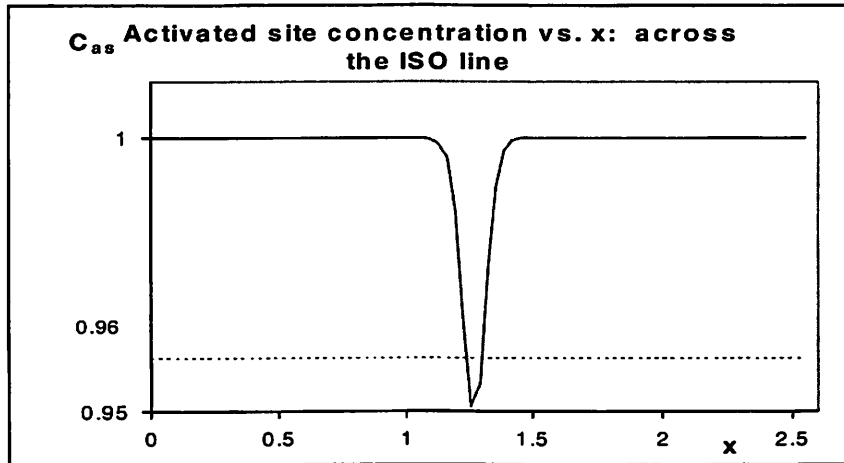
The simulation flow is as follows:

First, the image intensity profile $I(x,y)$ on the plane which is $0.35\mu\text{m}$ below the resist top surface is obtained through SPLAT. Then the image profile $I(x,y)$ is converted into the acid concentration $C_a(x,y)$ using Dill's ABC model. $C_a(x,y)$ is then input into RIAR to start the post exposure bake simulation which output the activated site concentration profile $C_{as}(x,y)$. Finally a threshold model is used to determine the LES, i.e., given a threshold TH , $0 < TH < 1$, the resist on which $C_{as} > TH$ is developed, while the resist on other area is not cleaned.

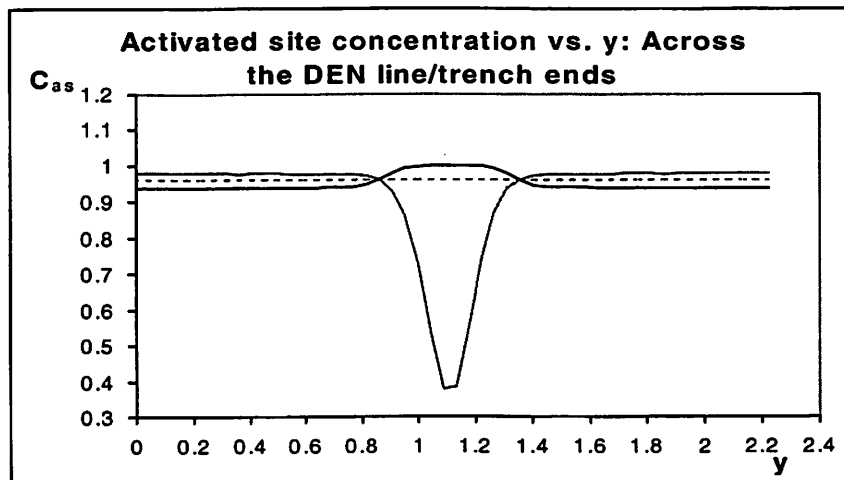
The threshold TH is found by being tuned to satisfy the assumption that a $0.15\mu\text{m}$ -wide isolated line is actually $0.16\mu\text{m}$ -wide after develop. This is a common anchoring criterion used in fab. The excessive $0.01\mu\text{m}$ width is used to compensate the etch bias, which is the resist CD shrinkage due to etch process.

Figure 3-7 (a) shows the activated site concentration across the $0.15\mu\text{m}$ -wide line. It was found that $TH=0.96$ is the proper threshold. Figure 3-7 (b) shows the activated site

concentration across the two line/trench ends. Using $TH=0.96$, it was found that the separations between the line/trench ends are $0.40\mu\text{m}$, corresponding to $0.18\mu\text{m}$ double-side LES. This LES agrees well with the experimental data from Texas Instruments.



(a)



(b)

Figure 3-7 Simulation of dense lines/trenches. Both have significant LES.

(a) shows the activated site concentration across the linewidth. $TH=0.96$ is found to be the proper threshold that makes $0.15\mu\text{m}$ line printed as $0.16\mu\text{m}$. (b) shows the activated site concentration across the line ends. The dotted line is $C_{as}=TH=0.96$.

3.8 Conclusions

In this chapter, a rapid numerical algorithm for solving partial differential equations is described and implanted in RIAR, a 2-dimensional post exposure bake simulator. The algorithm represents the solution to PDE system using cubic splines and then solves the coefficients of cubic splines iteratively. Due to the second order continuity of cubic spline representation, much larger time steps can be achieved, compared with FDM.

Compared to STORM, RIAR significantly reduces the simulation time to $1/7 \sim 1/5$. Furthermore, it consumes less than 1% memory space of STORM. Thus RIAR makes large-scale PEB simulations possible. The time complexity of RIAR and STORM are compared with respect to simulation scale, diffusivity, reaction rate, etc. Both of their time complexities highly depends on the initial diffusivity of the resist. For the resists of interest ($D_0 < 5 \times 10^{-4} \mu\text{m}^2/\text{s}$), RIAR consumes less than 1/5 CPU time than STORM does. The value of reaction rate does not significantly affect the performance of RIAR and STORM. The exponential diffusion coupling coefficient, ω , increases the CPU time of RIAR by 140%, STORM by 14%, when ω increases from 0 to 7. Even at $\omega=7$, which is very highly nonlinear, CPU time of RIAR is still 1/3 that of STORM.

The speed and precision of RIAR can be tuned by controlling the preset allowed error ε . When the error changes from 10^{-2} to 10^{-10} , the CPU time only increases by 43%. Hence RIAR can achieve very high precision without much loss in simulation speed. Finally an example of line-end shortening simulation through RIAR is given.

4 Automatic Resist Parameter

Extraction by Pattern Matching

4.1 Introduction

ArF resist imaging is rapidly maturing and a predictive modeling capacity that includes both the chemically-amplified resist and imaging quality is needed to guide manufacturing. To accurately describe the scanner/resist system, several systematic error factors have to be addressed, such as mask error, resist response to defocus, lens imperfection, etc. A physical lithographic model is expected to resolve these complications and predict printed patterns effectively. The pattern distortion effects, such as corner rounding and line-end shortening (LES), which are exacerbated in the extension of optical lithography into deep 100-nm regime, are increasingly important in ensuring lithographic quality, and conventional single number metrics such as critical dimension (CD) of a feature may not be adequate. Thus it is desired to quantitatively describe LES with 2-dimensional metric and, with this metric, evaluate and optimize simulation models.

On the other hand, traditional rule-based Optical Proximity Correction (OPC) technique has been inadequate in deep-100nm regime[44]. Model-based OPC is relatively more accurate in reflecting the lithography processes, but is more computationally intensive[45]. In industrial applications, OPC models are tuned to fit a set of experimental data such as line/space width and line-end pullback,, which are basically 1-

dimensional metrics. Then the models are applied to generate corrected reticle from original layout. By sampling enough line/space CD in tuning the OPC models, the corrected mask usually results in tolerable CD's printed on wafers. However, the calibration of OPC models is unable to take into account the 2-dimensional random structure. Thus the printed patterns may have some 2-dimensional distortions, which can fail the devices, such as line-end shortening, corner rounding, bridging and scum, even though the line CD's are correct. This problem becomes more and more severe with more random logic devices being packed onto a chip. The extension of OPC to 2-dimensional, i.e., calibrating models with 2D patterns instead of 1-dimensional CD's, could be a solution to ensure correct pattern transfer in sub-100nm lithography.

In this chapter, an algorithm for extracting monochromatic representation of resist patterns from SEM pictures is initially presented and then a scheme for comparing the experimental resist patterns with simulated images is discussed. Image Mismatching Factor (IMF), a 2-dimensional metric for evaluating the simulation model performance, is also defined. A framework for tuning simulation models is then built based on optimizing IMF. On the basis of the above methodology, several levels of physical assumptions in simulation models were optimized and their IMF's were compared. These models were then applied to a much smaller pattern to evaluate their predictabilities. The impact of factors leading to pattern feature distortion, including lens aberrations, resist optical and PEB parameters, on IMF are then discussed.

4.2 Concept of Pattern Matching

As is discussed in Section 4.1, a systematic approach is desired to quantitatively compare the difference of a simulated image and an SEM picture and obtain a metric to describe the difference. In image processing, a concept termed Signal to Noise Ratio (SNR) is used to describe the difference of two gray-scaled images[47]. Suppose the two images have $M \times N$ pixels, and their intensities at the pixels are $A(i, j)$ and $B(i, j)$, respectively, where $1 \leq i \leq M, 1 \leq j \leq N$. Here we assume $B(i, j)$ is the standard sample, and $A(i, j)$ is the sample to be compared with $B(i, j)$. Then their difference is given by

$$\begin{aligned} \Delta(i, j) &= A(i, j) - B(i, j) \\ 1 \leq i \leq M, 1 \leq j \leq N \end{aligned}$$

Equation 4-1

Their difference is quantitatively described by a 1D metric, SNR , which is defined as

$$SNR = \frac{\sum_{i=1}^M \sum_{j=1}^N \Delta^2(i, j)}{\sum_{i=1}^M \sum_{j=1}^N B^2(i, j)}$$

Equation 4-2

Consider $\Delta(i, j)$ to be the error and consider $B(i, j)$ to be the signal, then SNR defined in Equation 4-2 is actually the ratio of error energy to the signal energy.

Though SNR is a good metric to evaluate the difference of two images, it must be modified for lithography applications. After the lithography process, the resist on wafer is either “developed” or “undeveloped”, and therefore the resist patterns of interests can be characterized by a monochromatic image, i.e., a black/white image. On the other hand, the SEM pictures of resist patterns are generally 256-gray-scaled images. In order to quantitatively calculate the difference between SEM pictures and simulated images, it is

necessary to quantize the SEM pictures into 2 levels, or white and black, which correspond to remaining resist and cleared region, respectively. Similarly, the simulated images are to be quantized into two levels, corresponding to “developed” and “undeveloped” resist. The quantization of simulated images is usually accomplished by a threshold model, as is described in Chapter 2.

Now let $B(i, j)$ be the monochromatic representation of a SEM picture, and let $A(i, j)$ be the monochromatic version of the corresponding simulated image. Then $A(i, j) = 1, 0$ and $B(i, j) = 1, 0$, $1 \leq i \leq M, 1 \leq j \leq N$. Now the difference of the two images is given by Equation 4-1. However, now $\Delta^2(i, j)$ is either 1 or 0. The value of 1 or 0 is just a symbol of “undeveloped” or “developed”, and means energy to some extent. Based on the definition of *SNR*, we define a new metric to evaluate the difference $\Delta(i, j)$ termed “Image Mismatch Factor”, short IMF, which is calculated by

Equation 4-3

$$IMF = \frac{\sum_{i=1}^M \sum_{j=1}^N \Delta^2(i, j)}{\sum_{i=1}^M \sum_{j=1}^N B(i, j)} = \frac{\sum_{i=1}^M \sum_{j=1}^N |\Delta(i, j)|}{\sum_{i=1}^M \sum_{j=1}^N |B(i, j)|}$$

It can be considered as the percentage of pixels at which image A and B are different.

The process of quantizing and comparing the images is depicted in Figure 4-1.

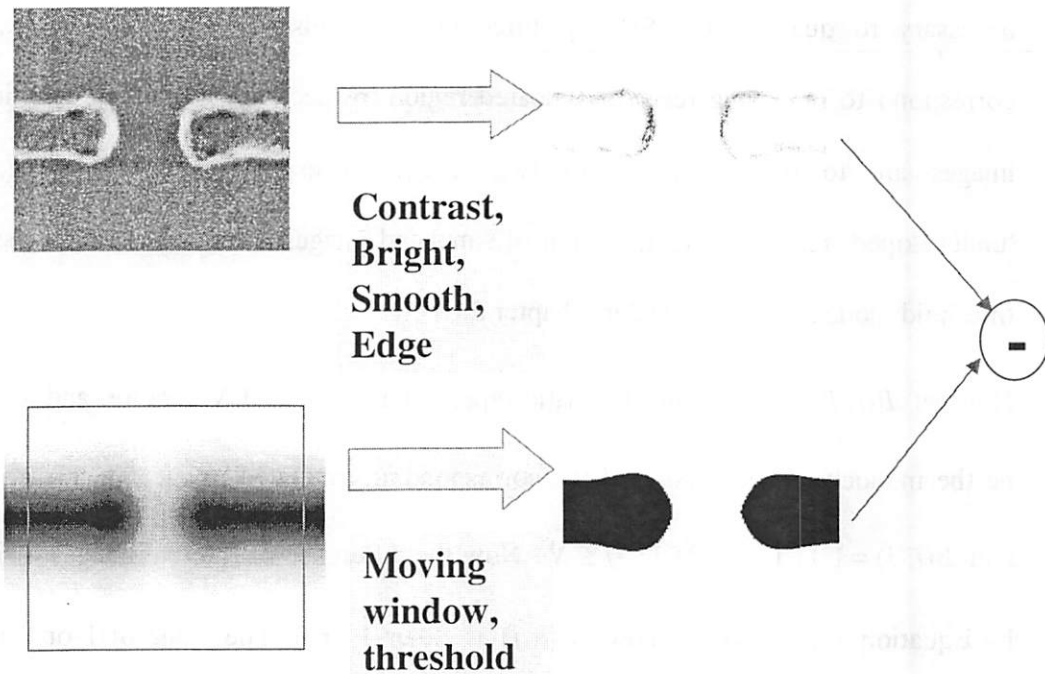


Figure 4-1 The diagram of SEM/SIM comparator

The SEM picture, shown at the upper part, is quantized into a black/white picture, representing remaining resist or cleared area. The simulated image, shown at the lower part, is also quantized into a monochromatic picture. Then IMF is calculated.

4.3 Converting SEM Pictures to Monochromatic

The algorithm for making SEM pictures monochromatic is described as below:

Step 1: Edge detection. Given a gray-scaled SEM picture, denoted as $I = (I_{mn})$, $1 \leq m \leq M$, $1 \leq n \leq N$, where M and N are the height and width of the image in number of pixels. Assume the image has 256 gray levels, i.e., $0 \leq I_{mn} \leq 255$, 0 corresponds to the darkest pixels and 255 corresponds to the brightest pixels. The edges of the resist patterns

are usually the brightest pixels in a SEM picture. Therefore the edge detector can be defined as a threshold detector:

$$\text{Equation 4-4} \quad D[I, Th] = J = (J_{mn}), J_{mn} = \begin{cases} 1 & \text{if } I_{mn} > Th \\ 0 & \text{if } I_{mn} \leq Th \end{cases}$$

Here Th is a predetermined threshold. After edge detection, the SEM image I is converted into a monochromatic image J , in which 1's are the edges of the resist patterns, as is depicted in Figure 4-2 (b).

Other edge detection algorithms, including Roberts algorithm, Laplacian operator and so on, can also be used and may result in better image of edges. However, they are more computationally intense. So the simple threshold edge detection is used in this thesis. The detailed description of other edge detection algorithms can be found in [47].

Step 2: Noise removal. As can be seen in Figure 4-2 (b), there are some random pixels in J whose values are 1. These noisy pixels are usually caused by resist non-uniformity or SEM shot noise. They can be removed by an averaging filter [47] followed by a threshold detector:

$$\text{Equation 4-5} \quad K = J * H, H = \frac{1}{12} \begin{pmatrix} 1 & 1 & 1 \\ 1 & 4 & 1 \\ 1 & 1 & 1 \end{pmatrix}$$

Here "*" is convolution. H is the moving average window matrix [47].

$$\text{Equation 4-6} \quad L = D[K, NT] = (L_{ij}), L_{ij} = \begin{cases} 1 & \text{if } K_{mn} > NT \\ 0 & \text{if } K_{mn} \leq NT \end{cases}$$

Here NT is also an adjustable threshold between noise and real edges. In this chapter NT is taken as 0.5. The image after noise removal is shown in Figure 4-2 (c).

Step 3: Filling the region inside the edges. It is desired to differentiate the remaining resist from the cleared region by assigning the pixels of the dark region the value of 1 while assigning other pixels the value of 0. After Step 1 and 2, the edges are assigned the value of 1 while other areas are assigned the value of 0. Now we need to fill all areas inside the edges with color 0. There have been many mature filling-area algorithms which can be found in [48]. In this thesis the simplest scan-line polygon fill algorithm [48] was employed. The image after filling was shown in Figure 4-2 (d). Denote the image as P .

Step 4: Clipping proper image. Generally only a particular part of the SEM image is of interest. As is in Figure 4-2 (d), only the region outlined by the dotted lines is needed to compare with simulation, because it is the critical feature of this pattern. The clip of interest is characterized by the coordinates of its center, (x_0, y_0) , which is termed “alignment mark”, and its width W and height H . That is, the clip is

Equation 4-7

$$Q = \begin{pmatrix} P_{x_0 - \frac{H}{2}, y_0 - \frac{W}{2}} & \cdot & \cdot & \cdot & P_{x_0 - \frac{H}{2}, y_0 + \frac{W}{2}} \\ \cdot & \cdot & \cdot & \cdot & \cdot \\ \cdot & \cdot & P_{x_0, y_0} & \cdot & \cdot \\ \cdot & \cdot & \cdot & \cdot & \cdot \\ P_{x_0 + \frac{H}{2}, y_0 - \frac{W}{2}} & \cdot & \cdot & \cdot & P_{x_0 + \frac{H}{2}, y_0 + \frac{W}{2}} \end{pmatrix}$$

The alignment mark is usually found by searching for a pixel that satisfies some given conditions. In this particular pattern, the alignment mark is defined as the pixel that is equidistant to the two resist lines. Here the distance of a point p to a set of points B is

defined as $d(p; B) = \min\{|p - b| \mid \forall b \in B\}$. If more than one pixel satisfies the condition, their mass center is taken as the alignment mark. The alignment mark in Figure 4-2 (d) is marked by “*”.

Note that the extraction process for a SEM picture is conducted only once, thus the computational complexity is not of particular concern.

After the above four steps, a black/white image Q has been obtained, which will be compared with simulated images. Note that by the above method of choosing pattern edges, the filled patterns will be bordered by the outmost edges. This means Q is corresponding to the profile at the bottom of the remaining resist.

4.4 SEM/SIM Comparator and Model Tuner

Given a simulation output, no matter if it is an aerial image or an activated site concentration, it can be treated with a threshold model to obtain a monochromatic representation of the resist patterns after development. This means resist for which the simulated value is higher than a given threshold is considered to dissolve, and otherwise the resist is considered to remain.

For the purpose of comparing SEM's with simulation, it is necessary to clip the simulated image with the same window defined in Section 4.3, step 4. The clipping process is essentially identical. Note that in the presence of lens aberration, the simulated image is no longer symmetric, thus the coordinates of the alignment mark can not be determined in advance of simulation.

The clipped simulated image is denoted as R , which is also a black/white image. After obtaining the monochromatic representations of the SEM picture and simulated image, namely Q and R , the Image Mismatching Factor (IMF), a 2D metric evaluating the error of the simulation is given by:

Equation 4-8

$$IMF = \frac{\sum_i \sum_j |R_{ij} - Q_{ij}|}{\sum_i \sum_j Q_{ij}}$$

Note that the numerator represents the area in which the simulation does not agree with the SEM picture, whereas the denominator represents the area of the resist patterns in the SEM picture. An example of comparing SEM with the simulation is shown in Figure 4-3.

The simulation model can now be optimized using this metric. The optimization process is depicted in Figure 4-4. The simulation is iterated with a different set of parameters until IMF is minimized. A number of algorithms can be used to find the optimum of a given irregular function, for example, Direct Search Method, Newton-Gauss Gradient Search, Simulated Annealing[49]. In this thesis, the Method of Feasible Direction[12] is used for its simplicity, stability and ability of reaching at least local optimum.

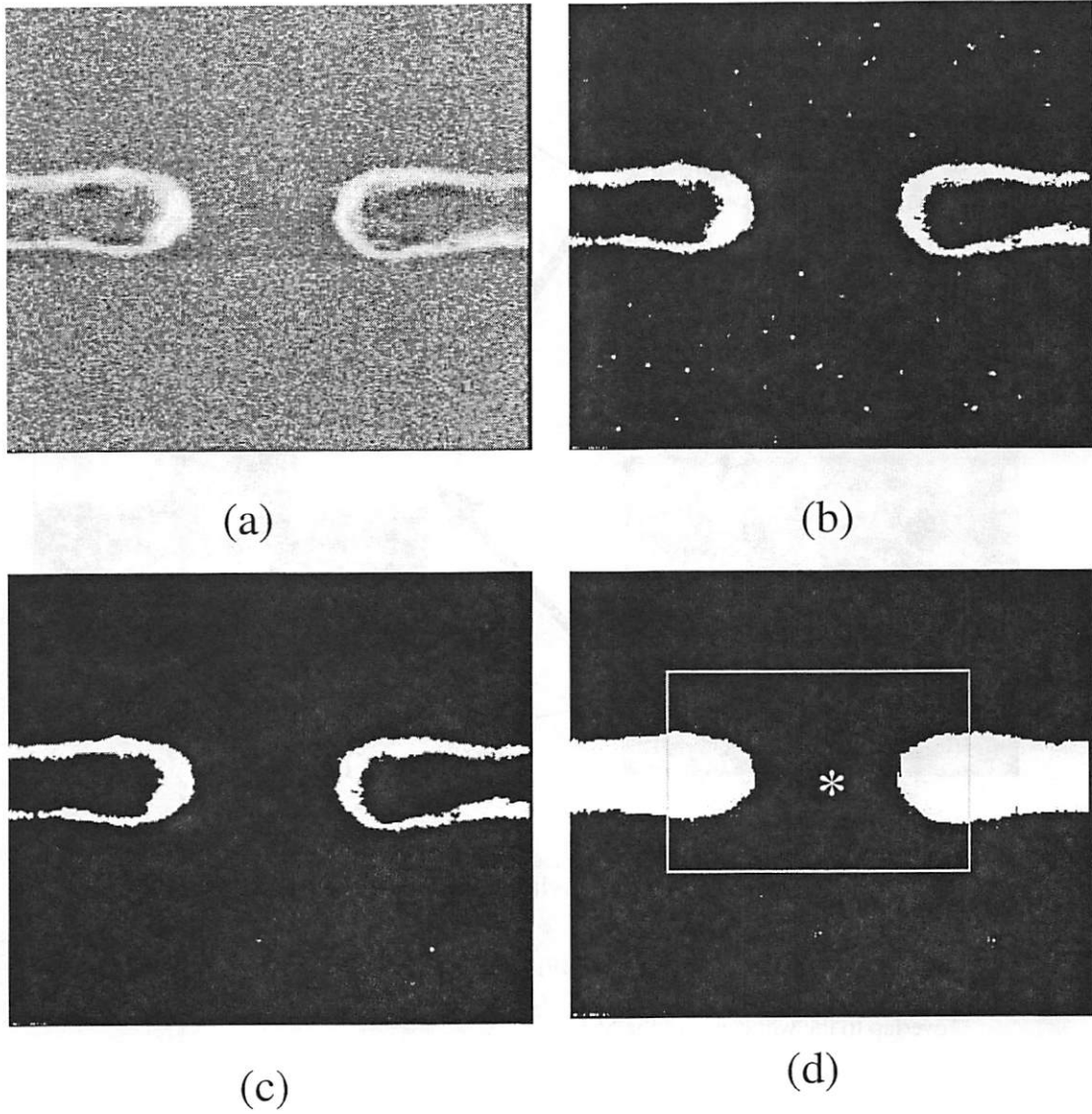


Figure 4-2 The process of extracting black/white representations from SEM pictures.

Here, (a) SEM picture, (b) image after extracting the edges, (c) image after removal of noise, (d) image after filling the area inside the edges. In (d) the alignment mark is highlighted by “*”.

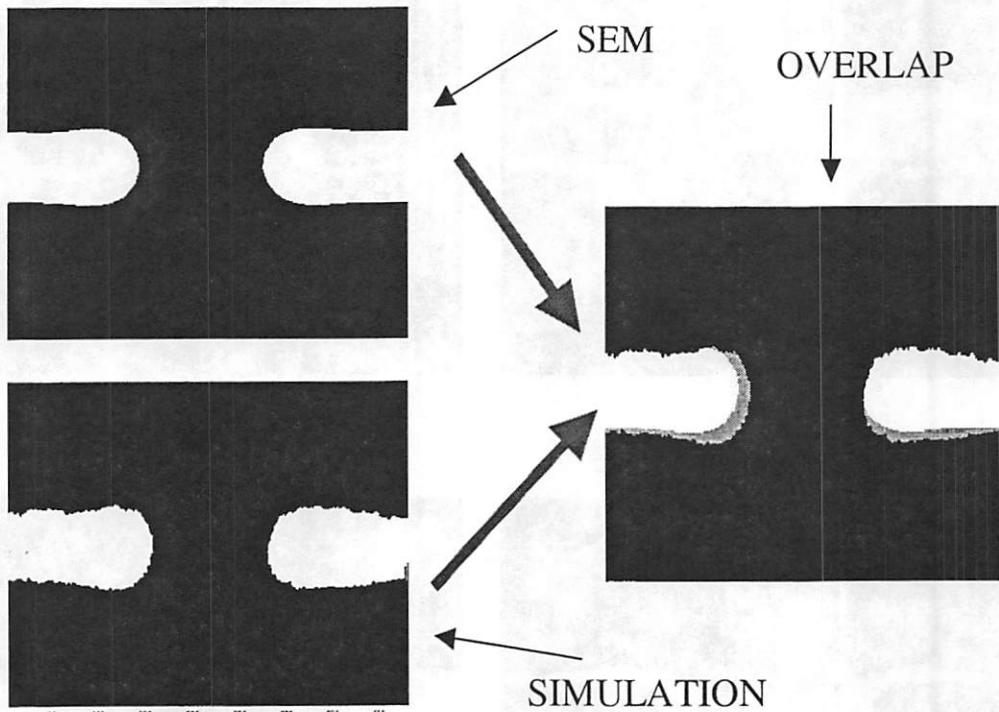


Figure 4-3 Overlaying SEM with simulated image.

The Image Mismatching Factor (IMF) is defined as the ration of the dark area in the overlap to the white area of the SEM.

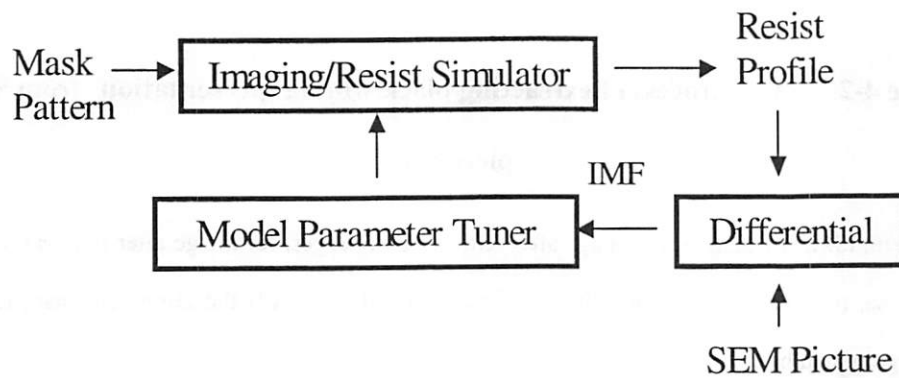


Figure 4-4 The framework for tuning models based on minimizing IMF.

4.5 Conclusions

The algorithm for extracting monochromatic representation of resist patterns from SEM pictures is presented in this chapter. At present the computational complexity of the algorithm is not critical since it needs to be run only once for each SEM picture. The Image Mismatching Factor (IMF) is introduced as a 2-dimensional metric for evaluating the simulation model performance. Furthermore, a framework for tuning simulation models is built. With the fast algorithm presented in Chapter 3 and the model calibration/evaluation framework presented in this Chapter, a comprehensive model of projection lithography can be implemented and thereafter the sources contributing to pattern distortions can be identified, which is the main theme of this thesis and will be discussed in details in Chapter 5.

5 Modeling Projection Lithography through Resist Simulation and Pattern Matching

5.1 Introduction

With the IC device dimensions approaching 100nm regime and ArF imaging technology rapidly maturing, a comprehensive model of projection lithography is needed to identify the systematic error factors in printing process including mask variation, lens imperfection and resist chemistry, and guide manufacturing processes. Furthermore, the extensive use of Resolution Enhancement Technique (RET) greatly boosts the need of a fast, predictive and physical model to ensure that the RET designs reach CD targets and have enough process latitude. For example, current OPC models are extracted from 1-dimensional CD measurements, including linewidth, space width and so on. The extrapolation of these OPC models to 2D random logic devices might result in poor imaging quality and small process latitude, which may fail the devices. The unwanted pattern distortion phenomena, such as corner rounding and line-end shortening (LES), exacerbated in the extension of optical lithography into deep 100-nm regime are increasingly important in ensuring lithographic quality. A predictive model of 2D random pattern printing is therefore desired to avoid the failures of OPC models.

In Chapter 2, a physical model of stepper/resist system simulation using SPLAT and STORM is described, which has been proved effective in predicting LES in 248nm resists[43]. Compared with 248nm resists, 193nm resists are still immature and have some unwanted properties such as large line-edge roughness (LER), poor resist adhesion and resist slimming during Scanning Electron Microscope (SEM) measurements[50][5], which presents great challenge to the application and modeling of ArF lithography. As a consequence, current production-oriented modeling work of 193nm lithography usually focuses on one particular dose and best focus and tries to predict the critical dimensions (CDs) of different patterns through rapid numerical models including diffused aerial image model[51][52], variable threshold model [34][35] and so on. It is the process engineers' responsibility to select the best dose and focus so as to provide large enough process latitude and minimize the impacts of the systematic errors in simulation models [54]. This methodology can ensure line CD control within 5% variation but may fail in capturing the 2-dimensional pattern distortions which result in unwanted scum, bridging, etc.[54] Furthermore, the simulation errors can be magnified by the dose/defocus bias brought forth by non-uniform wafer planarity or tool-dependent lens aberrations. Thus the process latitude may be unexpectedly poor when using reticles corrected by this methodology[55]. On the other hand, lithography engineers have been using physical-model-based simulators such as PROLITH [56] and SOLID-C [57] to evaluate the feasibility of process setup and predict the through-dose, through-focus printing results of mask patterns. Although the simulators capture the trends of printing results as process or reticle varies, they generally are not used to predict pattern CDs if certain accuracy is

required due to the large number of their model parameters to be calibrated and the time-consuming simulation process.

To provide a solid base for characterizing the major process factors in 193nm lithography and predicting the pattern transfer quality, this chapter begins with a rapid physical model combining the advantages of the above two methodologies. A predictive, physical and feasible model is expected to have the following properties:

- 1) It is a reasonable approximation of actual physical and chemical processes occurring in lithography, therefore it can be extrapolated to predict new processes or new patterns not covered by the calibration process of the model.
- 2) It has relatively a small number of key parameters which can be extracted efficiently by sampling experimental data. In another word, the model can be easily trained.
- 3) Its computational complexity is small.
- 4) As far as lithography engineering is concerned, the capability of predicting through-dose, through-focus and across-tool behaviors of various patterns within reasonable error is highly desired.

Developing such a model is the main theme of this thesis. A systematic divide-and-conquer strategy is presented and the modeling methodology is developed in this chapter. In summer 2000 and summer 2001, the author had the opportunity to work at KFAB of Texas Instruments (TI). The experimental and simulation work on characterizing 193nm lithography at TI provides a solid basis for this chapter. The discussion with Maureen Hanratty, Keeho Kim, Mark Terry and Mark Ma, the author's mentors and colleagues at TI, greatly helps motivate and develop the modeling work presented in this chapter. Their

advice and knowledge offered generously to the author is highly appreciated. Meanwhile, the author appreciates Jeff Byers at International SEMATECH (now he is with FINLE, a subsidiary of KLA-Tencor) for providing resist and anti-reflective coating (ARC) parameters. The resist parameters were measured at SEMATECH and now are available through resist vendor.

Based on the enormous amount of experimental data and SEM pictures obtained at TI, a divide-and-conquer strategy was used to identify the main process factors individually. The main factors affecting printing quality include mask accuracy, choice of imaging imaging focal plane, lens aberrations, resist PEB process and resist dissolution mechanism. Practically, the SEM measurement error is also not negligible in calibrating models. In particular, the large LER and resist slimming of 193nm resists make the measurements much more noisy than for 248nm resists.

First, the actual mask CDs were measured and used in all simulations, which excludes the mask error effect. Comparing the mask CDs and wafer CDs, it is found that the unexpected isolated-dense line bias is mostly determined by mask CD variations and Mask Error Factor (MEF). Then by inspecting the CD vs. defocus curves of isolated and dense lines, the location of focal plane in the resist was determined. When adding lens aberrations measured by Litel in-situ technique at TI and simulating CD vs. defocus curves of lines, it was found that the actual focal plane location was 0.1 μ m lower than calculated under the assumption of aberration-free lens. The error of simulated CDs is reduced by 15% after including lens aberrations. It proves the importance of incorporating lens aberrations in the model and furthermore indicates that positioning the focal plane can compensate for lens imperfection to some extent.

Using the measured mask CDs, lens aberrations and the imaging location found above, the light intensity in resist of lines at different defocus, different pitch and $9.5\text{mJ}/\text{cm}^2$ dose are simulated. A threshold light intensity model was used to determine the line CDs. By fitting line CD vs. defocus simulations with experimental curves, the threshold was extracted. The Root Mean Square (RMS) value of the simulation error was 5.26nm , or 5% of the smallest linewidth. Thus this single-threshold model is adequate in predicting line CDs through focus.

The calibrated single-threshold resist imaging model was further used to simulate 2-dimensional patterns. The simulated images conform the experimental SEM pictures very well and the mismatched area is generally less than 15% of the pattern area. However, this line-end gaps predicted by this model were much larger than experimental. The RMS error is 43nm , which indicates the resist PEB or dissolution process may have big impact on opening gaps. Two models were tested to identify the impact of the two resist processes separately. One was PEB model in which the acid diffusivity, the deprotection rate constant and the threshold activated site concentration were tuned to determine the line-end gaps. The PEB model reduced RMS error of line-end gap prediction to 37nm with little change in RMS error of predicting linewidths. The other model tested was a dissolution model in which the dissolvability of resist at a certain location is enhanced by the maximum acid concentration in its neighborhood. While keeping the error of linewidth simulation within 6nm , the dissolution model reduces the error of predicting gaps to 26nm over different doses and focuses. Finally the PEB model and dissolution model were combined to predict the patterns CDs through dose/focus with RMS error of 26nm . The residual error may be due to the incompleteness of dissolution simulation.

5.2 Experimental Setup

The experiments were done at Texas Instruments on a 193nm 4X scanner, NA 0.6, σ 0.75. The scanner is an early engineering tool. The Sumitomo PAR710 resist was used, a soft bake 130°C, 60sec, and post exposure bake 130°C, 60sec. After soft bake, the resist thickness is 350nm. Along with the resist, the Bottom Anti-Reflective Coating (BARC) AZ-20 was also used with thickness 82nm.

A full through dose and through defocus matrix was exposed. The dose used was from 9 to 10.5mJ/cm² in step of 0.5mJ/cm². The defocus was from -0.2 to 0.2 μ m in steps of 0.1 μ m. After development, the SEM pictures of the patterns were taken. All SEM pictures had the same magnification of 150K. The resist parameters were provided by International SEMATECH. The optical constants of the PAR710 resist are $n=1.699$, $A=0$, $B=1.114$, $C=0.05\text{mJ}^{-1}$. The BARC AZ-20 has refractive index $n=1.706174$, $k=0.40784$.

Before the exposure experiments, the mask was measured. In all the simulations in this chapter, the measured mask CDs were used. In particular, 1D line/space patterns and two 2D patterns named 'D11H' and 'D18H' were used to develop and test the models. The measured linewidths on the mask are listed in Table 5-1 and the two 2D patterns with measured CDs are shown in Figure 5-1 and 5-2, respectively.

Table 5-1 Measured CDs on the mask

Note that the mask is 4X, thus the resulted wafer CDs are supposed to be ¼ the mask CD.

		0.4	0.48	0.52	0.56	Designed Mask CD (um)
Pitch	1.28	0.428	0.532	0.575	0.644	
(µm)	1.32	0.431	0.526	0.56	0.594	
	1.36	0.409	0.514	0.546	0.571	
	1.4	0.438	0.513	0.544	0.569	
	1.5	0.425	0.504	0.538	0.577	
	1.6	0.422	0.507	0.539	0.565	
	1.8	0.426	0.504	0.541	0.582	
	2	0.431	0.514	0.542	0.585	
	2.4	0.436	0.513	0.548	0.591	
	3	0.429	0.503	0.54	0.583	
	4	0.431	0.494	0.533	0.587	
	5	0.425	0.498	0.525	0.569	
	6	0.412	0.5	0.52	0.564	
	7	0.409	0.477	0.516	0.567	
	isolated	0.414	0.469	0.514	0.567	

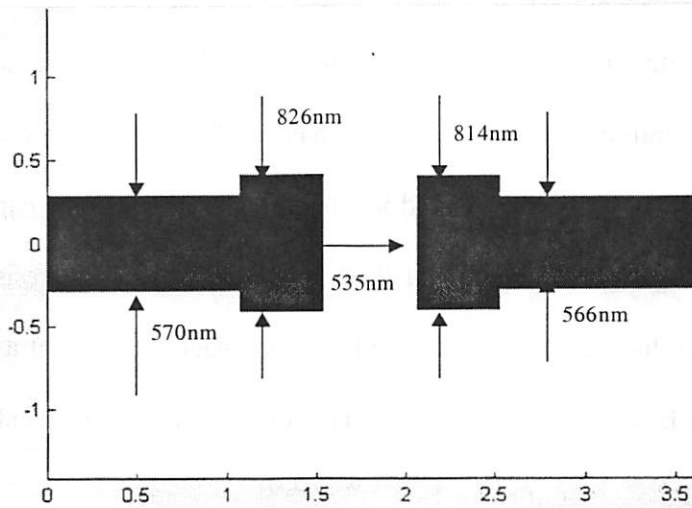


Figure 5-1 D11H, the mask pattern used for calibrating simulation models

All the dimensions noted in the figure were from actual mask measurements. The axis are in unit μm . Note that the mask is 4X

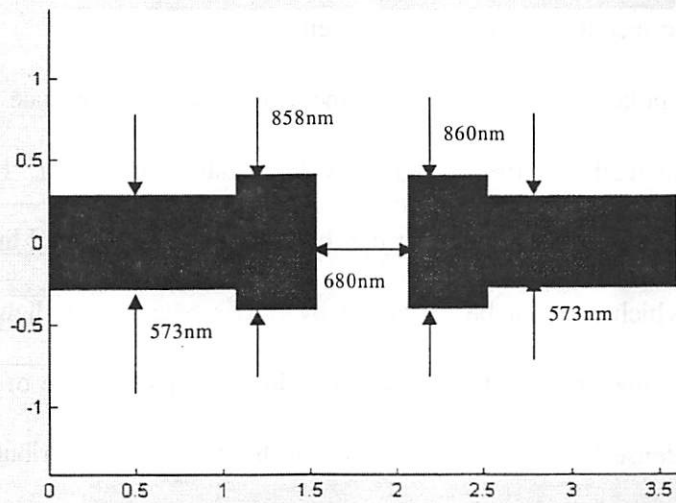


Figure 5-2 D18H, the mask pattern used for verification of simulation models

All the dimensions noted in the figure were from actual mask measurements. The axis are in unit μm . Note that the mask is 4X.

5.3 Simulation Setup

[57][58][59] etc. show that the Aerial Image Model, even including aberrations, is not sufficient to capture the through-focus behavior of lines. On the other hand, the imaging in resist model which was presented in Chapter 1 is shown to be capable of capturing the essential through-focus variation of lines. Thus the imaging in resist model is used as a base model in this chapter. It first simulates the image intensity at a location within resist and then uses Equation 5-1 to convert image intensity to acid concentration:

Equation 5-1 $C_a(x,y) = 1 - e^{-C \cdot Dose \cdot I(x,y)}$

Where $I(x,y)$ is the normalized image in resist, and $Dose$ is the exposure dose in mJ/cm^2 , C is the Dill's C parameter in cm^2/mJ . The conversion of image to acid is for simulating the effects of different doses. Finally a threshold detector is used to determine the simulated CD, which means the resist will be developed where the image intensity or activated site concentration is above a given threshold.

Before the simulation, it is worthy of mentioning the importance of plus the measured mask CDs instead of the designed values into simulation. Figure 5-3 plots the experimental linewidths vs. pitch. It can be seen that the isolated lines are wider than the dense lines, which can not be explained by optics because the light intensity on isolated lines is always higher than dense lines. The light intensity slope of isolated lines are also steeper than dense lines. Figure 5-4 plots the light intensity distribution across the 130nm line at pitch from 320nm to 1750nm. Furthermore, isolated resist lines are attacked by more acid or developer than dense lines are, due to the fact that isolated resist lines are facing much broader spaces which have higher acid or developer concentration. Thus it is expected that isolated lines are narrower than dense lines. In fact, it can be explained by

mask CD variation. Figure 5-5 plots the measured mask CDs vs. pitch. The mask CDs and pitches have been divided by 4 for normalization to 1X. Compared Figure 5-3 and 5-5, it can be seen that the wafer CDs almost exactly follow the variation of mask CDs. When the pitches are less than 400nm, the mask CD errors are magnified by the Mask Error Factor (MEF) that can be up to 2 for lines if pitch is small. Therefore the isolated-dense bias is mostly due to the mask CD variation, or in other words, due to the isolated-dense bias of mask CD. Note that the mask CD variation is consistent with pitch variation. Thus current OPC models, calibrated on through-pitch and through-width line CDs, are actually including the mask making bias effects. This also helps explain why the current OPC models are only valid for a particular mask making tool[60][61].

5.4 Identifying Imaging Location in Resist

In gate printing process, linewidth control is the first priority. Thus the effectiveness of a lithography model should be tested first against the through dose, through defocus and through pitch behavior of linewidths. Moreover, the linewidths are basically 1-dimensional structures and therefore provide ground for building models.

A plot of linewidths of 100-140nm lines at pitch 350nm, exposure dose $9.5\text{mJ}/\text{cm}^2$, and at defocus -0.2 to $0.2\ \mu\text{m}$ is shown in Figure 5-6.

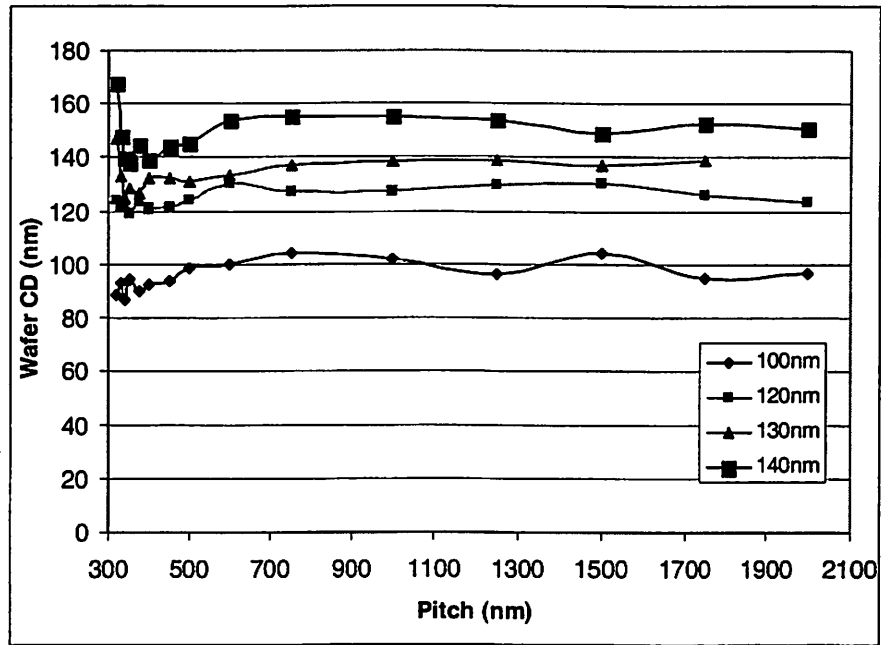


Figure 5-3 Wafer CD vs. pitch

The wafer CDs are exposed at 0 defocus, 9.5mJ/cm² dose.

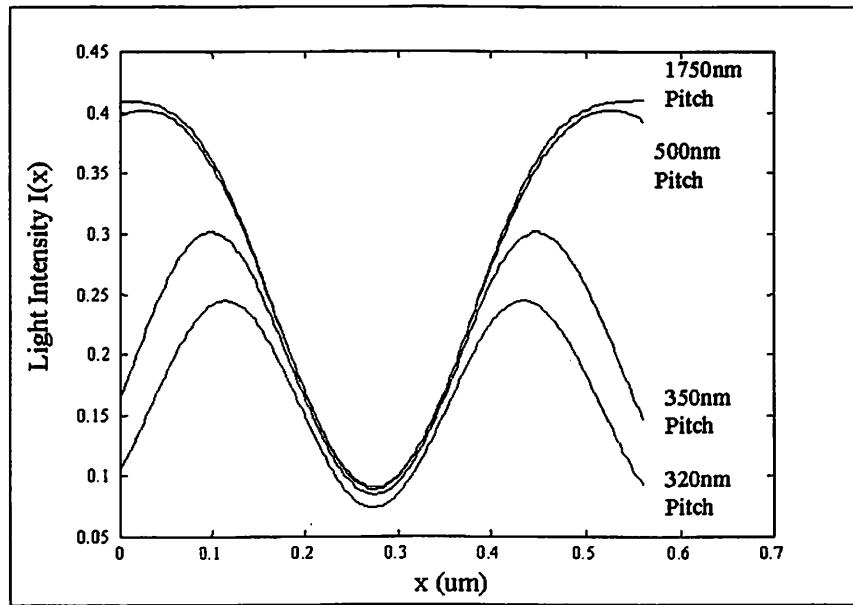


Figure 5-4 Simulated light intensity of 130nm line in resist

The light intensities are taken at the bottom of resist. Defocus 0um.

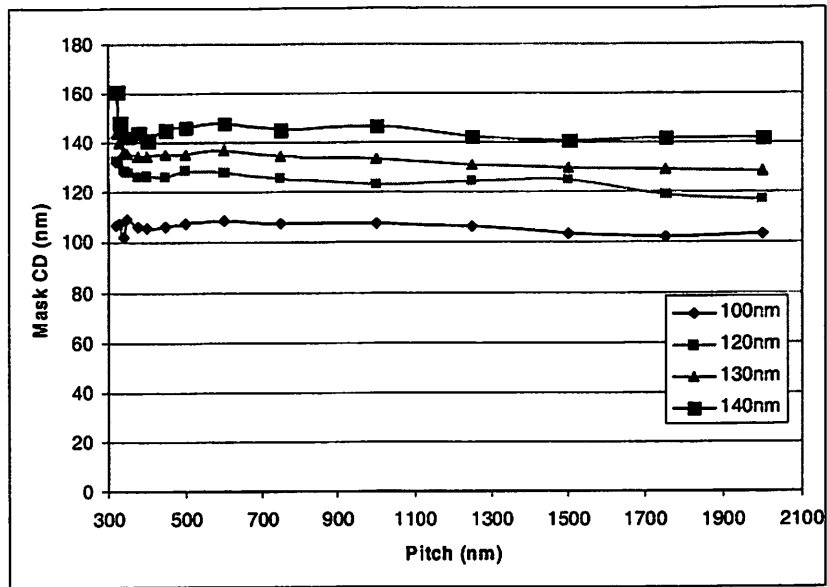


Figure 5-5 Mask CD vs. pitch

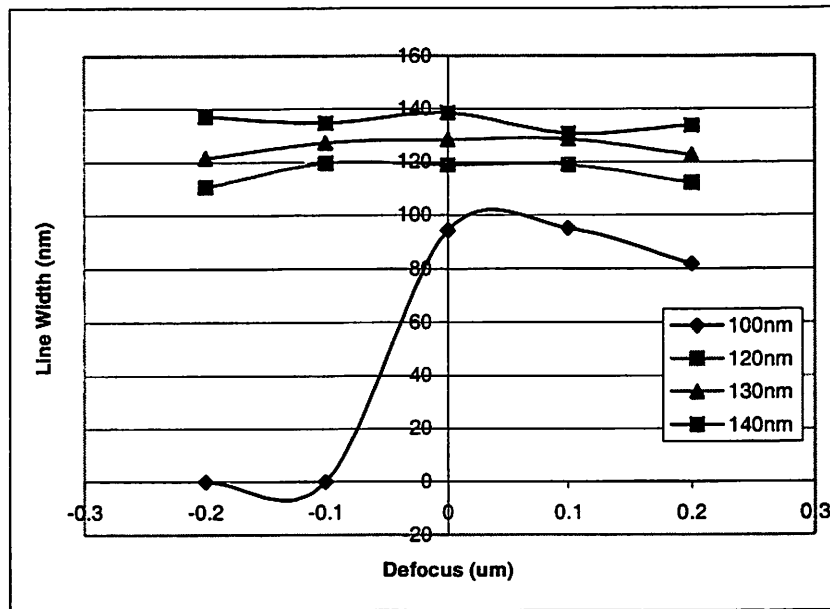


Figure 5-6 Linewidths vs. defocus at 350nm pitch

Note that the wafer CDs of the 100nm line at -200 and -100nm defocus are 0, which means there were no patterns on the wafer.

Note that there were no patterns of the 100nm line on the wafer when the defocus was -200nm or -100nm . This could be due to processing latitude problem.

From Figure 5-6, it can be seen that the best focus corresponds to a positive defocus setup on the scanner which is very close to 0. Since the line CDs are determined by the feet of the remaining resist or the image intensity at the bottom of resist, the focal plane of the scanner is most likely close to the bottom of the resist. The resist thickness, however, also affects the image intensity distribution at the bottom of resist. Figure 5-7 plots the light intensity at the bottom of resist when the 0 defocus corresponds to a focal plane $0.2\mu\text{m}$ below the resist surface.

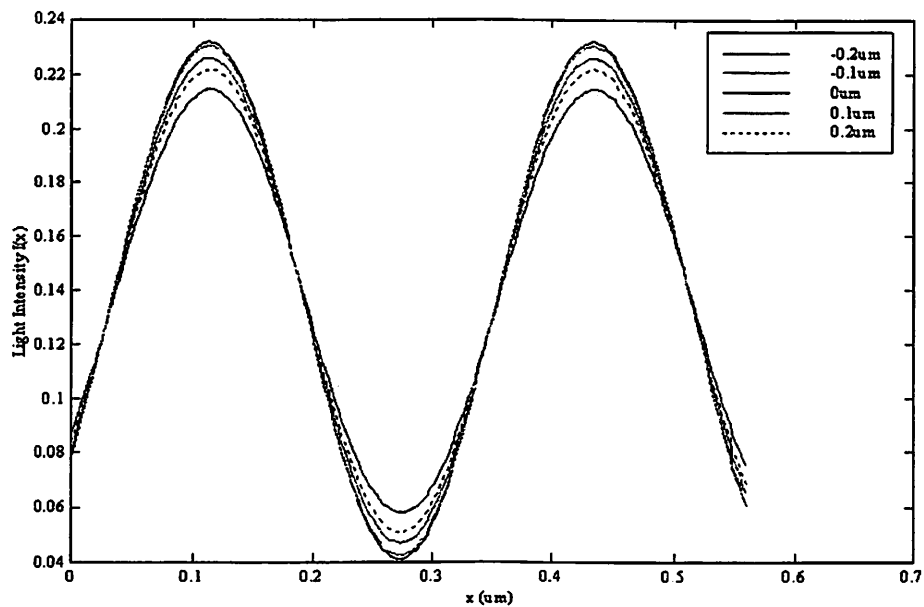


Figure 5-7 Light intensity of 140nm line at 350nm pitch

The light intensities are taken at the bottom of resist. The 0 defocus means the focal plane is $0.2\mu\text{m}$ below the resist surface.

By introducing resist thickness effect and focal plane location, the light intensity is no longer symmetric with defocus. Thus it explains the asymmetric behavior of line CDs with defocus varying, while aerial image model can not explain that.

The following procedure was used to determine the actual position of the focal plane. First use SPLAT to simulate the image intensity at the bottom of resist through defocus, at dose $9.5\text{mJ}/\text{cm}^2$, assuming the distance of focal plane to the resist surface is Z , where positive Z means the focal plane is below the resist surface (away from the lens) and negative Z means the focal plane is above the resist surface (towards the lens). In the simulation, the measured mask CDs of the 100, 120, 130 and 140nm lines were used to exclude the mask error effects. After obtaining the image intensities, a threshold detector is used to calculate the linewidths, which assumes the resist at which the image intensity is above a given threshold is developed. The Root Mean Square (RMS) value of the errors between simulation and experimental data is calculated over the 4 lines and 5 defocuses. The disappearance of 100nm lines at negative defocuses could be due to process errors, thus the simulations at these nodes were not included in the calculation of RMS error. Figure 5-8 shows the simulated linewidths vs. defocus when the focal plane is 0.35, 0.25, 0.2 and 0.15 μm below resist surface, assuming the lens is aberration-free. The corresponding RMS errors are 17.16, 6.77, 3.29 and 4.05 nm, respectively.

From Figure 5-8, it can be seen that the 0.35 μm and 0.25 μm focal positions make the best focus at $-0.2\ \mu\text{m}$ and $-0.1\ \mu\text{m}$, respectively, whereas the best focus determined by the experiments is around $0\ \mu\text{m}$. Furthermore, their RMS errors are large. This indicates these two focal positions fail in capturing the through-focus trend of the line CDs. On the other hand, the 0.20 μm focal position shows almost identical through-focus trend as the

experimental curves and has minimum RMS error 3.29nm. The 0.15 μm focal position shifts the best focus further to +0.05 μm , which excludes the possibility of this position being the 0 defocus setup on the scanner. This concludes that the 0 defocus setup on the scanner is approximately 0.20 μm below the resist surface, which is explained as follows.

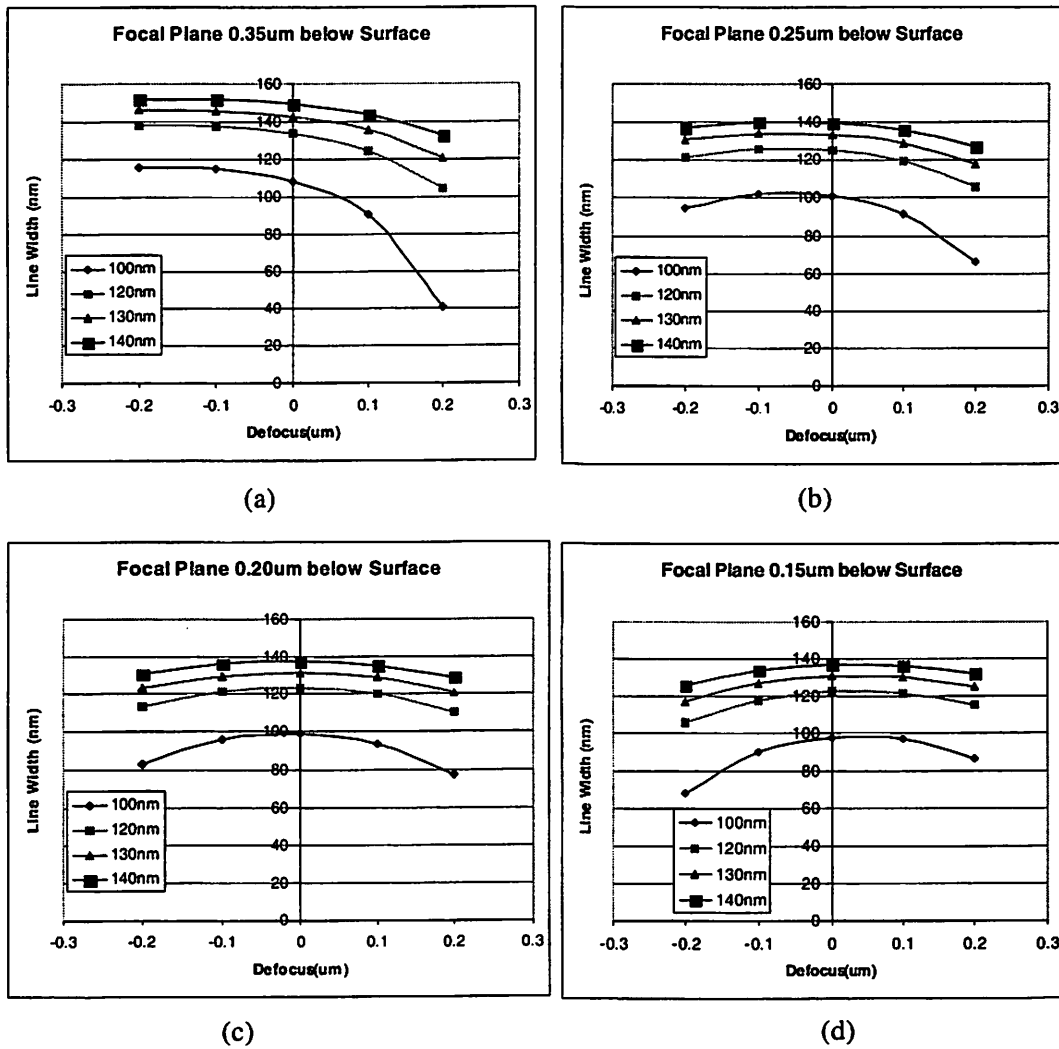


Figure 5-8 Simulated linewidths vs. defocus at 350nm pitch

Four lines shown in the plot are 100, 120, 130 and 140nm wide, respectively. From (a) to (d) the focal plane are 0.35, 0.25, 0.20 and 0.15 μm below the resist surface, respectively.

Consider an exposure system with 1X lens (the actual lens in the scanner is 4X, but the imaging parameters in experiments and simulations are all adjusted to 1X) depicted in Figure 5-9 (a).

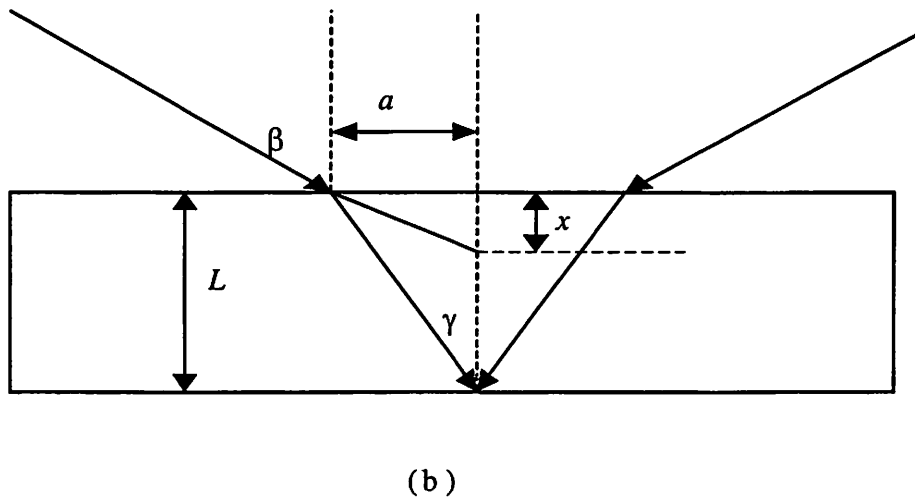
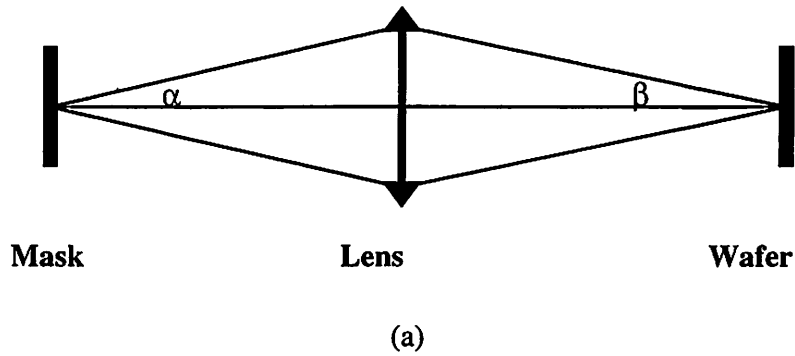


Figure 5-9 Diagram of a 1X exposure/resist system.

In (a), the components of the scanner are shown. Note that the lens is 1X, thus $\alpha = \beta = \sin^{-1}NA$. The resist system is depicted in (b), where L is the resist thickness. The incident angle is β and the refraction angle is γ .

Obviously, the angles α and β are given by

Equation 5-2 $\sin \alpha = \sin \beta = NA$

The refraction angle is given by Snell's Law

Equation 5-3 $\sin \beta = n \sin \gamma$

Where n is the refractive index of resist.

If there were no resist, the two rays at the edge of lens will converge at the focus. Due to resist refraction, however, the two rays will converge at another point below the original focus. Suppose the resist thickness is L , and the distance of the original focus to the resist surface is x . Since the bottom of the remaining resist after develop determines the resist CD, it is desired to converge the rays emitted from a certain point to the bottom of resist so as to reduce the imaging spread at the bottom. Therefore the desired imaging spread at the resist surface is given by

Equation 5-4 $a = L \cdot \tan \gamma$

Therefore the original focus is positioned at

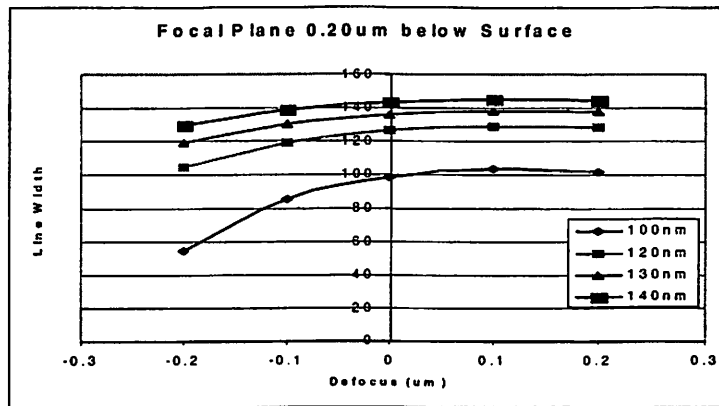
Equation 5-5 $x = \frac{a}{\tan \beta}$

In the experiments, the resist thickness $L=350\text{nm}$, refractive index $n=1.699$. Using Equations 5-2 to 5-5, it is found that $x=176\text{nm}$. That is, the optimum focal plane is estimated to be 176nm below the resist surface, which justifies our conclusion that the 0 defocus setup on the scanner corresponds to the plane 0.20 μm below resist surface if the lens is aberration free.

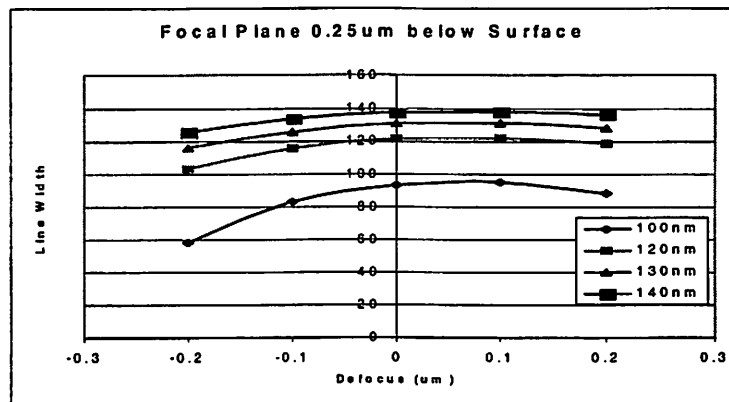
5.5 Simulating Linewidths in the Presence of Lens Aberrations

The best imaging location found in Section 5.4 is not valid when taking into account the fact that the lens is not perfect. The aberrations were measured through Litel in-situ technology and the Strehl ratio was found to be 0.926. Although this Strehl ratio does not have significant impact on aerial image, it significantly affect the imaging in resist. Figure 5-10 shows the linewidths vs. defocus when the focal plane is 0.20, 0.25 and 0.30 μm below resist surface, simulated with the measured lens aberrations. The corresponding RMS errors are 9.94, 4.99 and 2.79 nm, respectively. It can be seen that the conclusion that the optimum focal plane is 0.2 μm below resist surface is not longer valid if the lens aberrations are taken into account. In fact, the best focal plane is now 0.30 μm below the resist surface. By including lens aberrations, the best focal plane is shifted 0.1 μm towards the resist bottom and the RMS error is reduced from 3.29nm to 2.79nm, or 15%. Thus lens aberrations are critical to the choice of best focus and to the through-focus variation of CDs.

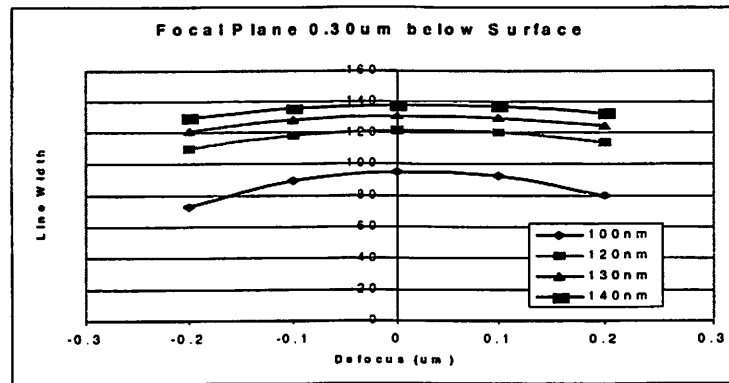
Setting the best focus to be 0.30 μm below resist surface and including lens aberrations into SPLAT simulations, the line CDs can be calculated with the threshold found above. Figure 5-11 compares the experimental and simulated CDs vs. defocus at 350nm and 1750nm pitch, exposure dose 9.5mJ/cm². The RMS error for the four different lines at 5 defocuses and 4 different pitches (320, 350, 500 and 1750nm) is 5.28 nm. That is, the RMS error over 80 line CD measurements is 5.28 nm, or 5.3% of the smallest linewidth (100nm mask CD).



(a)



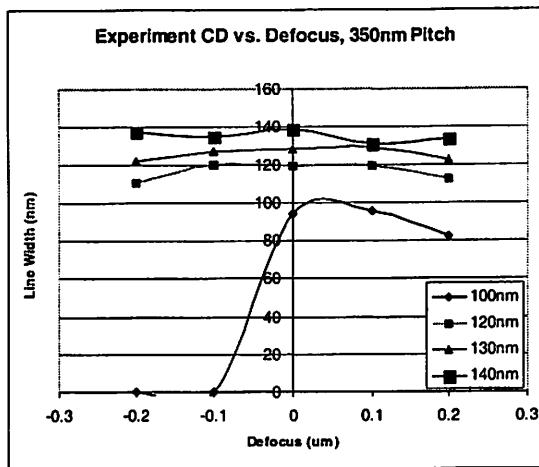
(b)



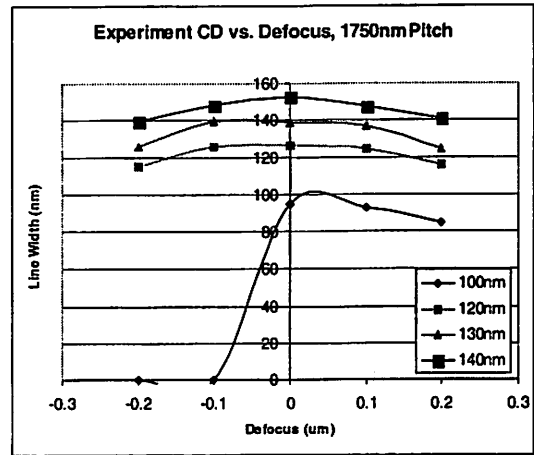
(c)

Figure 5-10 Simulated linewidth vs. defocus at 350nm pitch, aberrations included

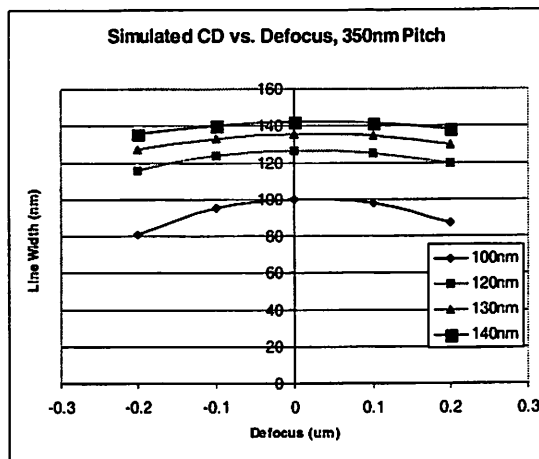
Four lines shown in the plot are 100, 120, 130 and 140nm wide, respectively. From (a) to (d) the focal plane are 0.20, 0.25 and 0.30 μ m below the resist surface, respectively.



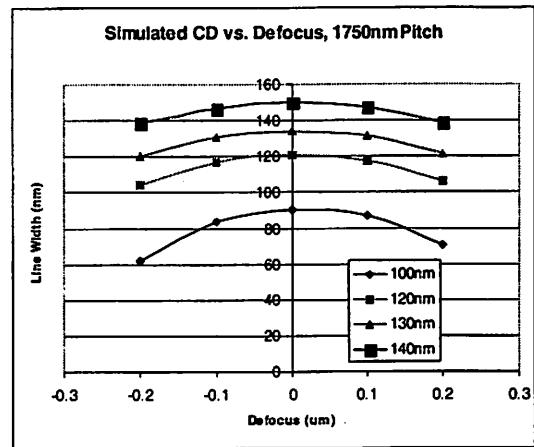
(a)



(b)



(c)



(d)

Figure 5-11 Experimental and simulated linewidth vs. defocus at 350nm and 1750nm pitch, lens aberrations included

Four lines shown in the plot are 100, 120, 130 and 140nm wide, respectively. Here (a) and (b) are experimental CDs at 350 and 1750nm pitch, respectively. (c) and (d) are corresponding simulated CDs.

Generally, the CD control in gate printing process requires $\pm 5\%$ CD variation. And SEM measurement error is more than 10nm due to resist slimming and line-edge

roughness[15]. Thus this simple resist imaging model, aided by lens aberrations, is capable of predicting line CD with RMS error 5% of the current 130nm node. It is sufficient for mask layout verification or process validation to ensure proper CD control.

Combining the above analysis, it is concluded that the variation of linewidths are mostly due to mask CD bias. The lens aberrations are critical to the choice of optimum focal plane and are essential to predicting the through-focus CD variation. Due to the sharp image slope in line/space structures, the line CDs are not sensitive to PEB or dissolution process. By calculating the image intensity on the bottom of resist with the measured Zernike polynomial coefficients, the linewidths can be predicted with RMS error 5.28nm, which is even less than the SEM measurement error.

On the other hand, PEB and dissolution models are not negligible in predicting pattern fidelity of 2-dimensional features, as will be shown in next section.

5.6 Analysis of Experimental and Simulated Images

With the defocus setup and the threshold obtained in Section 5.4, D11H, the pattern shown in Figure 5-1 was simulated with dose 9.0, 9.5, 10.0 and 10.5 mJ/cm², defocus – 0.2 to 0.2μm. Note that the same relative light intensity at different dose generates different photoacid concentration. Thus the threshold light intensity is converted to threshold photoacid concentration by Equation 5-1. Then the simulated images were compared with the monochromatic representations of the corresponding experimental SEM pictures and the Image Mismatching Factor (IMF) was calculated to evaluate the effectiveness of the resist imaging model. The mask pattern shown in Figure 5-1, ‘D11H’, was first simulated to evaluate the predictability of the simulation model. Note

that there was noticeable amount of bias on mask. The designed separation between the two line ends is 120nm, while the actual space on mask is equivalent to 134nm.

The SEM pictures of the corresponding wafer pattern exposed at $9.5\text{mJ}/\text{cm}^2$ and defocus -0.2 to $0.2\mu\text{m}$ are shown in Figure 5-12. The corresponding monochromatic representations of these SEM pictures are shown in Figure 5-13.

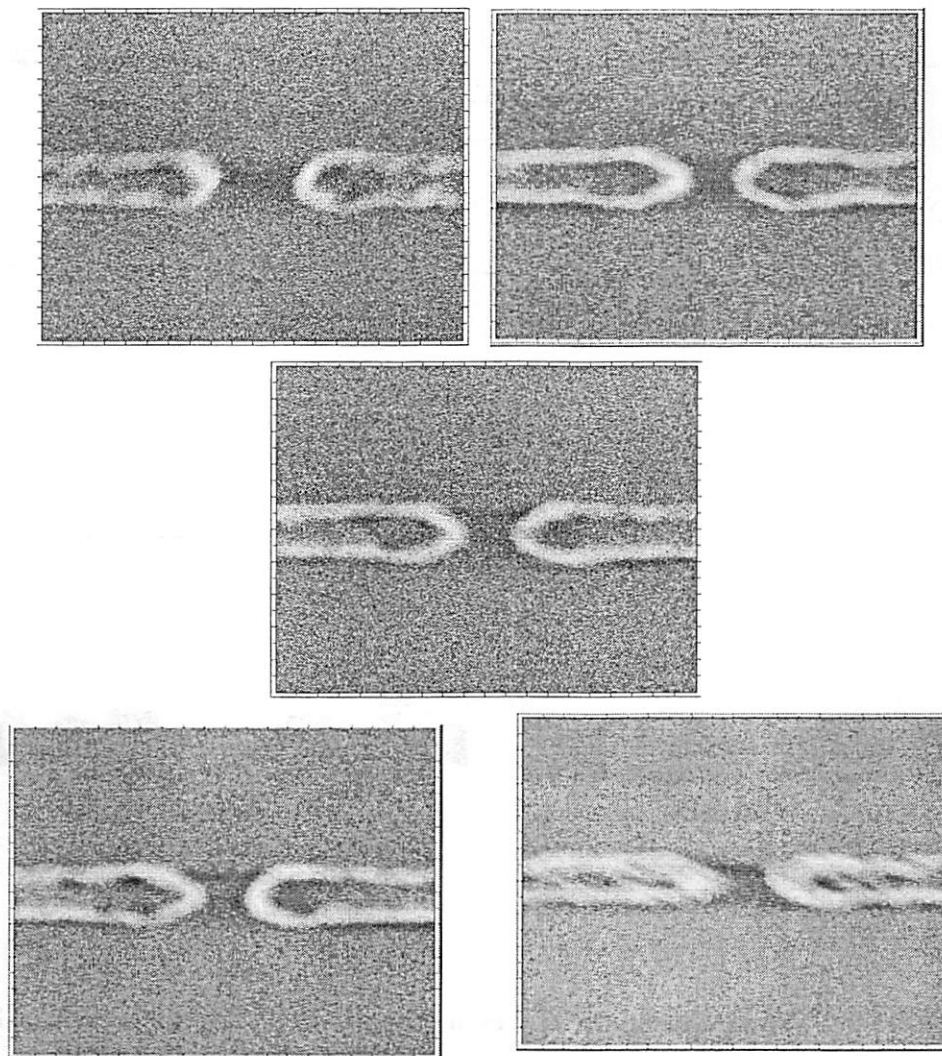


Figure 5-12 SEM pictures of D11H exposed at $9.5\text{mJ}/\text{cm}^2$.

From left to right and from top to bottom, the pictures correspond to defocus -0.2 , -0.1 , 0 , 0.1 and $0.2\mu\text{m}$.

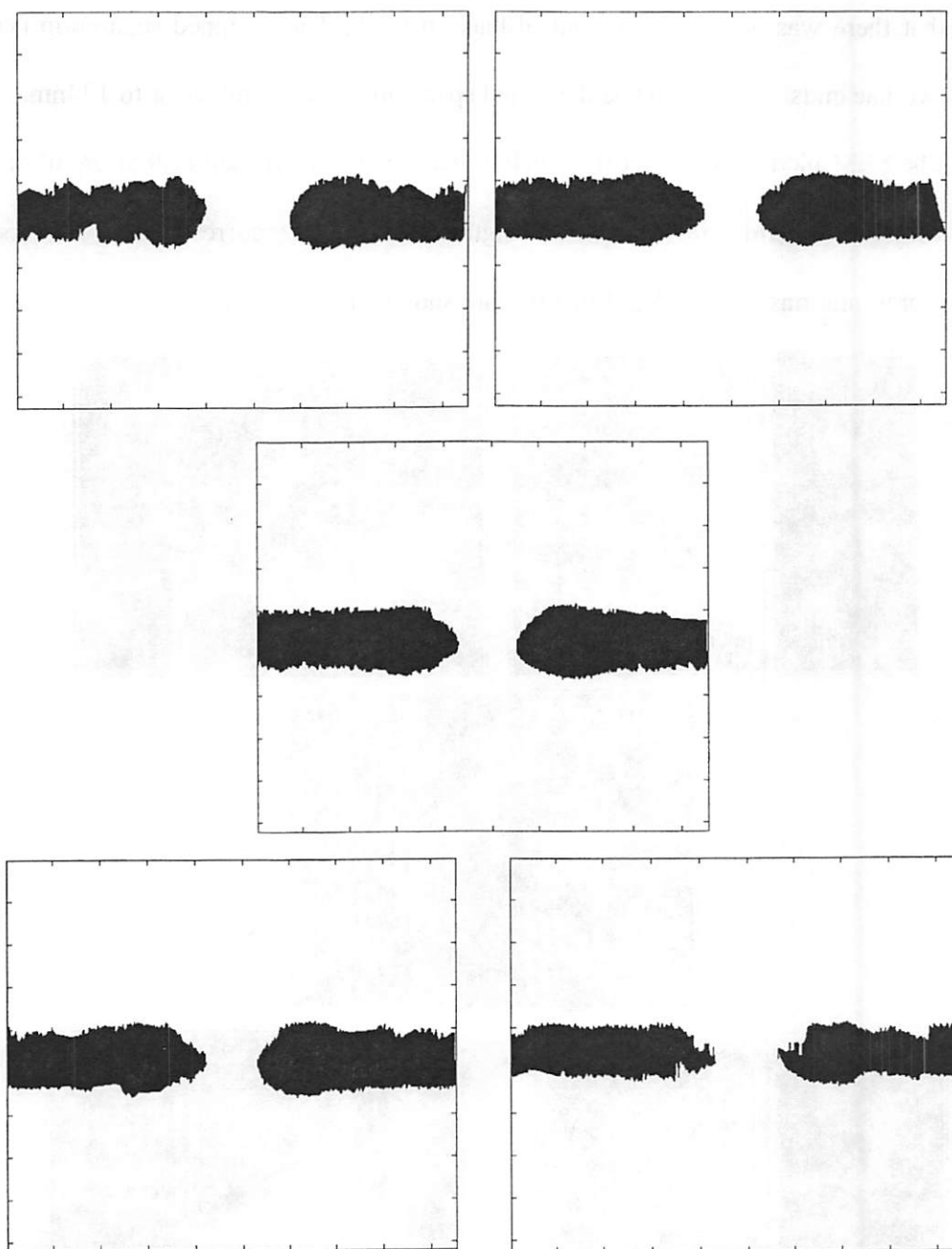


Figure 5-13 The monochromatic representations of the SEM pictures of D11H
exposed at $9.5\text{mJ}/\text{cm}^2$.

From left to right and from top to bottom, the pictures correspond to defocus -0.2 , -0.1 , 0 , 0.1 and $0.2\mu\text{m}$.

For the purpose of CD control, a good model is expected to predict line or space CDs on arbitrary patterns within reasonable error. For the patterns D11H and D18H, the CD used to evaluate a model is the spacing between the two line ends. Figure 5-14 plots the through-dose, through-focus spacing of D11H. Since the resist shrink during SEM measurements, the curves are smoothed in Figure 5-15. In the smoothing process, it is assumed that the space CD is a parabolic function of defocus at a certain dose. That is

Equation 5-6 $CD(x) = a + bx + cx^2$

Where x is the defocus, a , b and c are functions of dose. By fitting the CDs at a dose with Equation 5-6, the coefficients a , b and c can be determined and the smoothed CDs are given by Equation 5-6. The smoothed curves are shown in Figure 5-15.

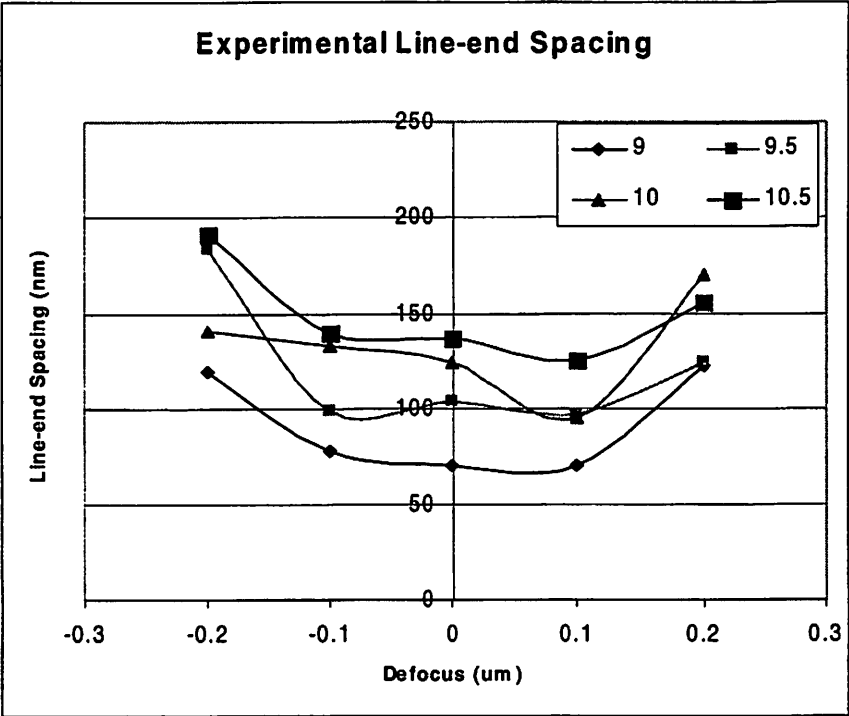


Figure 5-14 The experimental line-end spacing of D11H

The legend refers to dose.

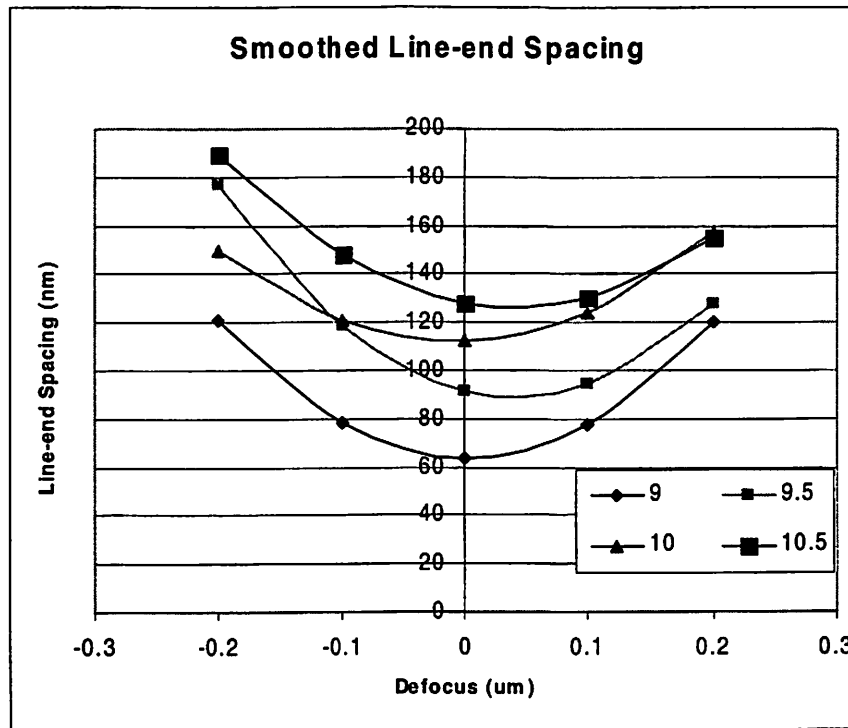


Figure 5-15 The smoothed line-end spacing of D11H

The legend refers to dose.

The overlay of the simulated images with the monochromatic representations of experimental pictures is shown in Figure 5-16. The simulations agree with experimental images in black areas in Figure 5-16, and do not agree in gray areas. In Figure 5-16, (a) to (d) correspond to exposure dose 9.0, 9.5, 10.0 and 10.5 mJ/cm², respectively. Only the overlay of simulations at 0 defocus are shown. The model it was further used to test another pattern D18H at dose 9.0 to 10.5 mJ/cm², and -0.2 to 0.2μm defocus. The average IMFs were used to evaluate the models' predictability.

The IMFs of D11H and D18H at dose 9.0 to 10.5mJ/cm² and defocus -0.2 to 0.2 μm are listed in Table 5-2. Figure 5-17 plots the corresponding spacing predicted by the resist imaging model.

Table 5-2 IMFs of the simulations applied to two patterns

The IMFs at defocus -0.2μm to 0.2μm, at dose 9 to 10.5 mJ/cm², are shown.

IMF of D11H		9	9.5	10	10.5	Dose
Defocus	-0.2	0.133	0.1401	0.1317	0.156	
	-0.1	0.1082	0.114	0.1407	0.0992	
	0	0.1439	0.0915	0.137	0.131	
	0.1	0.126	0.1422	0.1318	0.1342	
	0.2	0.2508	0.1706	0.5477	0.1195	
	Average	0.15238	0.13168	0.21778	0.12798	

IMF of D18H		9	9.5	10	10.5	Dose
Defocus	-0.2	0.094	0.2117	0.0855	0.1323	
	-0.1	0.092	0.0946	0.0759	0.0873	
	0	0.0635	0.1279	0.0914	0.0879	
	0.1	0.0708	0.0584	0.0862	0.0922	
	0.2	0.3265	0.2399	0.3762	0.2079	
	Average	0.12936	0.1465	0.14304	0.12152	

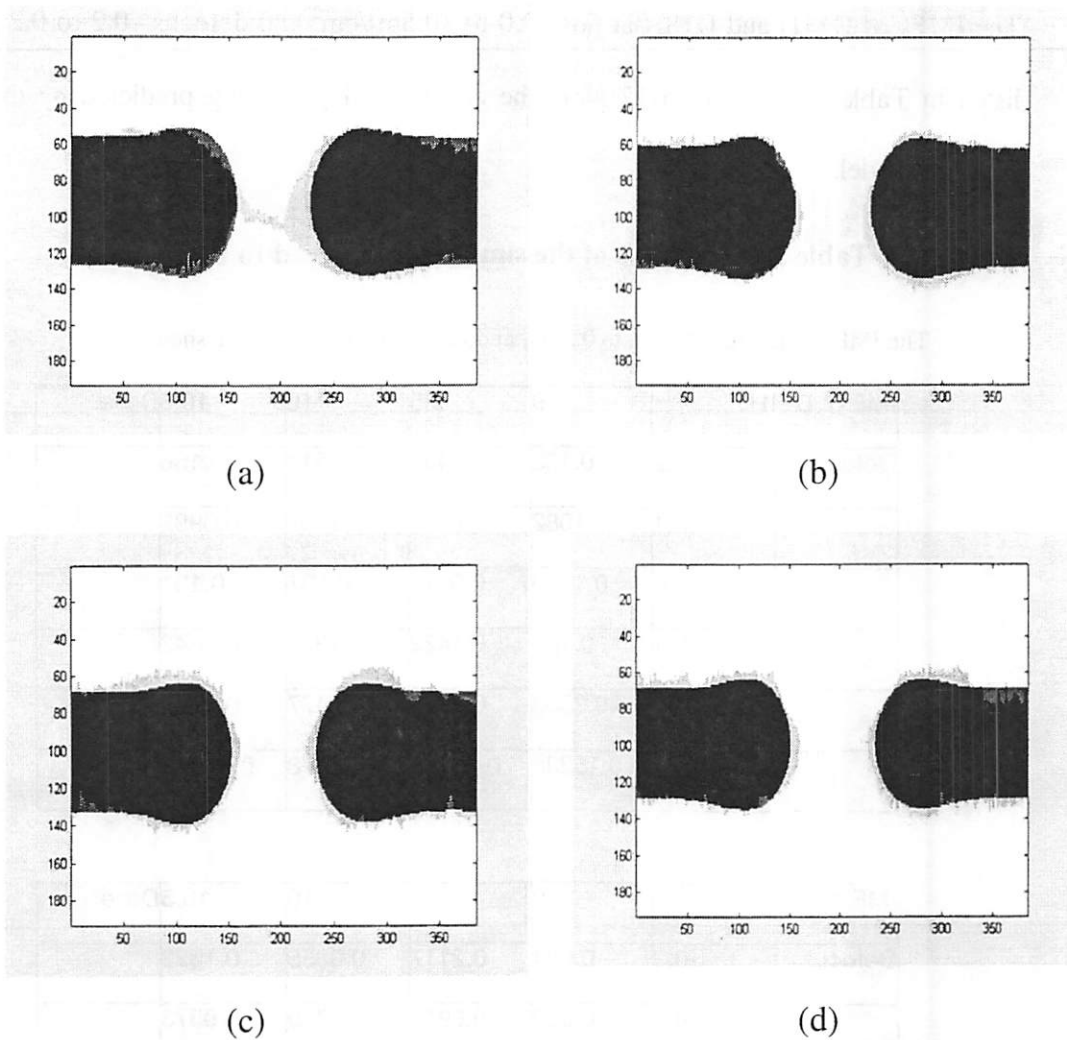


Figure 5-16 Overlay of simulated and experimental images.

The simulations overlap with experiments in the black area, while they do not agree in the gray area.

Table 5-2 and Figure 5-16 show that this resist imaging model fits through-dose, through-focus experimental SEM pictures very well, even though the threshold photoacid concentration was obtained by fitting linewidths at $9.5\text{mJ}/\text{cm}^2$ dose only. At the $0.2\mu\text{m}$

defocus, however, the IMFs are much larger than at other defocuses. This is mostly due to the blurriness of SEM pictures corresponding to the 0.2 μ m defocus patterns. Not yet well developed, the 193nm resists are facing the problems such as large line edge roughness (LER), low contrast and resist slimming during SEM measurements. At 0.2 μ m defocus, the imaging quality of the patterns was poor, thus the resist had much more severe LER compared with other defocuses, as can be seen in Figure 5-12 and 5-13. This made the extraction of monochromatic images from the SEM pictures very noisy. This mismatch can be probably solved by adjusting SEM pictures to remove the textures caused by LER, a topic beyond the scope of this thesis.

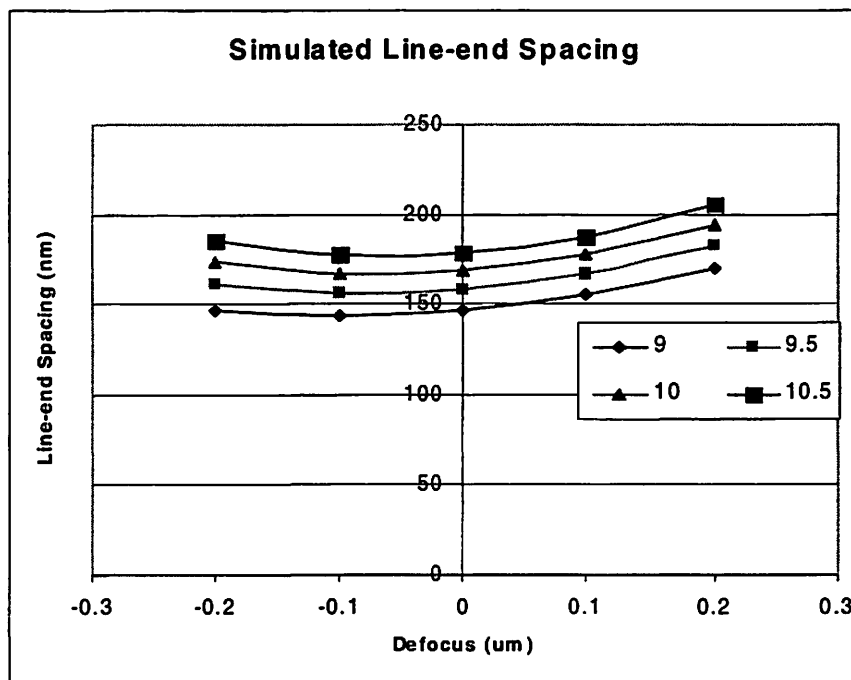


Figure 5-17 The simulated line-end spacing of D11H

The legend refers to dose.

However, the spacing predicted by this resist imaging model is significantly and consistently larger than the experimental data. The RMS error of prediction is 43.6nm, which indicates the chemical effects other than optical effects must be taken into account. It is well known that line-end shortening (LES) frequently occurs in 248nm lithography, which means the spacing between two line ends is larger than designed. In 193nm lithography, however, line-end spacing is often smaller than design and causes scum and bridging effects. There could be two mechanisms contributing to this line-end gap shrinkage phenomenon. First is the PEB process. Along the edge of lines the image intensity is high (almost 1) and the image slope is steep. In the neighborhood of line-end gap, however, the image intensity is low (typically less than 0.7). Thus it is expected that larger amount of acid can diffuse into the line than diffuse into gap. The other mechanism is the dissolution process. The neighborhood of lines has very high dissolution rate and thus is dissolved instantly at the beginning of developing. Then the sidewalls of lines are attacked by developer, which effectively increases the dissolution of lines. In contrast, the neighbor of line-ends is dark and the dissolution rate is relatively low. Thus it takes more time to open the gap and therefore leaves less time for the developer to attack resist line ends. As a consequence, the gap is developed for less time and may show more roughness and scum than line edges do.

The reason that the resist imaging model succeeds in predicting linewidths but fails in predicting line-end gap is further explored by Figure 5-18.

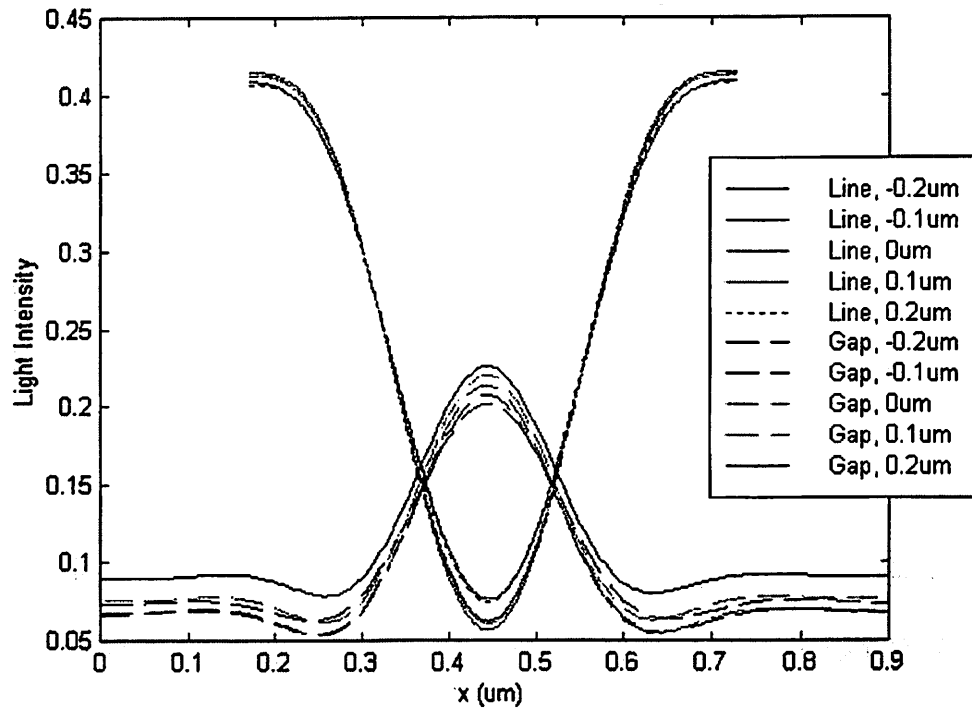


Figure 5-18 Light intensity across lines and line-end gaps

The line is 140nm wide, isolated. The gap is 134nm on mask. Both features were exposed at 9.5mJ/cm². The legends refer to defocus.

Figure 5-18 shows that the lines have much and steeper higher peak light intensity than the gaps, which justifies the above argument that gaps are developed for less time and the advancing of developer is relatively slow. Also, note that the lens aberration have bigger impact on gaps than on lines. The light intensity of gaps is not symmetric or sharp whereas that of lines is almost as symmetric and sharp as without aberrations.

To determine the impact of PEB and dissolution on printing the line-end gap, two models corresponding to the two processes are presented in next sections.

5.7 Analysis of PEB Models

The PEB model presented in chapter 2 and 3 was used to predict the pattern CDs. The PEB reaction rate constant $K_1=0.307s^{-1}$, acid loss rate constant $K_2=0s^{-1}$, diffusivity constant $D_0=20.65nm^2/s$, exponential diffusivity constant $\omega=3$, reaction order $m=1$. After PEB simulation through RIAR, a threshold model was used to determine the CDs. The deprotection/diffusion parameters were provided by International SEMATECH. However, the reaction rate constant K_1 , diffusivity D_0 and exponential diffusion factor ω were found to be so large as to clear all resist. Thus the parameters were tuned to fit the line-end gap data of D11H and then used to simulate the linewidths given in Section 5.3. The calibrated $K_1=0.1$, $D_0=5nm$ and $\omega=0$. The simulated line-end gaps are plotted in Figure 5-19. The simulated linewidths are plotted in Figure 5-20.

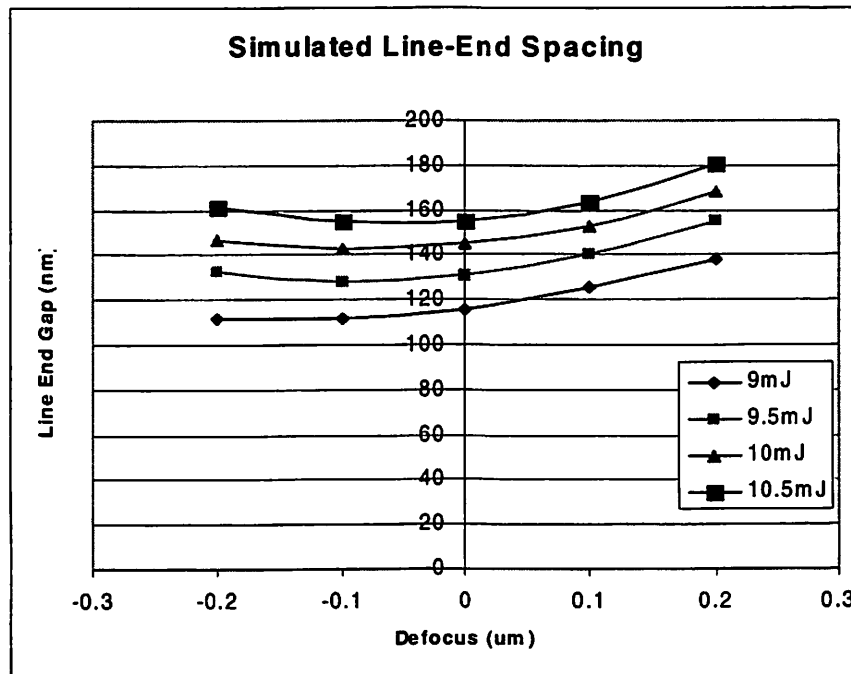
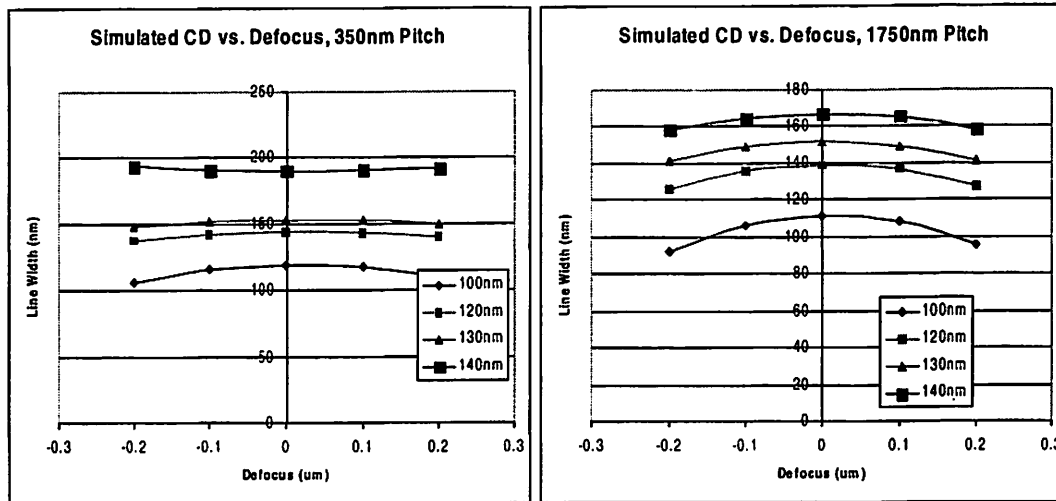


Figure 5-19 The line-end spacing of D11H simulated with PEB model



(a)

(b)

Figure 5-20 The linewidths simulated by PEB model

Here (a) is 350nm pitch and (b) is 1750nm pitch.

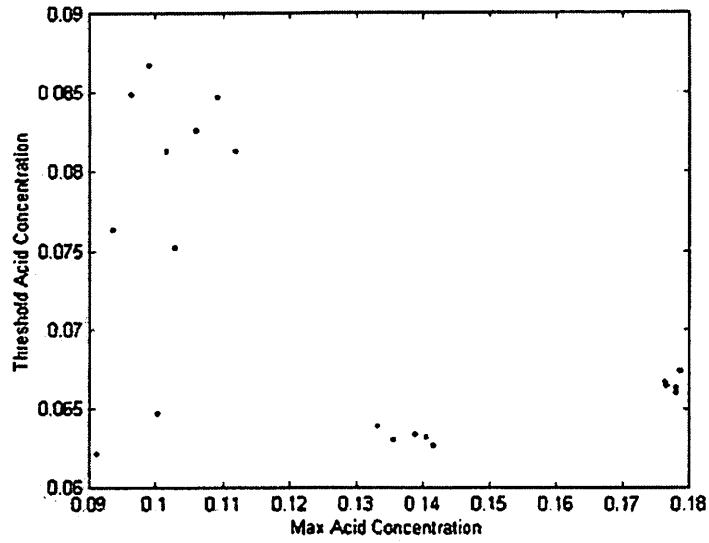
It can be seen that PEB model reduces the error of predicting line-end gaps at the cost of increasing the error of predicting linewidth. The RMS error of simulating line-end gap is 37nm and of simulating linewidths is 27.8nm. As a comparison, the RMS error of resist imaging model in predicting line-end gap is 43.6nm and in predicting linewidth is 5.28nm. Thus the linewidths are not sensitive to PEB process while the line-end gaps are. By including PEB model, the simulation of line-end gaps is improved by 15% but the error of linewidth simulation is too large for CD control purpose.

In PEB process, the line ends are exposed to larger bright area that line edges are. Thus the amount of acid diffusing into line ends is usually larger than into lines, which leads to line-end shortening effect, a common phenomenon in 248nm lithography. By using image and PEB simulation, Chapter 2 successfully explained the LES effect in KrF

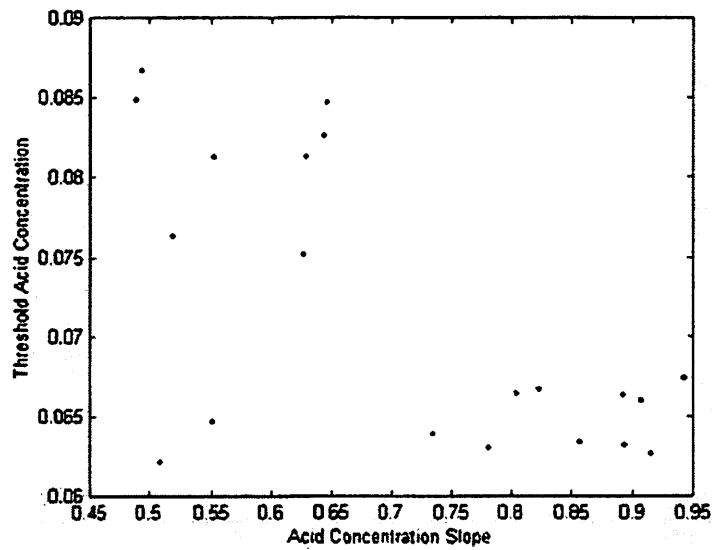
lithography. Note that the peak light intensity in gaps is much lower than near lines, as is seen in Figure 5-18. In high-contrast KrF resists, this does not cause trouble because the middle of gaps can still be developed almost instantly at the beginning of develop. Then the developer advances until hitting resist whose dissolution rate is about 0. Thus the lines and gaps have the same threshold light intensity in KrF lithography. The line-end shortening is basically due to optical approximating and acid diffusion. In 193nm lithography, however, the resist contrast is low. During develop, it may take some time for develop to open the middle of gaps and then advance. Thus the threshold is higher than in the case of lines. Therefore it is compellingly necessary to include a dissolution model into simulation, which will be discussed in next section.

5.8 Analysis of Dissolution Model

Variable-threshold models have been used extensively in OPC[34][35]. The threshold light intensity is usually assumed to be a function of light intensity slope. To illustrate how the light intensity distribution affect the threshold, the thresholds which result in experimental CDs are plotted vs. acid concentration slope and peak acid concentration in Figure 2-21. Using acid concentration instead of light intensity is to adjust the effects of different dose. It can be seen that the threshold is not strongly correlated to slope. Instead, the threshold is approximately a constant if the peak acid concentration is above 0.03. When peak acid concentration is less than 0.03, threshold appears to be increasing as peak and slope of acid concentration decreases. This phenomenon indicates a variable-threshold model is not adequate if the impact of peak intensity is not included.



(a)



(b)

Figure 5-21 The correlation of threshold acid concentration with peak acid intensity and acid intensity slope

Here (a) plots threshold vs. peak intensity and (b) plots threshold vs. slope.

A 1-dimensional dissolution model was developed as a possible factor for this various threshold phenomenon. Suppose the dissolution rate along a line is $r(x)$, and the maximum dissolution rate is at $x=0$. At other points, the dissolution rate is assumed to be so low that the vertical dissolution of the resist at that point can be neglected. Only the point at the $x=0$ can be developed vertically. This assumption is valid if the resist contrast is high enough. After the resist at $x=0$ is developed, its neighboring resist can be and can only be dissolved by the developer filling $x=0$. This assumption is approximately true given the fact that the sidewall area is much than the resist surface area. Then the time for developer to dissolve the resist at x with length dx is

Equation 5-7 $dt = dx / r(x)$

Then the developer advances to dissolve the resist at $x+dx$. Thus the resist being developed during time T is determined by

Equation 5-8 $\int_0^L \frac{dx}{r(x)} = T - \frac{h}{r(0)}$

Where L is the length of the resist having been developed, h is the resist thickness and $h/r(0)$ is the time needed to develop the resist at $x=0$. It is similar to the dissolution model proposed by C. Mack[32].

The dissolution rate is a function of activated site concentration, which is usually described by enhanced Mack Model[62][63]:

Equation 5-9 $r(s) = R_{resin} \cdot \frac{1 + K_{enh} \cdot s^n}{1 + K_{inh} (1-s)^l}$

Where s is the normalized activated site concentration, K_{enh} is the enhanced dissolution constant, K_{inh} is the inhibition dissolution rate, R_{resin} is the resin dissolution rate.

The parameters given by International SEMATECH are: $R_{resin}=550\text{nm/s}$, $R_{min}=0.05\text{nm/s}$, $R_{max}=568\text{nm/s}$, $n=14$, $l=12$.

If the acid diffusion in PEB is ignored, the activated site concentration is given by

Equation 5-10 $s = 1 - e^{-K_1 C_a t}$

Where K_1 is the reaction rate, C_a is the photoacid concentration and t is PEB time.

Figure 5-22 plots the dissolution rate as a function of normalized activated site concentration.

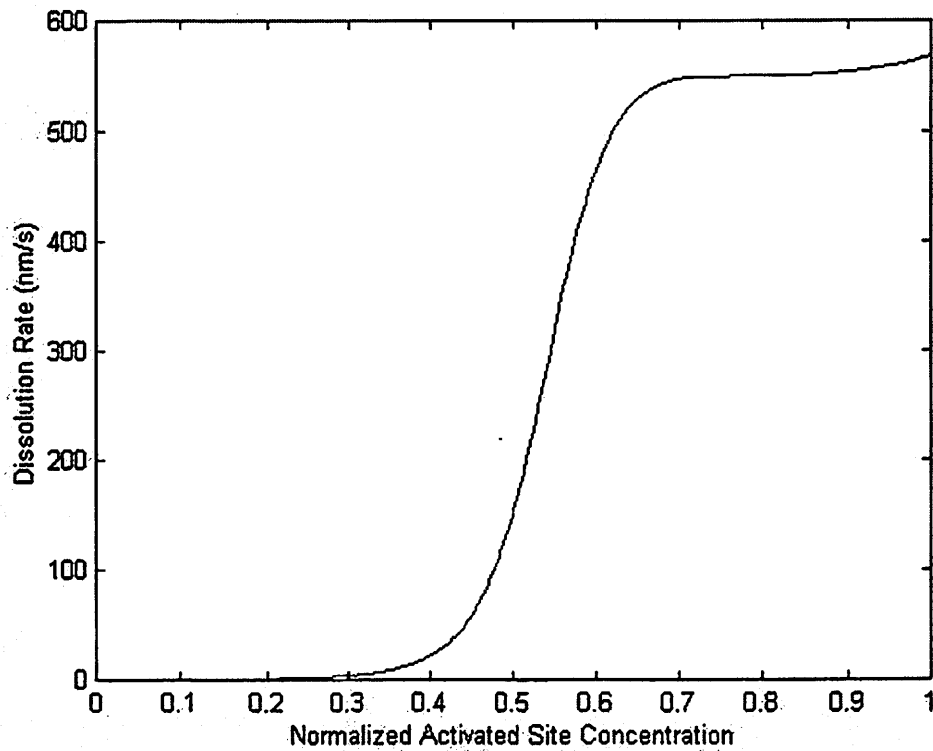


Figure 5-22 Dissolution rate of PAR710 vs. normalized activated site concentration

To simplify the dissolution modeling, it is assumed that acid diffusion is negligible and thus dissolution rate is a direct function of acid concentration. Furthermore, the curve plotted in Figure 5-22 is approximated as 3 line segments, similar to the Lumped Parameter Model proposed by C. Mack[32]. In another word, the dissolution rate as a function of acid concentration is given by

$$\text{Equation 5-11} \quad r(c) = \begin{cases} 0 & c < c_0 \\ R_{\max} \cdot \frac{c - c_0}{c_1 - c_0} & c_0 \leq c \leq c_1 \\ R_{\max} & c > c_1 \end{cases}$$

Where c is acid concentration, c_0 and c_1 are cutoff acid concentrations and R_{\max} is the maximum dissolution rate. Furthermore, assume the acid concentration is a linear function of position x , which is approximately true in the region where light intensity transits from high to low. Then the dissolution rate as a function of position x is

$$\text{Equation 5-12} \quad r(x) = \begin{cases} r_0 - \beta x & x \leq \frac{r_0}{\beta} \\ 0 & x > \frac{r_0}{\beta} \end{cases}$$

Substituting Equation 5-12 to 5-18, the advancing length of resist is given by

$$\text{Equation 5-13} \quad L = \frac{r_0}{\beta} (1 - e^{-\beta(t-h/r_0)})$$

To make this calculation easy to use, an equivalent threshold acid concentration is derived which is the acid concentration at $x=L$. Thus this equivalent threshold can be directly put into resist imaging model to determine the CD. The threshold can be shown to be

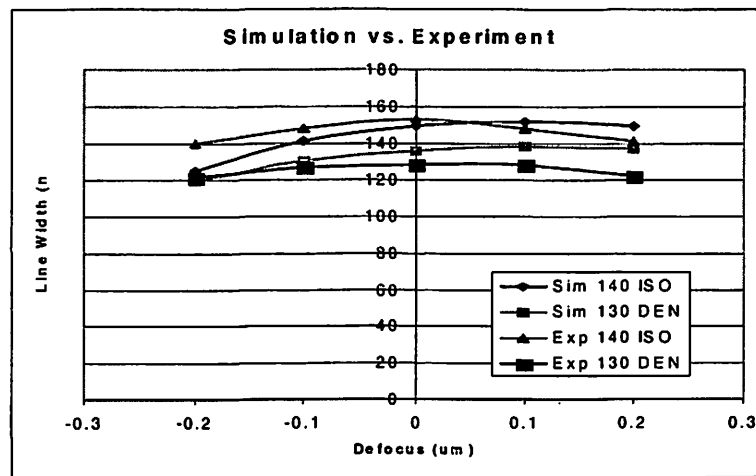
$$\text{Equation 5-14} \quad T_c = c_{\max} \cdot \exp\left(-kt + k \cdot \frac{h}{c_{\max}}\right)$$

Where c_{\max} is the maximum acid concentration along the line, k is the slope of acid concentration along this line, t and h are constants to be determined.

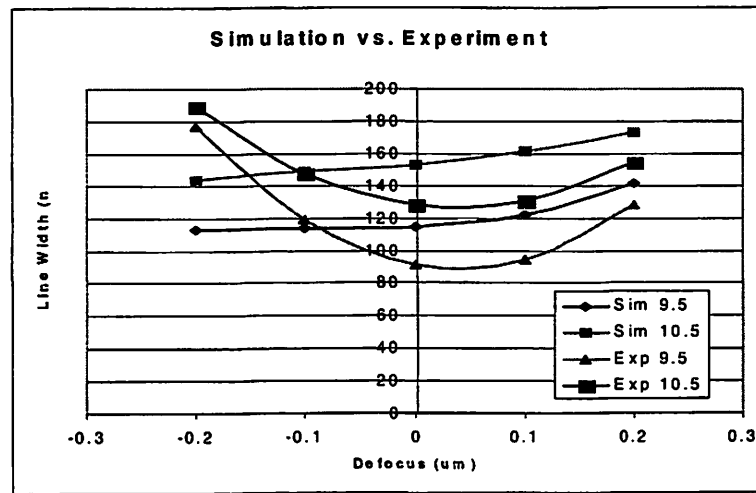
On the other hand, T_c must be greater than c_0 . Thus the threshold acid concentration is

Equation 5-15
$$T_c = \max\left\{c_0, c_{\max} \cdot \exp\left(-kt + k \cdot \frac{h}{c_{\max}}\right)\right\}$$

The resist imaging model was modified to include this dissolution rate effects. After obtaining the acid concentration of the patterns, the line at which the CD is measured is extracted and the maximum and slope of acid concentration are calculated. Then threshold acid concentration is determined by Equation 5-15. Then the threshold is used to find out the CDs. The parameters in this dissolution model, t and h , were extracted by fitting CDs with 140nm isolated line, 130nm lines at 350nm pitch, D11H gap at 9.5 and 10.5mJ/cm². The simulations are compared with experiments in Figure 5-23. The RMS error of gaps is reduced to 24nm, 33% less than PEB model and half the imaging model. Meanwhile, the RMS error of linewidth prediction is less than 6%, because this dissolution model becomes single-threshold model when peak and slope intensity are large, which is true for lines.



(a)



(b)

Figure 5-23 Comparing experiment with simulation using Dissolution model

Here (a) plots the linewidths and (b) plots the gaps.

5.9 Conclusions

In this chapter, first the resist imaging model was implemented to predict the line CDs. With only one parameter, the threshold photoacid concentration, fitted at one dose $9.5\text{mJ}/\text{cm}^2$, the model shows very good performance. It calculates the linewidths through dose, through focus, through pitch and through line-width with RMS error of 5.28nm .

The SEM measurements were noisy due to the resist LER and slimming phenomena, and the measurement error is believed to be more than 10nm. Meanwhile, the process variation, if well controlled, is about 5% of the nominal CD, i.e., 6.5nm. Thus the error is less than measurement or process errors, which makes it sufficient for the purpose of mask verification. By comparing experiments with simulations, it is shown that the lens aberrations are critical to the choice of best focus. The focal plane should be shifted to compensate for the lens aberrations. With lens aberrations, the through-dose, through-focus CD variation can be predicted very well. On the other hand, the mask CD errors are the main factors that determine the wafer CD errors. The unexpected isolated-dense bias is mostly due to mask CD bias.

Then the model was applied to simulate 2D resist patterns. The simulation fits well with the experimental SEM pictures through dose and through focus, even though the parameter was only trained at one dose. The mismatch area is generally around 14% of the pattern area. However, the model failed in predicting line-end gaps. The experiment gaps are much larger than predicted, which is believed to be caused by chemical effects such as PEB or develop.

The PEB model was applied to simulate the patterns and the diffusivity and reaction rate were tuned to fit the experimental gaps. By incorporating PEB model, the RMS error of predicting gaps was reduced from 43.6nm to 37.0nm, or 15%, whereas the RMS error of predicting linewidths was 27nm. Note that at the line ends, the LER is particularly severe and the resist, due to its small bulk, is more sensitive to SEM. Thus the measurement error is believed to be much larger than along lines. Further improvement of simulation performance was achieved by incorporating a 1D linear-dissolution-rate model to

describe the low-contrast of 193nm resists. The dissolution model reduced the RMS error of predicting gaps down to 24nm, a 50% improvement on PEB model. A resist imaging model, combined with PEB and 2D/3D dissolution model, is expected to solve the prediction problem. Since line ends are very sensitive to PEB while linewidths are not, the PEB model should be trained at the line-end gaps. Moreover, more experiments are needed in which PEB times should be varied to differentiate the effects of PEB and dissolution.

6 Electric-Field-Enhanced Post

Exposure Bake Technique:

Theory and Simulation

6.1 Introduction

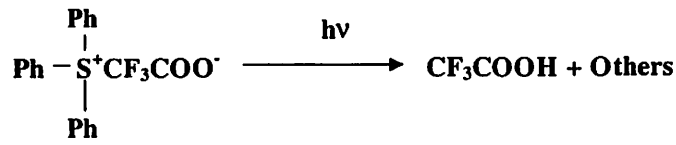
Electrical field has been used for long time to control physical motions of charged particles. A technique broadly used is electrophoresis, which uses electric field to separate charged particles such as nucleic acids and proteins by size and charge[64][65]. There exists similar charged particle motion in chemically amplified resists[66]. Chemically amplified resists are based on the acid catalyzed deprotection of functioning groups in a polymer matrix. During the post exposure bake (PEB) step, several chemical and physical processes take place. Photoacid catalyzes the deblocking process[67], in which the blocked insoluble polymer is converted to a soluble polymer with hydroxyl group and a volatile component. The volatile group then generates free volume that enhances the photoacid diffusivity. Meanwhile, the photoacid can be deactivated by neutralization and evaporation, or be trapped due to lack of free volume. Some of the resist systems also suffer from substrate or air contaminations[68].

For the purpose of CD control, it is desired to confine the acid in the vertical direction and reduce the lateral acid diffusion/deprotection, which is a key limiting factor on line-

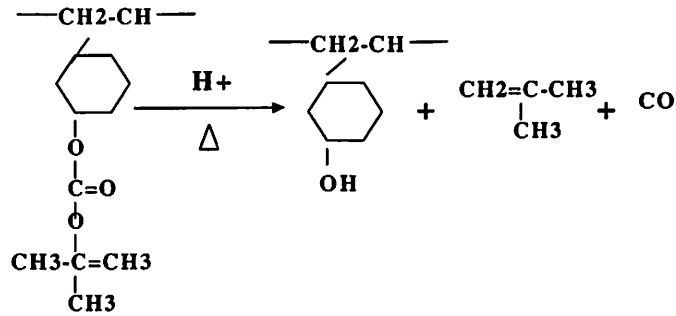
end shortening and CD bias[69]. Since the photoacid carries positive charge, an external electric field present in the resist film can force it to drift along certain direction. This is the same principle of electrophoresis. Electrophoresis is applied to particles in fluid, where the particles have long motion length. In resists, the acid diffusion length is usually less than several tens of nanometers, which may have severe effect since IC devices are approaching sub-100nm regime. Thus in this chapter a method for improving resist resolution based on acid drift in external electric field is presented. In this setup, an alternating electric field is applied vertically across the resist film during the PEB. It will force the acid to drift back and forth in the vertical direction and confine its lateral diffusion. The method is termed electric-field-enhanced PEB (EFE-PEB). In this chapter, a math model of EFE-PEB is first presented and a rigorous solution is obtained under the assumption of Fickian diffusion and constant electric field. Then the experiments on UVIIHS resist and JEOL electron-beam exposure tool is described and discussed.

6.2 Post Exposure Bake Model

The radiation of photon or electron will generate photoacid in chemically amplified resists, as is described in Figure 6-1 (a). Then in PEB process, the photoacid is thermally split into a positively charged proton and a negatively charged anion. The proton catalyzes the deprotection reaction of the polymer matrix of resist, in which the blocked insoluble polymer is converted to a soluble polymer with hydroxyl group and a volatile component, as is described in Figure 6-1 (b). Then the volatile group generates free volume and enhances the acid diffusivity.



(a)



(b)

Figure 6-1 Chemical reactions of resist in exposure and PEB.

(a) is the photochemical reaction in exposure, in which an acid CF_3COOH is generated by photon or electron. (b) is the deprotection reaction in PEB, catalyzed by the proton H^+ .

In the presence of electric field, post exposure bake processes can be described via the following partial differential equations:

Equation 6-1

$$\frac{\partial C_{as}}{\partial t} = K_1(1 - C_{as})C_a^m$$

$$\frac{\partial C_a}{\partial t} = \nabla \cdot (D\nabla C_a) - \nabla \cdot (\mu \mathbf{E} C_a) - K_2 C$$

Where C_{as} is the activated site concentration, C_a is the photoacid concentration, K_1 is the reaction rate, D is the photoacid diffusivity in the resist, K_2 is the photoacid loss rate, and \mathbf{E} is the electric field.

The explanation of Equation 6-1 is in Chapter 3, Section 3.2. Note that in the second equation, the second term $-\nabla \cdot (\mu \mathbf{E} C_a)$ is the acid drift term, where μ is the acid mobility in the resist.

The acid mobility μ is related to acid diffusivity D by the Einstein equation:

Equation 6-2
$$\mu = \frac{qD}{kT}$$

Where q is the charge of the proton, k is Boltzman constant and T is PEB temperature.

To improve the resist profile, i.e., to obtain 90° resist sidewall, it is desired to enhance the acid drift in the vertical direction and reduce the acid diffusion in the horizontal direction. Hence the electric field is applied along the vertical direction, as is illustrated in Figure 6-2.

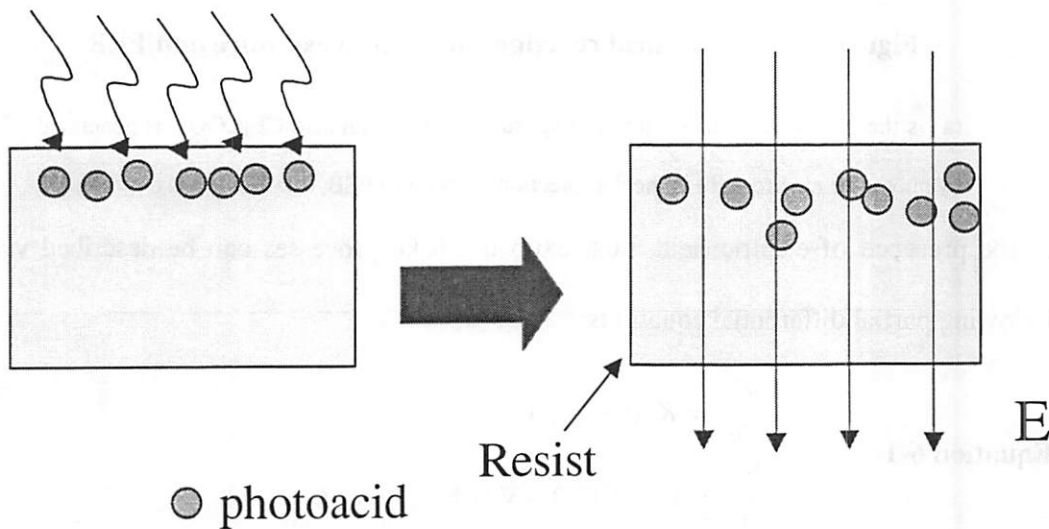


Figure 6-2 Principle of electric-field-enhanced post-exposure baking.

The acid is generated in exposure, and its drift in the vertical direction is enhanced by electric field. Note that a vertically uniform resist profile, i.e., 90° resist sidewall, is desired. Therefore a vertically directed electric field is needed.

6.3 Rigorous Solution to Electric-Field-Enhanced Post Exposure Bake

Model

In general, the acid diffusivity D is not a constant during the PEB process. Instead, it is usually a function of the extent to which the resist has been deprotected, because the free volume generated in PEB usually enhances the acid diffusivity by creating additional diffusion path. A relation between acid diffusivity and activated site concentration is proposed in [70][23]:

Equation 6-3
$$D = D_0 e^{\omega C_a}$$

In some resists, for example, UVIIHS, acid diffusivity can be considered as a constant during PEB. That is, $\omega = 0$, which corresponds to Fickian diffusion. In the case of isotropic Fickian diffusion and constant electric field in PEB, the EFE-PEB model can be rigorously solved. For simplicity, E is assumed to be at the vertical direction (z axis). The lateral directions are x and y axis. Assume $z=0$ corresponds to the resist bottom, and $z=L_z$, $L_z>0$, corresponds to the resist top surface. The resist is assumed to be a box bordered by $0 \leq x \leq L_x, 0 \leq y \leq L_y, 0 \leq z \leq L_z$. The coordinate system is depicted in Figure 6-3.

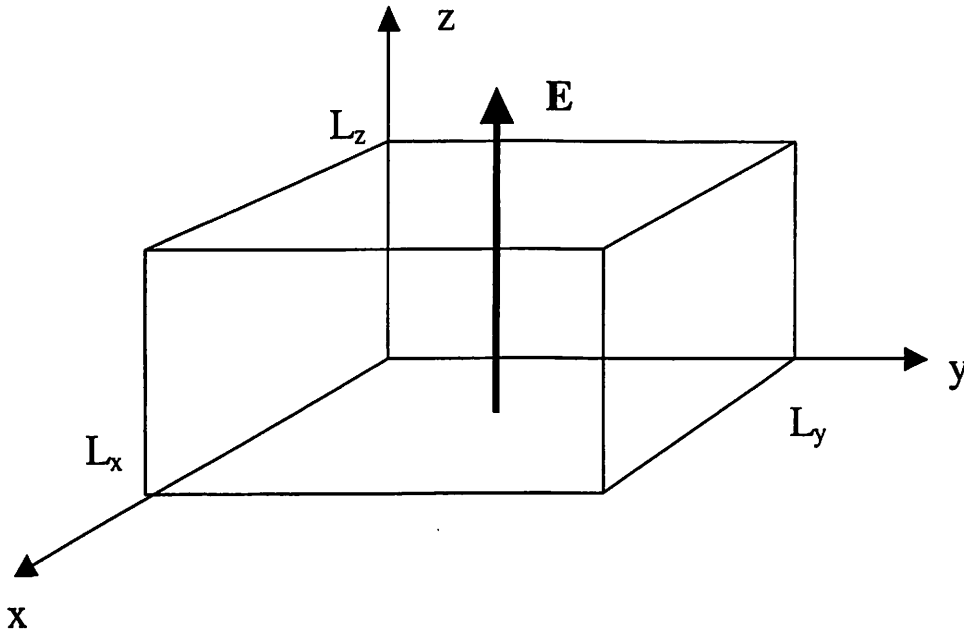


Figure 6-3 The coordinate system used in solving EFE-PEB model.

The resist is a box $[0, L_x] \times [0, L_y] \times [0, L_z]$, and z is vertical direction. E is along z axis.

In this coordinate system, Equation 6-1 can be written as

Equation 6-2
$$\frac{\partial C_{as}}{\partial t} = K_1(1 - C_{as})C_a^m$$

Equation 6-3
$$\frac{\partial C_a}{\partial t} = D\left(\frac{\partial^2}{\partial x^2} + \frac{\partial^2}{\partial y^2} + \frac{\partial^2}{\partial z^2}\right)C_a - \mu E \frac{\partial C_a}{\partial z} - K_2 C_a$$

The boundary conditions are

Equation 6-4
$$C_{as}(x, y, z, 0) = 0$$

Equation 6-5
$$C_a(x, y, z, 0) = c(x, y, z)$$

Equation 6-6
$$-D \frac{\partial C_a}{\partial x} = 0, \quad \text{at } x = 0, L_x$$

Equation 6-7
$$-D \frac{\partial C_a}{\partial y} = 0, \quad \text{at } y = 0, L_y$$

Equation 6-8
$$-D \frac{\partial C_a}{\partial z} + \mu E C_a = 0, \quad \text{at } z = 0, L_z$$

Equation 6-4 means the initial activated site concentration is 0 everywhere. This assumption means no deprotection reactions occur before the PEB process. The assumption is valid if the thermal deprotection in room temperature can be ignored, or equivalently, the activation energy of the deprotection reaction is high enough. Note that the deprotection reaction is Arrhenius reaction [85] (see Equation 3-28). Most resist systems satisfy this boundary condition.

Equation 6-5 gives the initial photoacid concentration.

Equation 6-6, 6-7 and 6-8 mean that there is no acid flux in or out of the resist boundary. This assumption is valid if there is no acid evaporation, air/silicon surface contamination or acid diffusion into silicon. Note that the acid flux is determined only by the diffusion at the x and y boundaries, whereas at the z boundaries, the flux is determined by both diffusion and drift.

Equation 6-2 can be solved as an ordinary differential equation (ODE) and its solution is

Equation 6-9
$$C_{as}(x, y, z, t) = 1 - \exp(-K_1 \int_0^t C_a^m(x, y, z, \tau) d\tau)$$

Thus I will focus on the solution to Equation 6-3 under the restriction of Equation 6-6, 6-7 and 6-8. First, let

Equation 6-10
$$C_a(x, y, z, t) = F(x, y, z, t)e^{-K_2 t}$$

Substituting Equation 6-10 to Equation 6-3:

$$e^{-K_2 t} \frac{\partial F}{\partial t} - K_2 e^{-K_2 t} F = e^{-K_2 t} D \left(\frac{\partial^2}{\partial x^2} + \frac{\partial^2}{\partial y^2} + \frac{\partial^2}{\partial z^2} \right) F - e^{-K_2 t} \mu E \frac{\partial F}{\partial z} - K_2 F e^{-K_2 t}$$

Therefore the following equation is obtained:

$$\text{Equation 6-11} \quad \frac{\partial F}{\partial t} = D\left(\frac{\partial^2}{\partial x^2} + \frac{\partial^2}{\partial y^2} + \frac{\partial^2}{\partial z^2}\right)F - \mu E \frac{\partial F}{\partial z}$$

Then let

$$\text{Equation 6-12} \quad F = X(x)Y(y)Z(z)T(t)$$

Substituting Equation 6-12 into Equation 6-11 and separating coefficients:

$$\text{Equation 6-13} \quad \frac{1}{T} \frac{dT}{dt} = \frac{D}{X} \frac{d^2 X}{dx^2} + \frac{D}{Y} \frac{d^2 Y}{dy^2} + \frac{1}{Z} \left(D \frac{d^2 Z}{dz^2} - \mu E \frac{dZ}{dz} \right)$$

The solution to Equation 6-13 can be obtained by finding the eigen functions of three differential equations:

$$\text{Equation 6-14} \quad \frac{d^2 X}{dx^2} = \lambda_x X$$

$$\text{Equation 6-15} \quad \frac{d^2 Y}{dy^2} = \lambda_y Y$$

$$\text{Equation 6-16} \quad \frac{d^2 Z}{dz^2} - \frac{\mu E}{D} \frac{dZ}{dz} = \lambda_z Z$$

$$\text{Equation 6-17} \quad \frac{dT}{dt} = D(\lambda_x + \lambda_y + \lambda_z)T$$

Here X , Y and Z must also satisfy the boundary conditions:

$$\text{Equation 6-18} \quad \left. \frac{dX}{dx} \right|_{x=0} = \left. \frac{dX}{dx} \right|_{x=L_x} = 0$$

$$\text{Equation 6-19} \quad \left. \frac{dY}{dy} \right|_{y=0} = \left. \frac{dY}{dy} \right|_{y=L_y} = 0$$

$$\text{Equation 6-20} \quad \left(-\frac{dZ}{dz} + \frac{\mu E}{D} Z \right)_{z=0} = \left(-\frac{dZ}{dz} + \frac{\mu E}{D} Z \right)_{z=L_z} = 0$$

The eigenfunctions of Equation 6-14 with the boundary condition 6-18 can be easily solved:

$$\text{Equation 6-21} \quad X_m(x) = \cos\left(\frac{m\pi x}{L_x}\right), \lambda_{m,x} = -\left(\frac{m\pi}{L_x}\right)^2, m = 0, 1, 2, \dots$$

Similarly, the eigenfunctions of Equation 6-15 with the boundary conditions 6-19 are

$$\text{Equation 6-22} \quad Y_n(y) = \cos\left(\frac{n\pi y}{L_y}\right), \lambda_{n,y} = -\left(\frac{n\pi}{L_y}\right)^2, n = 0, 1, 2, \dots$$

To find the eigenfunctions of Equation 6-16 with the boundary condition 6-20, let

$$\text{Equation 6-23} \quad v = \frac{\mu E}{D}$$

$$Z(z) = e^{\sigma z}$$

Substituting Equation 6-23 to Equation 6-16:

$$\text{Equation 6-24} \quad \sigma^2 - v\sigma - \lambda_z = 0$$

Thus Equation 6-16 has 2 degenerated eigenfunctions:

$$\text{Equation 6-25} \quad \exp(\sigma^+ z), \exp(\sigma^- z)$$

$$\sigma^+ = \frac{v + \rho}{2}, \sigma^- = \frac{v - \rho}{2}, \rho = \sqrt{v^2 + 4\lambda_z}$$

The reason of denoting ρ as $\sqrt{v^2 + 4\lambda_z}$ will be shown shortly.

According to Equation 6-25, the complete eigenfunction of Equation 6-24 can be written in the following form:

$$\text{Equation 6-26} \quad \zeta(z) = a^+ \exp(\sigma^+ z) + a^- \exp(\sigma^- z)$$

$\zeta(z)$ must satisfy the boundary condition Equation 6-20. Substituting Equation 6-26 into Equation 6-20:

$$\begin{aligned} \text{Equation 6-27} \quad & a^+(\sigma^+ - \nu) + a^-(\sigma^- - \nu) = 0 \\ & a^+(\sigma^+ - \nu)e^{\sigma^+ L_z} + a^-(\sigma^- - \nu)e^{\sigma^- L_z} = 0 \end{aligned}$$

To make $\zeta(z)$ a nontrivial function, either a^+ or a^- is not 0, which requires

$$\text{Equation 6-28} \quad e^{\sigma^+ L_z} = e^{\sigma^- L_z}$$

Substituting Equation 6-25 to Equation 6-28:

$$\begin{aligned} \text{Equation 6-29} \quad & \exp\left(\frac{\nu + \rho}{2} L_z\right) = \exp\left(\frac{\nu - \rho}{2} L_z\right) \\ & \Rightarrow \rho L_z = j2p\pi, p = 0, 1, 2, \dots \end{aligned}$$

Then from Equation 6-27, a^+ and a^- can be solved:

$$\text{Equation 6-30} \quad \frac{a^-}{a^+} = -\frac{\sigma^+ - \nu}{\sigma^- - \nu} = \frac{\rho - \nu}{\rho + \nu}$$

From the above discussion, the eigenfunctions of Equation 6-16 with the boundary condition 6-20 can be written as

$$\text{Equation 6-31} \quad \zeta_p(z) = e^{z\left(\frac{\nu + j p \pi}{2} L_z\right)} + \frac{j2p\pi - \nu L_z}{j2p\pi + \nu L_z} e^{z\left(\frac{\nu - j p \pi}{2} L_z\right)}, p = 0, 1, 2, \dots$$

From Equation 6-25 and 6-29, the eigen value of Equation 6-16 corresponding to $\zeta_p(z)$ is given by

$$\text{Equation 6-32} \quad \lambda_{p,z} = -\left(\frac{p\pi}{L_z}\right)^2 - \left(\frac{\nu}{2}\right)^2$$

Substituting Equation 6-21, 6-22, and 6-32 into Equation 6-17:

$$\begin{aligned} \text{Equation 6-33} \quad & \frac{dT}{dt} = -D \left[\left(\frac{m\pi}{L_x}\right)^2 + \left(\frac{n\pi}{L_y}\right)^2 + \left(\frac{p\pi}{L_z}\right)^2 + \left(\frac{\nu}{2}\right)^2 \right] T \\ & m, n, p = 0, 1, 2, \dots \end{aligned}$$

Therefore $T(t)$ is given by

$$\text{Equation 6-34} \quad T_{m,n,p}(t) = \exp \left\{ -D \left[\left(\frac{m\pi}{L_x} \right)^2 + \left(\frac{n\pi}{L_y} \right)^2 + \left(\frac{p\pi}{L_z} \right)^2 + \left(\frac{v}{2} \right)^2 \right] t \right\}$$

Combining the above discussion, it can be seen that the solution to Equation 6-11 can be written as a linear combination of products of $X_m(x), Y_n(y), \zeta_p(z), T_{m,n,p}(t)$. That is,

$$\text{Equation 6-35} \quad F(x, y, z, t) = \sum_{m=0}^{\infty} \sum_{n=0}^{\infty} \sum_{p=0}^{\infty} C_{mnp} \cos \left(\frac{m\pi x}{L_x} \right) \cos \left(\frac{n\pi y}{L_y} \right) \zeta_p(z) e^{-D\lambda_{mnp}t}$$

$$\zeta_p(z) = e^{z \left(\frac{v}{2} + \frac{jp\pi}{L_z} \right)} + \frac{j2p\pi - vL_z}{j2p\pi + vL_z} e^{z \left(\frac{v}{2} - \frac{jp\pi}{L_z} \right)}$$

$$\lambda_{mnp} = \left(\frac{m\pi}{L_x} \right)^2 + \left(\frac{n\pi}{L_y} \right)^2 + \left(\frac{p\pi}{L_z} \right)^2 + \left(\frac{v}{2} \right)^2$$

where the coefficients C_{mnp} are determined by the initial acid concentration 6-5, and can be obtained by orthogonal expansion, since $F(x, y, z, t)$ has been expressed in the form of orthogonal basis functions. For this purpose, the normalization factors for the eigenfunctions are calculated first.

$$\int_0^{L_x} \cos^2 \left(\frac{m\pi x}{L_x} \right) dx = \frac{L_x}{2}$$

$$\text{Equation 6-36} \quad \int_0^{L_y} \cos^2 \left(\frac{m\pi y}{L_y} \right) dy = \frac{L_y}{2}$$

$$\int_0^{L_z} \zeta_p(z) \overline{\zeta_p}(z) dz = 2L_z$$

Here the function $\overline{\zeta_p}(z)$ is the complementary of $\zeta_p(z)$, which is defined as

$$\text{Equation 6-37} \quad \overline{\zeta_p}(z) = e^{-z \left(\frac{v}{2} + \frac{jp\pi}{L_z} \right)} + \frac{j2p\pi + vL_z}{j2p\pi - vL_z} e^{-z \left(\frac{v}{2} - \frac{jp\pi}{L_z} \right)}$$

Therefore, the coefficients of orthogonal expansion can be determined by

Equation 6-38

$$C_{mnp} = \frac{2}{L_x L_y L_z} \int_0^{L_x} \int_0^{L_y} \int_0^{L_z} c(x, y, z) \cdot \cos\left(\frac{m\pi x}{L_x}\right) \cos\left(\frac{n\pi y}{L_y}\right) \overline{\zeta}_p(z) dx dy dz$$

Finally, the complete solution to the PEB model is summarized as

Equation 6-39

$$C_a(x, y, z, t) = 1 - \exp(-K_1 \int_0^t C_a^m(x, y, z, \tau) d\tau)$$

$$C_a(x, y, z, t) = e^{-K_2 t} \sum_{m=0}^{\infty} \sum_{n=0}^{\infty} \sum_{p=0}^{\infty} C_{mnp} \cos\left(\frac{m\pi x}{L_x}\right) \cos\left(\frac{n\pi y}{L_y}\right) \zeta_p(z) e^{-D\lambda_{mnp} t}$$

$$C_{mnp} = \frac{2}{L_x L_y L_z} \int_0^{L_x} \int_0^{L_y} \int_0^{L_z} c(x, y, z) \cdot \cos\left(\frac{m\pi x}{L_x}\right) \cos\left(\frac{n\pi y}{L_y}\right) \overline{\zeta}_p(z) dx dy dz$$

$$\lambda_{mnp} = \left(\frac{m\pi}{L_x}\right)^2 + \left(\frac{n\pi}{L_y}\right)^2 + \left(\frac{p\pi}{L_z}\right)^2 + \left(\frac{v}{2}\right)^2$$

$$\zeta_p(z) = e^{z\left(\frac{v}{2} + \frac{jp\pi}{L_z}\right)} + \frac{j2p\pi - vL_z}{j2p\pi + vL_z} e^{z\left(\frac{v}{2} - \frac{jp\pi}{L_z}\right)}$$

$$\overline{\zeta}_p(z) = e^{-z\left(\frac{v}{2} + \frac{jp\pi}{L_z}\right)} + \frac{j2p\pi + vL_z}{j2p\pi - vL_z} e^{-z\left(\frac{v}{2} - \frac{jp\pi}{L_z}\right)}$$

$$v = \frac{\mu E}{D} = \frac{qE}{kT}$$

6.4 Numerical Picture of Electric-Field-Enhanced Post Exposure Bake

With the rigorous solution obtained in Section 6.3, some numerical computations are conducted to depict the effect of electric field in PEB.

Assume $D=50 \text{ nm}^2/\text{s}$, resist thickness $L_z=600 \text{ nm}$, PEB time 90 sec, initial acid

distribution is $C_a(x, y, z, 0) = C\delta\left(x - \frac{L_x}{2}\right)\delta\left(y - \frac{L_y}{2}\right)z$, as is illustrated in Figure 6-4. The

acid concentration linearly decreases from the top to the bottom of the resist, which is a

rough approximation to the acid distribution profile after optical radiation due to resist absorbance. Note that the acid distribution is a line source.

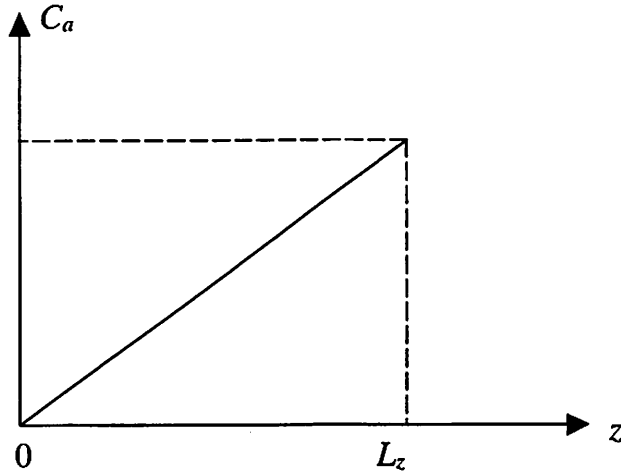


Figure 6-4 An example of acid distribution profile.

Note that $z=L_z$ corresponds to the top surface of resist. The acid concentration linearly decreases from top to bottom, which is an approximation to the acid distribution after optical exposure. To illustrate the diffusion/drift effects, the acid distribution is assumed to be a line source, i.e., all the acid is concentrated on the line $x=L_x/2, y=L_y/2$.

The acid concentration is always cylindrically symmetric about the line $x=L_x/2, y=L_y/2$, so only the acid concentration in the cross-section $y=L_y/2$ plane will be plotted. In the plots, ‘vertical’ refers to z axis, and ‘lateral’ refers to x axis. Figure 6-5, 6-6 and 6-7 plot the acid distribution profiles corresponding to $V=0, 0.2$ and 0.3 V, respectively, where V is the voltage drop from the top to the bottom of the resist film. It can be seen that the standard PEB can hardly improve the acid distribution uniformity while the 0.2V EFE-PEB can significantly smooth the acid distribution. If the voltage is as high as 0.3V,

however, the majority of acid will be shifted to the bottom of resist by the electric field, which is not desired.

Figure 6-8 compares the acid distribution after PEB along x axis, which is lateral direction. For the standard PEB ($E=0$ V/m), the acid distribution is taken at $z=L$, where the acid spreads farthest laterally. For the EFE-PEB ($E=3.3\times 10^5$ V/m, or $V=0.2V$), the acid distribution is taken at $z=L/2$, where the lateral diffusion of acid is largest. It can be seen that the EFE-PEB has smaller amount of acid diffusing laterally than standard PEB does, due to the fact that EFE-PEB can average the vertical acid distribution.

These numerical examples show that the presence of electric field can significantly alter the photoacid distribution, which thereafter impacts the activated site concentration profile. Usually a vertical resist sidewall is desired while excessive lateral acid diffusion is unwanted due to CD control purpose. Thus, a vertically directed electric field helps improving resist profile by migrating photoacid from high concentrated area (for example, top surface in optical lithography) to low concentrated area (for example, resist bottom in optical lithography). Meanwhile, the use of vertical electric field can help reducing unwanted lateral diffusion due to the reason depicted in Figure 6-8.

Prior art on the application of electric fields during PEB to control and improve resist profiles includes a pair of patents by Tokui and Yoneda[71]. Tokui and Yoneda used a DC field of 10 to 100 kV/mm on SAL-601-ER-7, described the preferred movement of the H^+ downward from an attenuated KrF exposure, and gave a schematic diagram of the resulting resist profile improvement rather than SEMs of resist profiles.

However, a simple DC field is not effective in improving the resist profile, although a properly chosen electric field magnitude can make the acid vertically uniform. In fact, it

can be proved that a simple DC field can never result in a vertically uniform resist profile. The reason is not obvious and will be discussed in next Section.

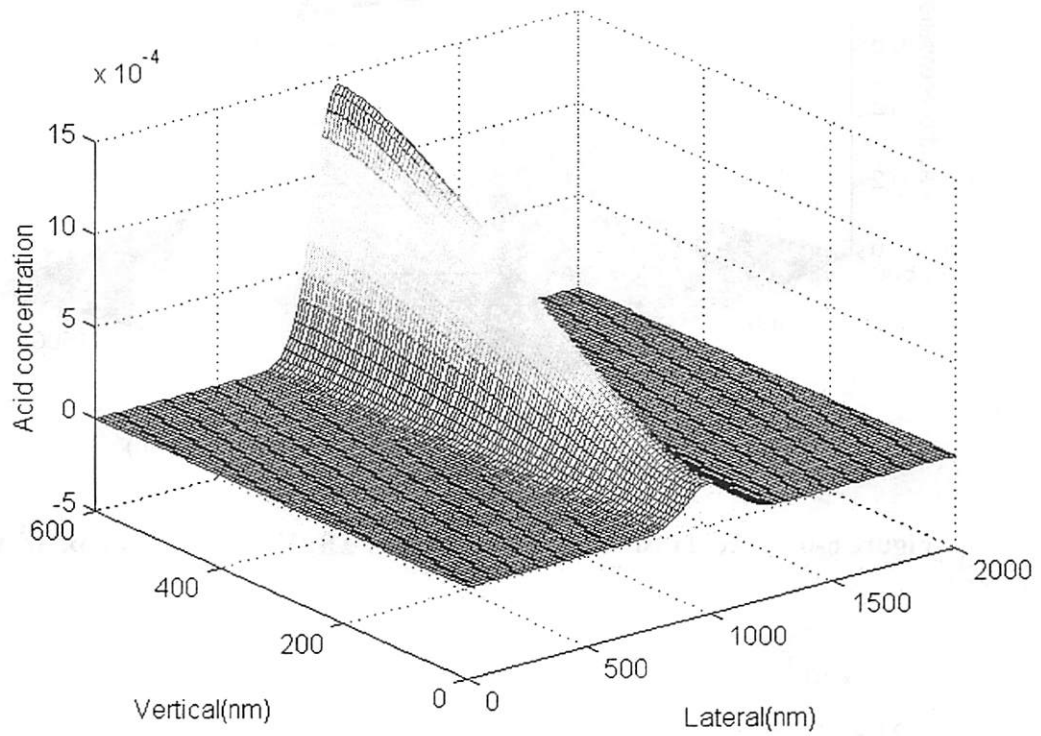


Figure 6-5 Acid distribution after standard PEB.

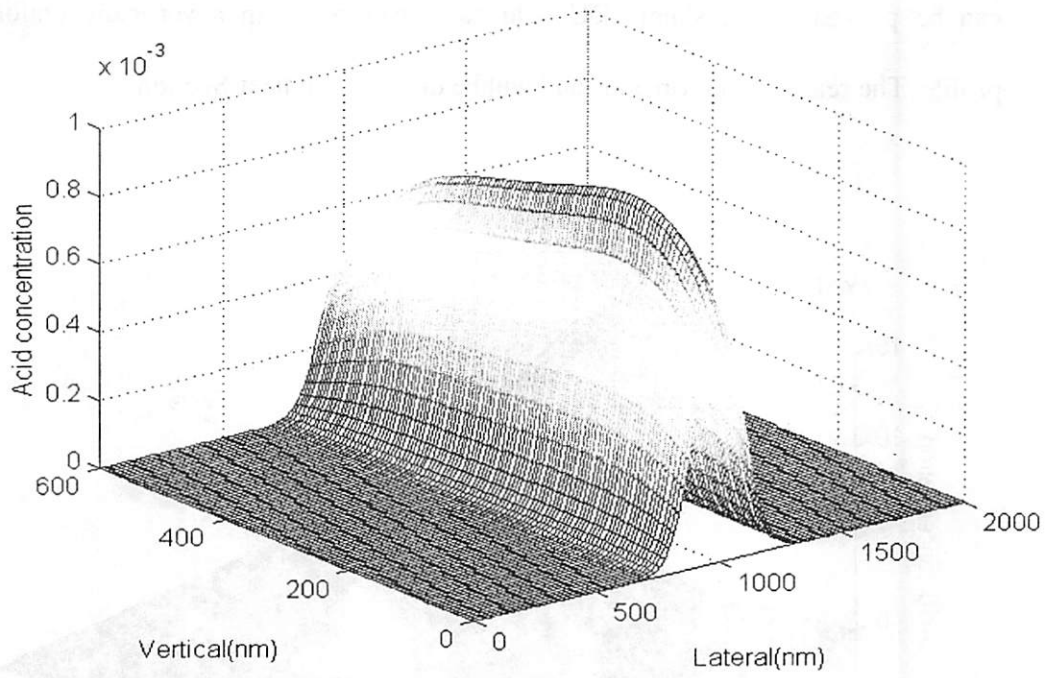


Figure 6-6 Acid distribution after EFE-PEB, $V=0.2V$ or $E=3.3 \times 10^5$ V/m.

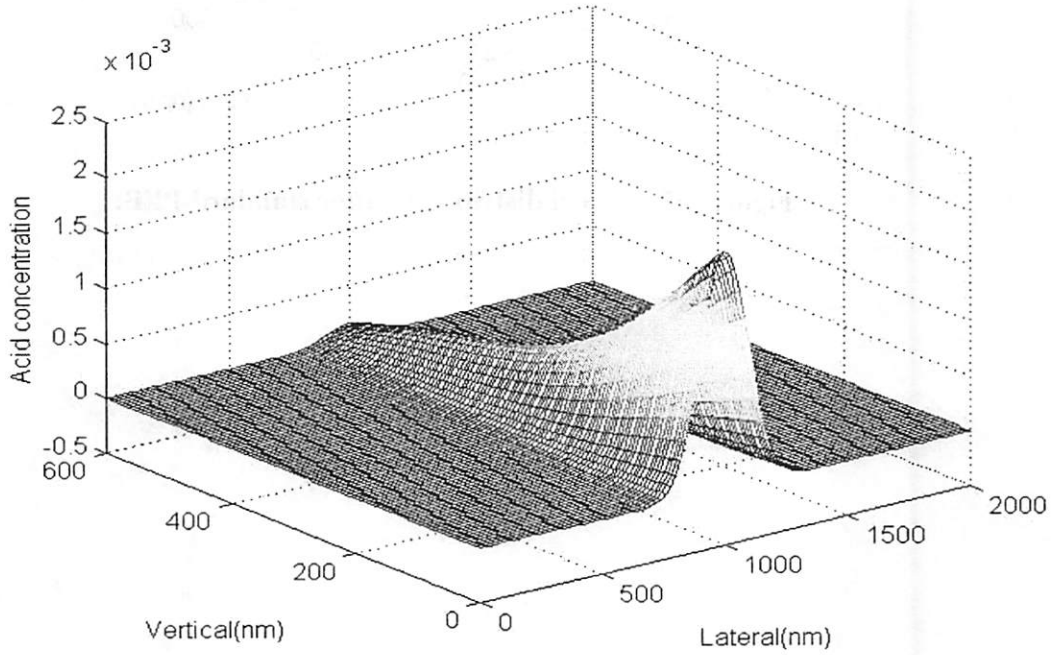


Figure 6-7 Acid distribution after EFE-PEB, $V=0.3V$ or $E=5.0 \times 10^5$ V/m.

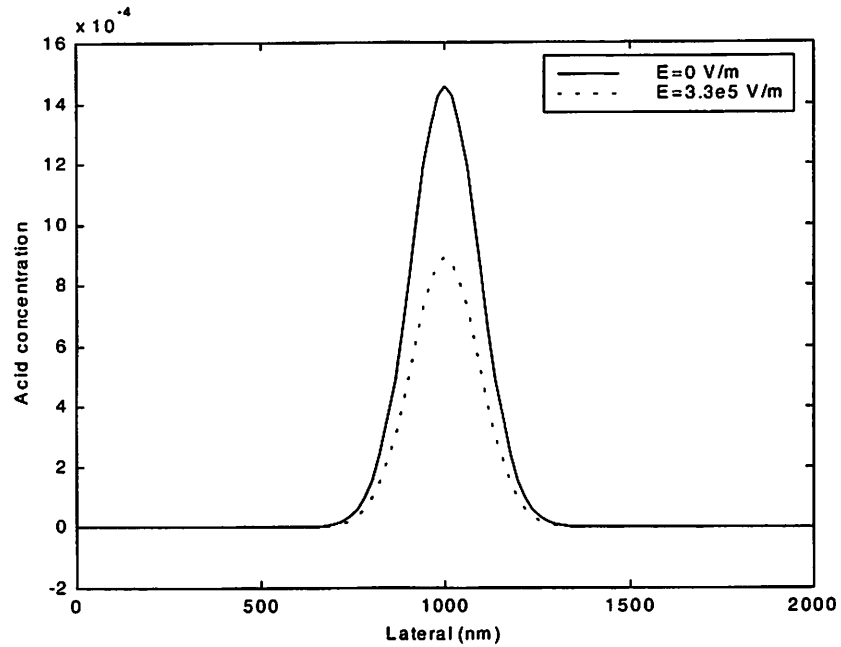


Figure 6-8 The acid lateral diffusion after standard PEB and 0.2V EFE-PEB.

6.5 The Role of Alternating Field in EFE-PEB

The dissolution rate of resist is determined by C_{as} , activated site concentration[72][73].

As is shown in Equation 6-39, C_{as} is given by

$$C_{as}(x, y, z, t) = 1 - \exp(-K_1 \int_0^t C_a^m(x, y, z, \tau) d\tau).$$

To improve the resist profile, it is desired to obtain a vertically uniform activated site concentration. From Equation 6-39, C_{as} at a certain point is determined by the amount of acid passing through this point during PEB. Optical radiation of resist yields more photoacid at the top and less at the bottom due to resist absorption. A downward electric field can help migrate photoacid towards bottom, thus results in a better resist profile. A direct field, however, is not sufficient to obtain a uniform activated site concentration,

and is not efficient in driving acid-catalyzed deprotection. To illustrate this, consider a 1-dimensional model depicted in Figure 6-9. The acid concentration linearly decreases from $z=L$ to $z=0$, and the electric field E also points from $z=L$ to $z=0$. Assume E and D is uniform in the resist layer.

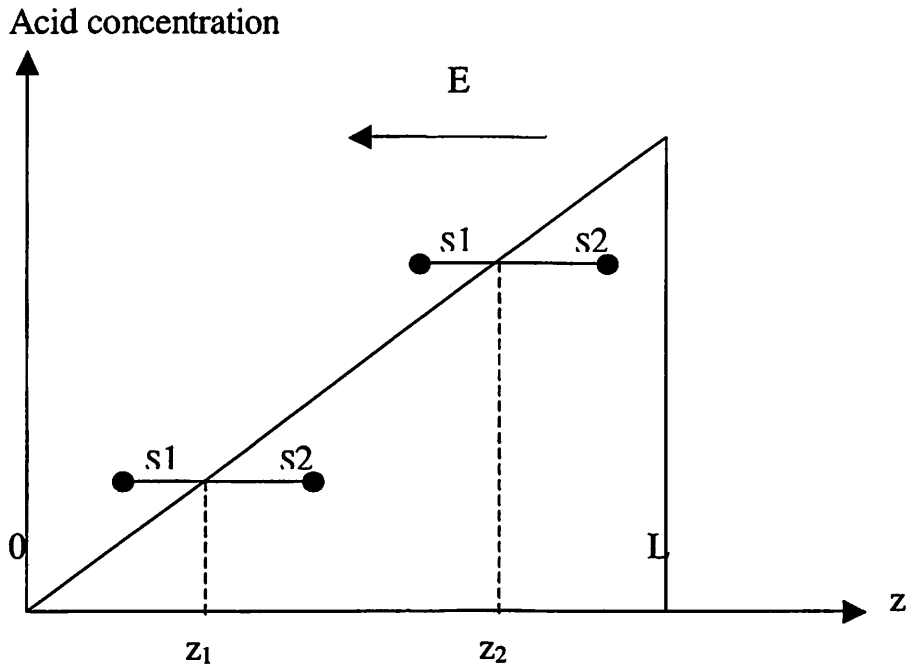


Figure 6-9 One-dimensional EFE-PEB model.

Initial acid concentration linearly decreases from $z=L$ to $z=0$. The direction of constant electric field E is negative. Any point z can be visited by acid from $[z-s_1, z+s_2]$. Note that $s_1 < s_2$.

During PEB, a given point z can be visited by the drifting/diffusing acid from the interval $[z-s_1, z+s_2]$. Obviously $s_1 < s_2$, and s_1, s_2 do not depend on z . Thus if $z_1 < z_2$, the amount of acid in interval $[z_1-s_1, z_1+s_2]$ is smaller than in interval $[z_2-s_1, z_2+s_2]$. As a result, $C_{as}(z_1)$ will be smaller than $C_{as}(z_2)$ after PEB. On the other hand, if $z_1+s_2 > L$ and $z_2+s_2 > L$, in the case of large E , then z_1 and z_2 are visited by acid from $[z_1-s_1, L]$ and $[z_2-s_1, L]$,

respectively. Thus $C_{as}(z_1)$ will be greater than $C_{as}(z_2)$. From the above discussion, it can be seen that a DC field can not result in a vertically uniform resist sidewall, no matter what magnitude the field is.

In fact there is only one case in which a DC field could result in a uniform C_{as} . That is, all the acid is concentrated on the very top surface of the resist at the beginning of PEB. In other word, the initial acid concentration is

Equation 6-40
$$C_a(z, t = 0) = C\delta(z - L)$$

This case can not occur in KrF, ArF or e-beam lithography unless the exposure dose is extremely small. In 157nm or Extreme Ultra-Violet (EUV) lithography, however, this case is common because of the high absorbance of resist at these wavelengths. The high absorbance of resist at 157nm and 13.6nm wavelengths severely limits the resist thickness, which therefore limits the resist performance as a barrier to plasma etching [19]. A potential solution to this high absorbance problem is to use a downward direct electric field to migrate the photoacid at the top of resist to the bottom during PEB, as is discussed in this chapter. This can be considered a modification of Top Surface Imaging (TSI)[74]. A term ‘Electrical-Field-Assisted Top Surface Imaging’ is proposed here for this process.

In general, the photoacid distribution is not a point source. Thus, to make C_{as} identical everywhere, a simple solution is to make s_1 and s_2 so large that any point can be visited by acid from interval $[0, L]$. Note that s_1 can only be increased by an upward electric field. Thus an alternating field, rather than a direct field, is desired to obtain vertically uniform activated site concentration. In addition to the alternating field, a small

downward direct field can also be of help by migrating the excessive acid at the top towards the bottom.

EFE-PEB with alternating field can also make the acid-catalyzed deprotection reaction more effective. In EFE-PEB, the acid ion will move much faster in the vertical direction, and it will catalyze much more deprotection reactions in the vertical direction than in the lateral direction. Compared with the standard PEB, the acid will catalyze the same number of reactions. But the increased movement of the acid in the vertical direction means that reaction events tend to occur and consume the acid along a more vertical path. This directed consumption depletes the number of catalytic events available for enabling reactions in the lateral direction and, has the effect of confining the lateral motion of the acid. It can be concluded that the lateral (unwanted) dissolution of resist will be reduced, compared with the standard PEB. Meanwhile, the vertical (desired) dissolution of resist will be enhanced due to more vertical acid motion. Thus the EFE-PEB can aggressively modify the resist profile.

From Equation 6-39, a large E is desired so that the electro-migration effect can dominate the diffusion process. On the other hand, the lateral diffusion length is estimated by $\sqrt{2Dt}$. Therefore a small PEB time t is desired to reduce acid lateral diffusion. To enhance the vertical deprotection and reduce the lateral deprotection by transporting acid, an alternating electric field with an offset bias is needed. The frequency and offset bias should be adjusted based on the acid diffusivity and different amount in the exposed/unexposed area. To choose the frequency and offset bias, two criteria have to be satisfied. First, the frequency should be low enough for the offset bias to vertically move the acids in the unexposed area for a long enough distance before the acids fully

deprotect the polymer in that area. At the same time, the frequency should be high enough for the acid in the exposed area to fully deprotect the polymer.

7 Electric-Field-Enhanced Post

Exposure Bake Technique:

Experiment

7.1 Introduction

In Chapter 6, the theory on electric-field-enhanced post exposure bake is discussed and an alternating field is theoretically shown to be able to improve resist sidewall. Furthermore, the presence of electric field in PEB can aggressively modify the resist profiles. The experiments to verify the impacts of EFE-PEB are described in this chapter and the experimental evidences are presented. The experiments conducted in electron-beam lithography are described first, and then the experimental data from KrF lithography are presented.

The diagram and voltage waveform of EFE-PEB setup are depicted in Figure 7-1. Note that the voltage in the first half period is $V+DC$ and in the second half period, it is $-V+DC$. The DC offset bias is DC while the AC component is V .

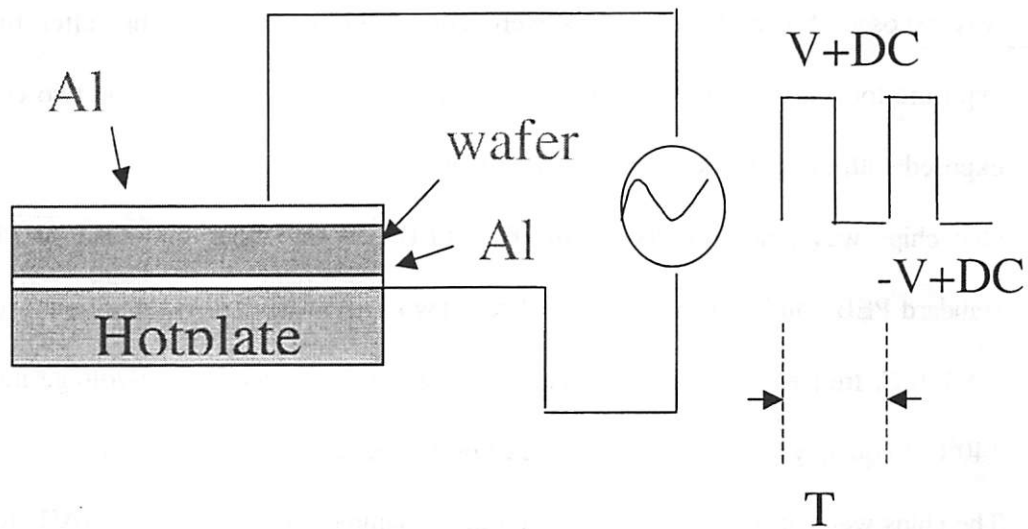


Figure 7-1 The setup of electric-field-enhanced PEB.

The wafer is in between two Al sheets, to which the cathodes are connected. The waveform of the output voltage is shown in the right side. It is a bi-polar rectangle wave with peak voltage $V+DC$ and $-V+DC$, and period T , where DC is the DC offset.

7.2 Experiment Setup in Electron-Beam Lithography

The experiments were conducted on a JEOL electron-beam exposure tool. The resist UVIIHS was coated on highly-doped wafers (the resistance is $<10\Omega$, hence the voltage drop across the substrate can be ignored) at 3000rpm for 30sec and prebaked at 140°C for 60sec. The exposure doses were 1.5, 3, 6, 9, 15, 20, 30 $\mu\text{C}/\text{cm}^2$ with beam currents 1, 5 and 10pA. The patterns of equal line/space (L/S) were exposed, the line/space widths were 100nm, 200nm, 300nm and 500nm, i.e., $L/S=100/100$, $200/200$, $300/300$, $500/500\text{nm}$. To exclude the environmental variations, we always loaded two chips into the exposure tool at the same time. Even though e-beam exposure has to be conducted in a sequential manner, the second chip was always exposed within 20 min after the first chip

was exposed. Since the exposures were conducted more than 2 hrs after tuning the exposure tool, it is believed that the beam current drift was minimal. The two chips were exposed with the same dose/beam current matrix.

One chip was randomly chosen for EFE-PEB and the other for standard PEB. The standard PEB conditions are: 140°C, 90sec. Two sets of EFE-PEB conditions were used: (1) 140°C, frequency 100kHz, 3.3V, 60sec, i.e., high-frequency, low-voltage mode. (2) 140°C, frequency 8kHz, 10V, 90sec, i.e., low-frequency, high-voltage mode.

The chips were developed in 0.263N tetramethylammoniumhydroxide(TMAH) for 60sec, in room temperature.

The 2-chip experiment was repeated 6 times and had good reproducibility.

7.3 Experiment Results and Analysis

In general, SEM pictures show T-topping taking place to some extent. This T-topping might be caused by several mechanisms. First, the samples were exposed in vacuum, some chemicals may outgas during the pumping process and cause surface retardation. Second, the highest electron dose is close to the substrate, the top part of the resist is exposed mainly by electron back scattering and may not receive enough dose[36]. Third, the environmental contamination may exist in SEM area.

The SEM pictures show that the EFE-PEB has noticeable effects on resist profile.

It was expected that EFE_PEB might increase the resist sensitivity. In the experiment, however, EFE-PEB's effect on sensitivity was not significant. All the patterns exposed at lower than $6\mu\text{C}/\text{cm}^2$ did not appear, and all the patterns exposed over $9\mu\text{C}/\text{cm}^2$ appeared. Some of the patterns exposed at $15\mu\text{C}/\text{cm}^2$ were over-exposed.

On the other hand, EFE-PEB can reduce the PEB time requirement. Figure 7-2 compares the line corners under EFE-PEB and standard PEB, respectively. In this sample, the EFE-PEB is 100kHz, 3.3V, 60sec. The line/space width is 500nm, dose $20\mu\text{C}/\text{cm}^2$. It can be seen that in EFE-PEB, the corner is more vertical, while in standard PEB, the corner forms a large radius profile with a rough edge and gradual taper down to the substrate.

Figure 7-3, 7-4, 7-5 and 7-6 compare the cross-sections of 0.1, 0.2 and $0.3\mu\text{m}$ L/S patterns under EFE-PEB and the standard PEB. The dose is $9\mu\text{C}/\text{cm}^2$. The EFE-PEB is 8kHz, 10V, 140°C , 90sec.

For $0.1\mu\text{m}$ L/S showed in Figure 7-3, the T-top effect was so severe that the top of the resist still remained while the underneath part of resist was washed away. The EFE-PEB, however, confined the lateral acid diffusion so more resist on top remained and formed a ‘comb’. In the standard PEB, the teeth of the ‘comb’ were deprotected and developed due to lateral acid diffusion[75].

For $0.2\mu\text{m}$ L/S shown in Figure 7-4, the standard PEB resulted in a very narrow resist foot which causes the collapse of resist lines, as is shown in Figure 7-4(b). The EFE-PEB lead to a thicker foot which was able to sustain the resist lines. This collapsed pattern is an example of over-exposure. The EFE-PEB has better tolerance of over-exposure because it confines the acid diffusion and reduces the extra lateral deprotection.

Figure 7-5 compares the $0.3\mu\text{m}$ L/S patterns. It can be seen that the EFE-PEB lead to much better resist profile, though the T-top effect still existed.

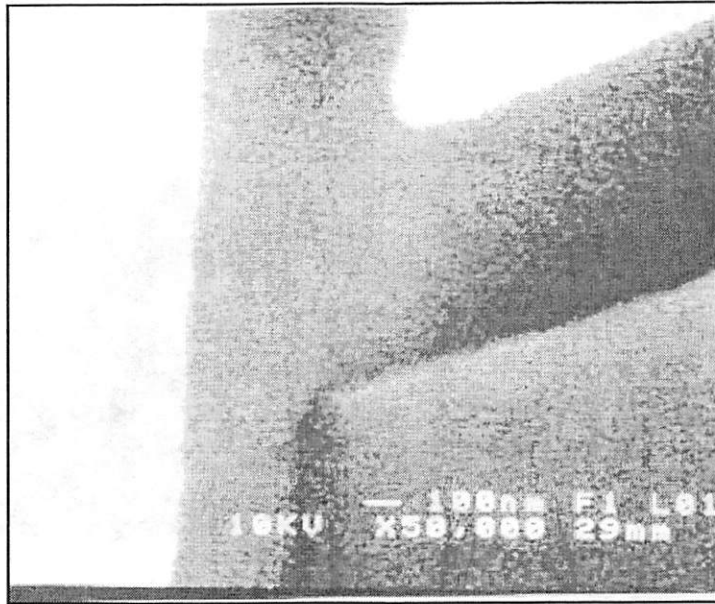
Figure 7-6 compares the $0.5\mu\text{m}$ L/S patterns, dose $15\mu\text{C}/\text{cm}^2$. Though the standard PEB and EFE-PEB lead to similar resist profile, EFE-PEB provided a better CD. In this sample, the design L/S is 500nm/500nm, standard PEB gave L/S=358nm/600nm, EFE-

PEB gave L/S=430nm/538nm. EFE-PEB reduced the lateral deprotection length by about 70nm.

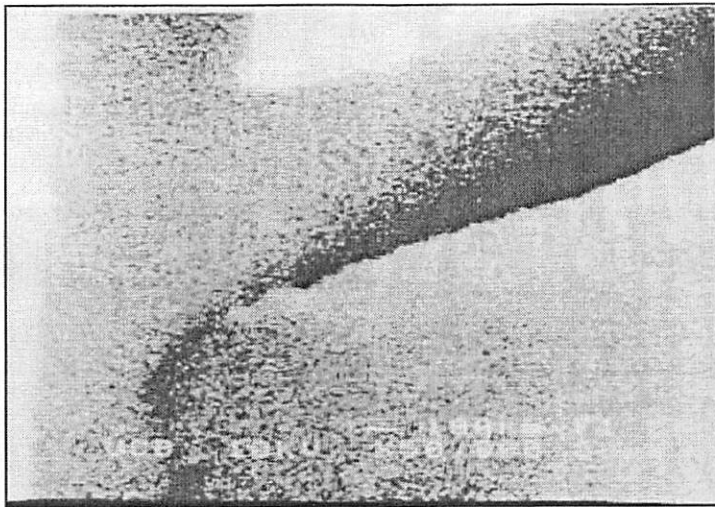
Table 7-1 shows the L/S values due to EFE-PEB and standard PEB. In all cases the remaining resist line was widened by at least 40nm.

Table 7-1 Line/Space values from EFE-PEB and standard PEB (unit: nm).

L/S on mask	L/S in standard PEB	L/S in EFE-PEB
300/300 (dose 15 μ C/cm ²)	190/483	267/434
300/300 (dose 9 μ C/cm ²)	215/388	253/332
500/500(dose 9 μ C/cm ²)	358/600	430/538



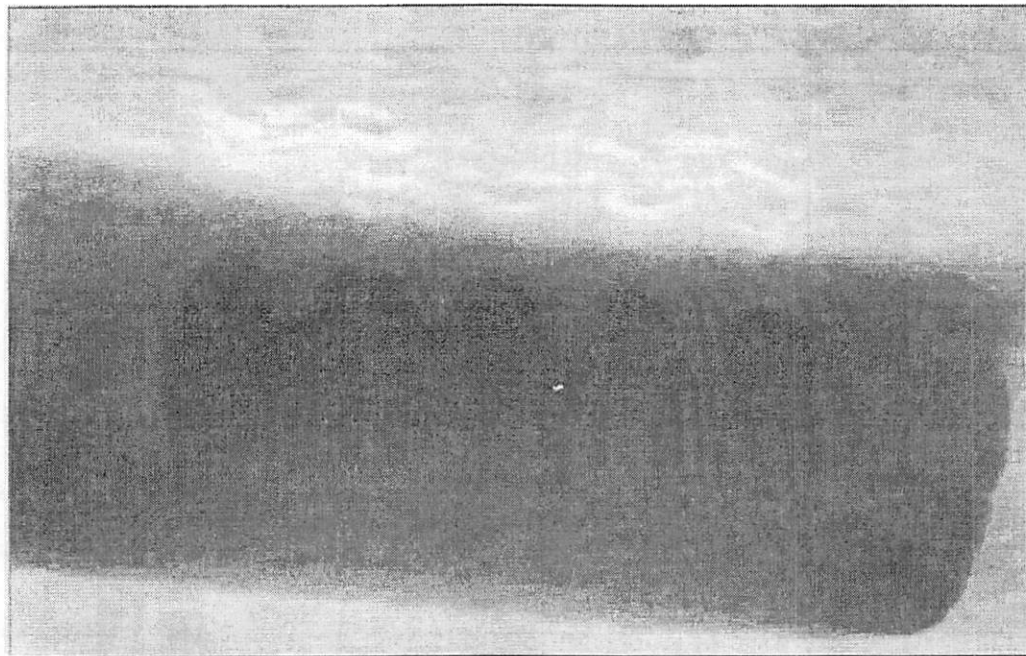
(a)



(b)

Figure 7-2 Comparison of EFE-PEB and Standard PEB for 0.5 μ m L/S, dose 20 μ C/cm².

(a) shows a line corner under EFE-PEB with 100kHz, 3.3V AC, 140°C, 60sec. (b), standard PEB 140°C, 90sec.



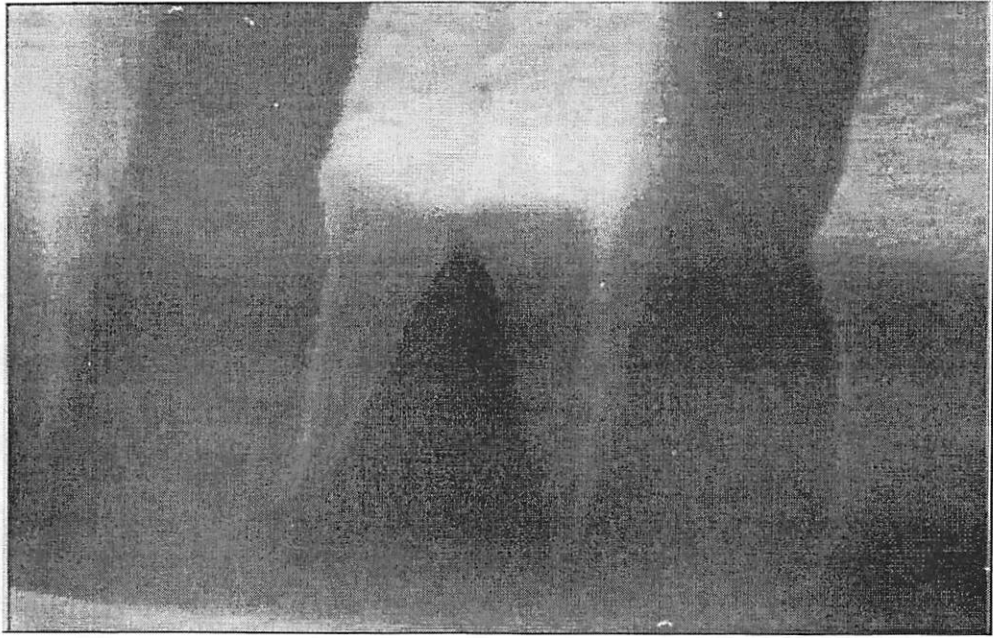
(a)



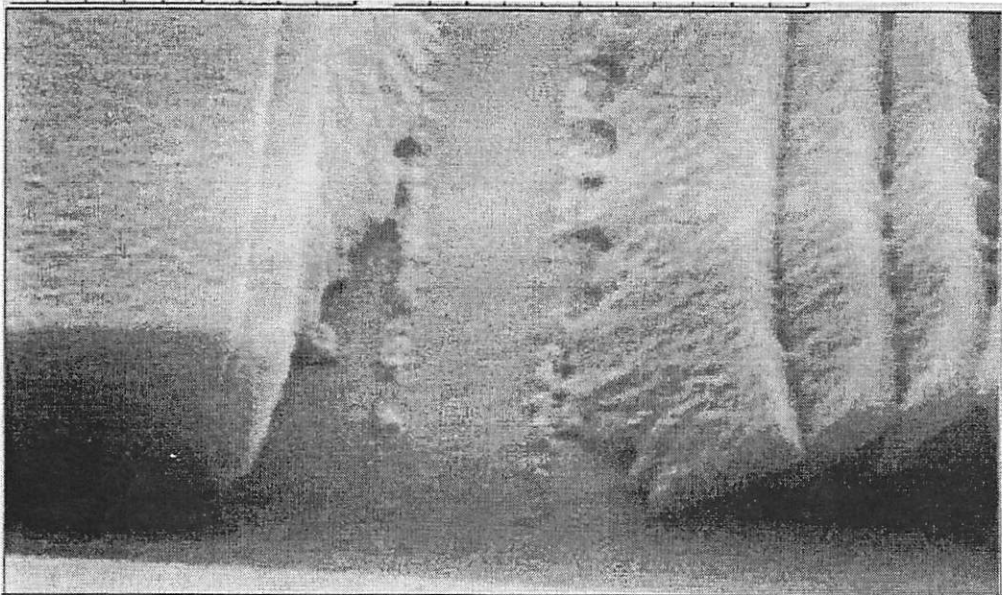
(b)

Figure 7-3 Comparison of EFE-PEB and Standard PEB for 0.1 μ m L/S, dose 9 μ C/cm².

Here (a) is EFE-PEB with 8kHz, 10V AC, 140°C, 90sec. (b), standard PEB 140°C, 90sec.



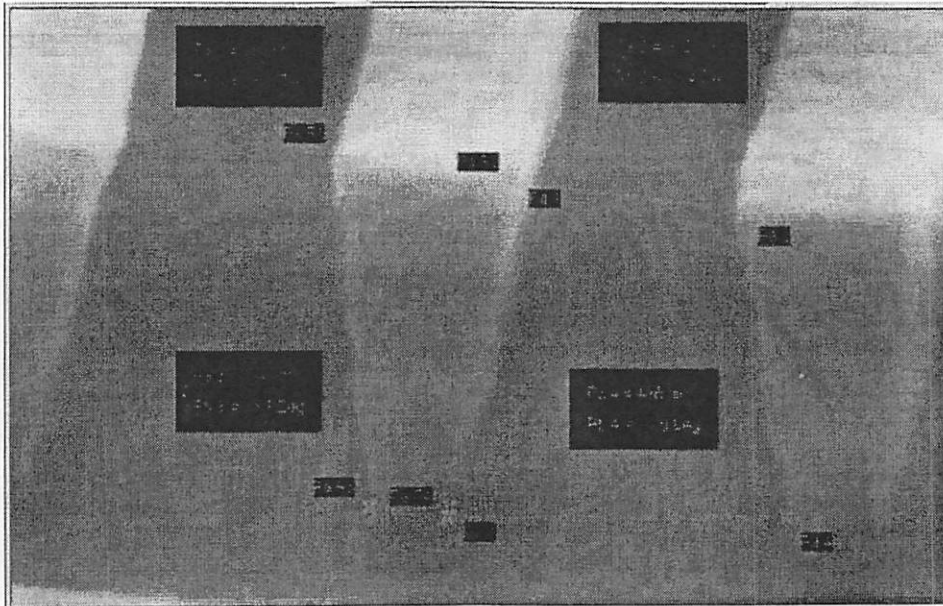
(a)



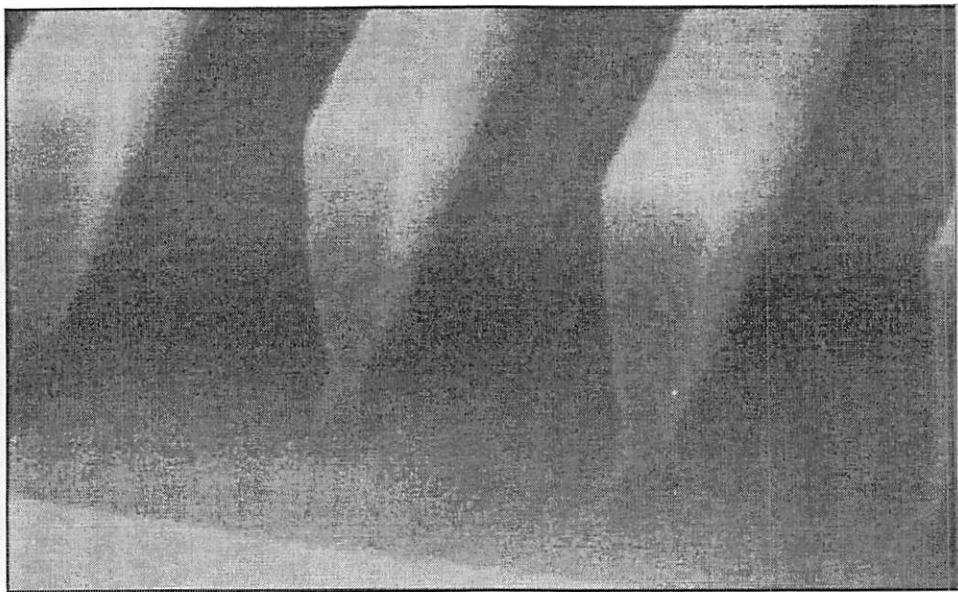
(b)

Figure 7-4 Comparison of EFE-PEB and Standard PEB for 0.2 μ m L/S, dose 9 μ C/cm².

(a) is EFE-PEB with 8kHz, 10V AC, 140°C, 90sec. (b), standard PEB 140°C, 90sec.



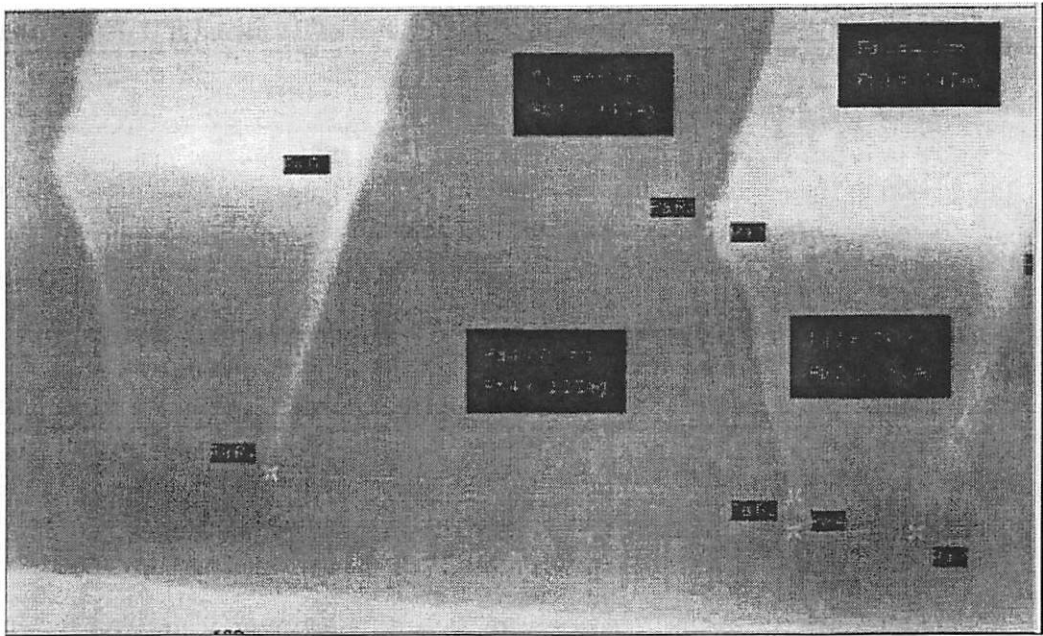
(a)



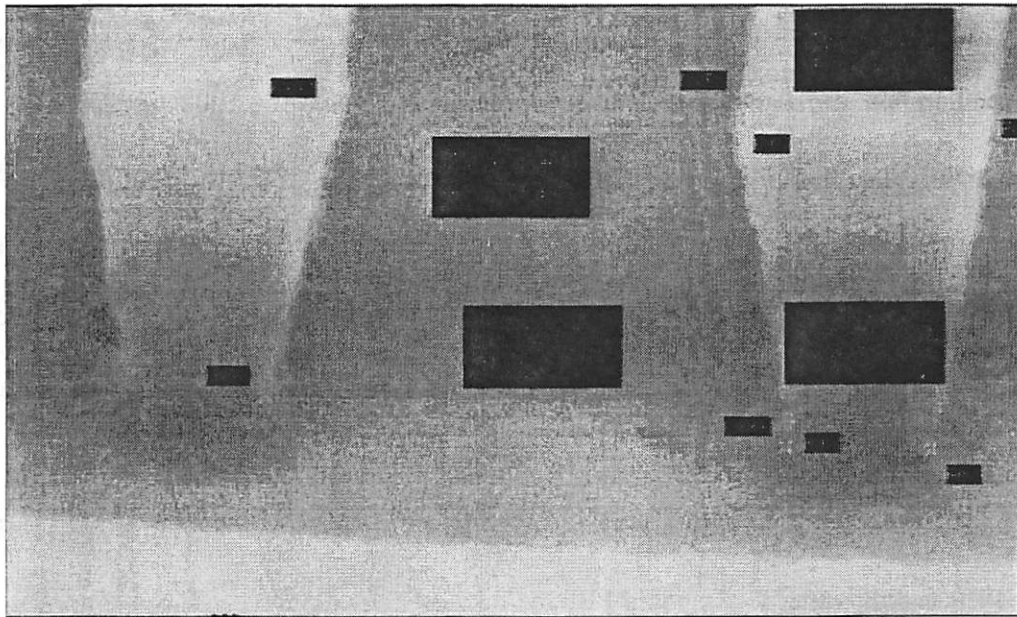
(b)

Figure 7-5 Comparison of EFE-PEB and standard PEB for 0.3 μ m L/S, dose 9 μ C/cm²

Here (a) is EFE-PEB with 8kHz, 10V AC, 140°C, 90sec. (b), standard PEB 140°C, 90sec.



(a)



(b)

Figure 7-6 Comparison of EFE-PEB and Standard PEB for 0.5 μm L/S, dose 15 $\mu\text{C}/\text{cm}^2$. Here (a) is EFE-PEB with 8kHz, 10V AC, 140°C, 90sec. (b), standard PEB 140°C, 90sec.

7.4 Experiments of the Impact of Field Polarity in Electron Beam

Lithography

In addition to the alternating field, the polarity of the direct field is also expected to affect the resist profile, because the DC field can drive the acid upward or downward and therefore redistributes the acid concentration. To demonstrate the impact of field polarity on resist, the experiments were conducted on a JEOL electron-beam exposure tool. The resist UVIHS was coated on highly-doped wafers (the resistance is $<10\Omega$, hence the voltage drop across the substrate can be ignored) at 3000rpm for 30sec and soft baked at 140°C for 60sec. The exposure doses were 7, 9, 12, 16 $\mu\text{C}/\text{cm}^2$ with beam currents 5 and 10pA. The patterns of equal line/space (L/S) and isolated space were exposed, and the line/space widths were 100nm, 200nm and 300nm, i.e., L/S=100/100, 200/200, 300/300nm. Similarly, the isolated space width were 100, 200 and 300nm, too. To exclude the environmental variations, we always loaded two chips into the exposure tool at the same time. Even though e-beam exposure has to be conducted in a sequential manner, the second chip was always exposed within 20 min after the first chip was exposed. Since the exposures were conducted more than 2 hrs after tuning the exposure tool, it is believed that the beam current drift was ignorable. Both chips were exposed with the same dose/beam current matrix. Then one chip was randomly chosen for EFE-PEB and the other for standard PEB.

The standard PEB conditions are: 140°C , 90sec. Two sets of EFE-PEB conditions were: 140°C , frequency 3Hz, DC 0.65V, AC 6.5V, 90sec, with the DC direction from the bottom to the top of the resist layer (upward) and from the top to the bottom of the resist layer (downward). Note that in standard PEB, the Al wafer was also placed on the resist

top to eliminate the thermal difference between standard PEB and EFE-PEB. Finally the chips were developed in 0.263N tetramethylammoniumhydroxide(TMAH) for 60sec at room temperature.

In both e-beam and DUV experiments that will be discussed in Section 7.6 and 7.7, a very important treatment of the Al wafer, which is the cathode, was to coat it with an insulating thin film. The film is made by spinning resist on the Al wafer and baking at 300°C for 10 min. Without this insulator, the H⁺ ion was found loss on the top, which is believed to be neutralized by obtaining an electron from Al in the anode. Being pressed by tweezers in PEB, the Al cathode has good contact with the resist film.

7.5 Experimental Results and Analysis

The process of UVIIHS resist is not optimized for e-beam lithography. Instead, the process is meant to be used for 248nm optical lithography. As is shown in Section 7.3, T-topping effects takes place to some extent in e-beam experiment, which is believed mainly due to e-beam dose distribution in resist. Thus an upward-DC is expected to improve UVIIHS resist profiles. The SEM pictures show that EFE-PEB has noticeably improved the resist profile.

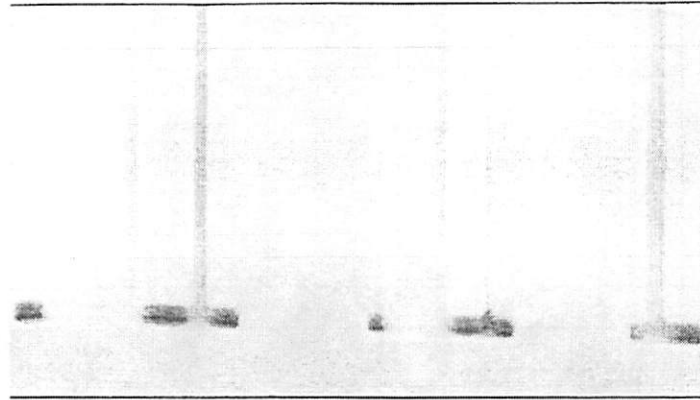
Figure 7-7 compares the tilted top-view of EFE-PEB with that of standard PEB. The dose is 12 μ C/cm². Under standard PEB, all the resist feet were undercut so severely that the lines were washed away. Under EFE-PEB with an upward DC, however, the acid was driven up without undercutting the lines so they still remained. On the other hand, the EFE-PEB with downward DC drove the acid down to the bottom of the resist, thus the T-

top effect was made even worse so that the top of the resist still remained while the underneath part of the resist was developed and a ‘comb’ was formed.

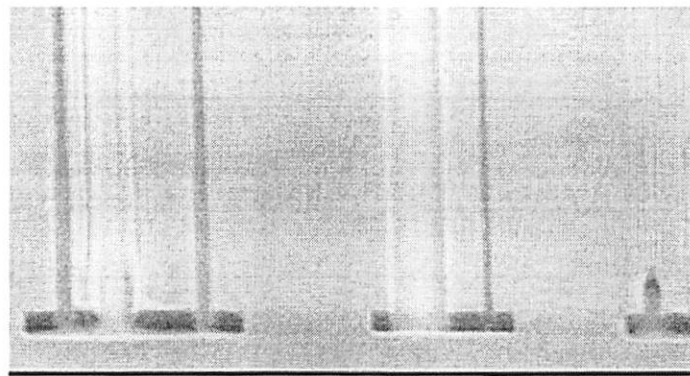
For 0.2 μm L/S shown in Figure 7-8, the standard PEB resulted in a very severe T-top effect such that a ‘comb’ was formed, as is shown in Figure 7 -8 (a). The EFE-PEB led to the development of resist surface to some extent and all the resist feet remained. This is a clear proof that the acid was driven to the top and implies that the EFE-PEB has better tolerance of under-exposure.

Figure 7-9 compares the 0.3 μm L/S patterns. It can be seen that the EFE-PEB lead to a much better resist profile, even though there is some bridging effect at the resist edge. On the contrary, the standard PEB eliminated all resist lines.

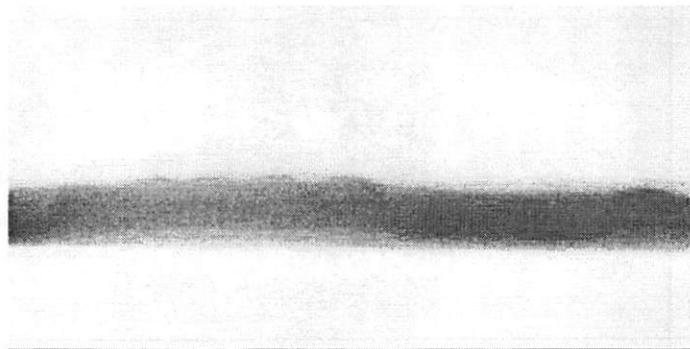
Figure 7-10 compares the 0.2 μm L/S patterns, dose 16 $\mu\text{C}/\text{cm}^2$, which is over-exposed. The upward EFE-PEB resulted in a clean sidewall. The downward EFE-PEB, however, resulted in a ‘roof’ at the resist edge, which indicates a worse T -top effect due to downward acid drift.



(a)



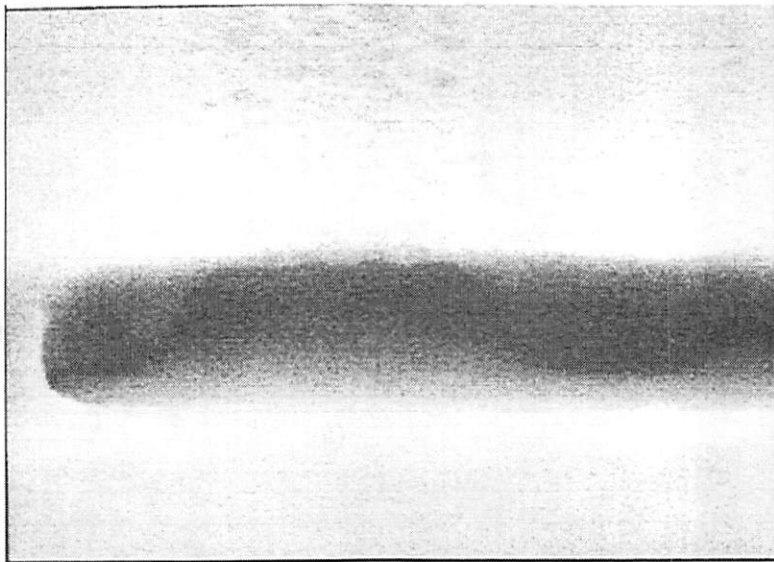
(b)



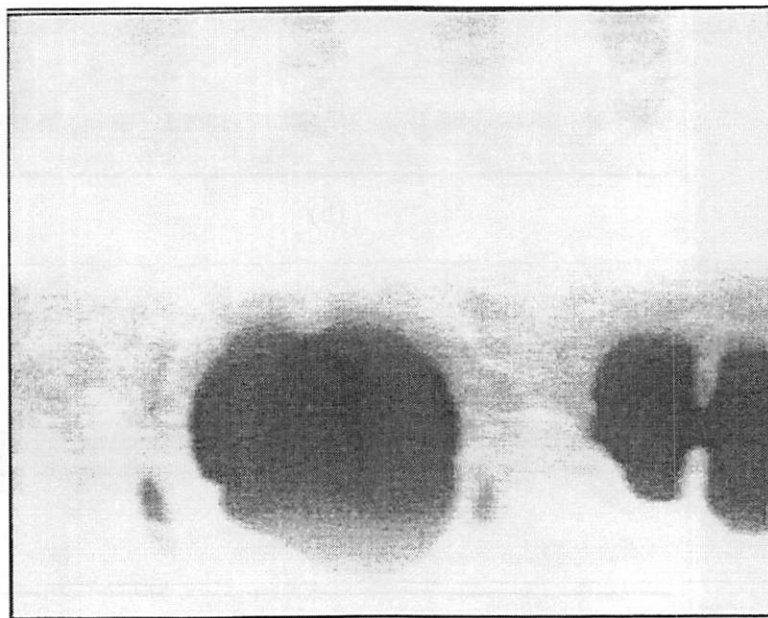
(c)

Figure 7-7 Comparison of upward/downward EFE-PEB and Standard PEB for 0.3, 0.2 and 0.1 μm L/S, dose $12\mu\text{C}/\text{cm}^2$.

Here (a) shows standard PEB. (b), EFE-PEB, DC upward. (c), EFE-PEB, DC downward, only 0.3 μm L/S is shown in (c).



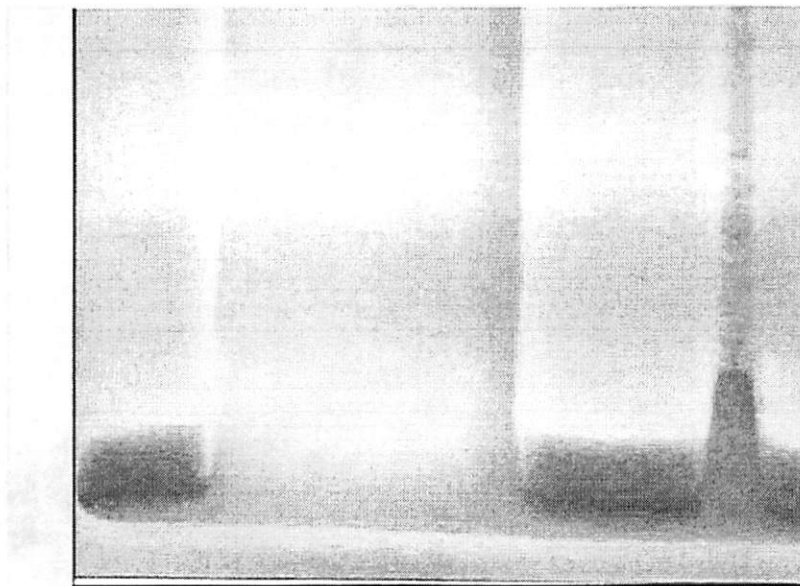
(a)



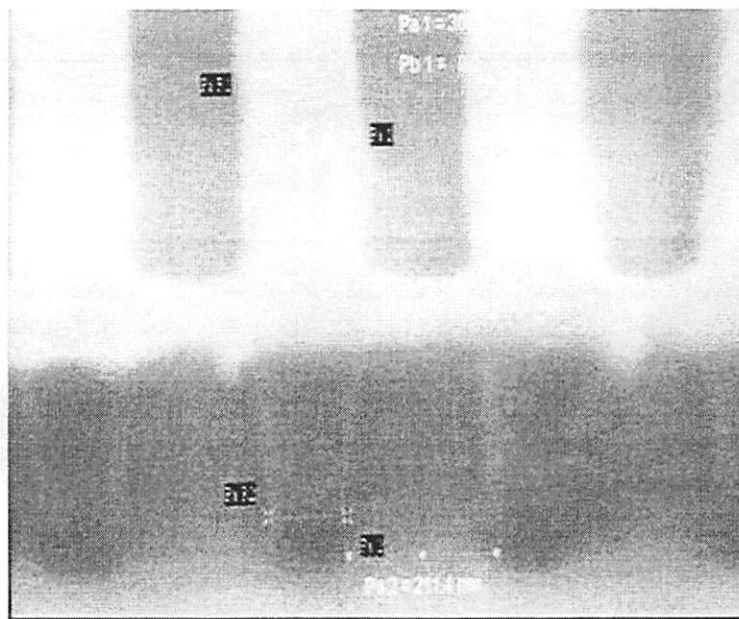
(b)

Figure 7-8 Comparison of EFE-PEB and Standard PEB for $0.2\mu\text{m}$ L/S, dose $9\mu\text{C}/\text{cm}^2$.

Here (a) is standard PEB, 140°C , 90sec. (b), EFE-PEB DC upward.



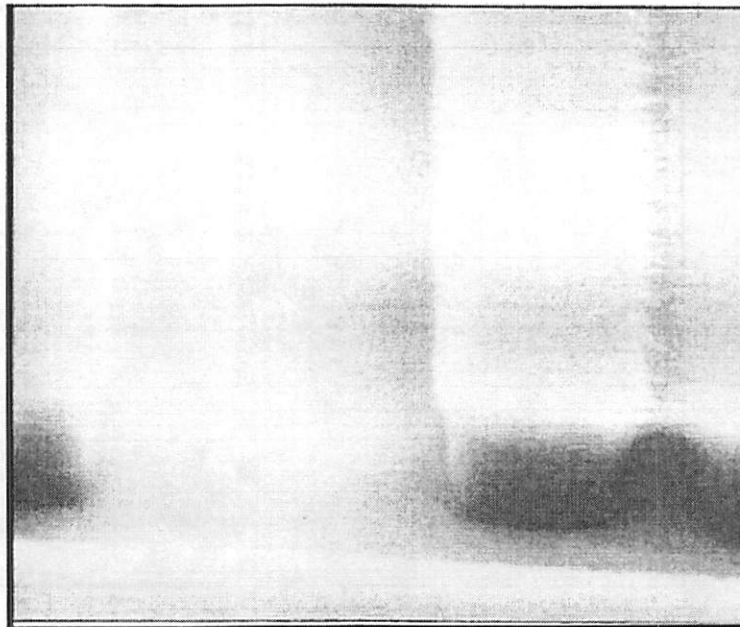
(a)



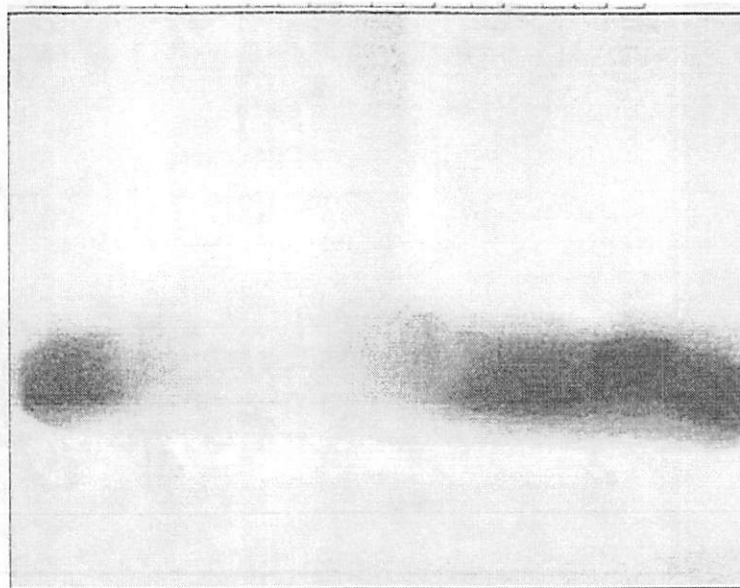
(b)

Figure 7-9 Comparison of EFE-PEB and Standard PEB for 0.3 μ m L/S, dose 9 μ C/cm².

Here (a) is standard PEB. (b), EFE-PEB, DC upward.



(a)



(b)

Figure 7-10 Comparison of EFE-PEB for $0.2\mu\text{m}$ L/S, dose $16\mu\text{C}/\text{cm}^2$.

Here (a) is EFE-PEB with 3Hz, 9.8V AC, 0.65V DC, upward. (b) is EFE-PEB with identical frequency and voltage, but DC downward.

7.6 Experiments in KrF Lithography

To demonstrate the impact of EFE-PEB in KrF lithography, a second set of experiments was done on an ASML KrF stepper. The resist UVII-10 was coated on 6-inch wafers. Though the wafers were not highly doped, their conductivity was much higher than that of the resist so that the voltage drop across the wafers could be neglected. The resist processing parameters are: spin 6000rpm for 30sec, soft bake 130°C for 90s. Exposure dose 27mJ/cm², NA 0.5, σ 0.2, Dense line/space with different pitches were exposed. Since the resist profiles at different pitches were consistent, only the data of L/S=400/400nm are presented in this thesis. On a 6-inch wafer, 26 dies of 2.1cm × 2.1cm were exposed with the identical dose of 27mJ/cm². During PEB, a 4-inch Al wafer was placed on the 6-inch wafer, covering half the dies. Thus half the dies were applied electrical field while the other half were on standard PEB. In EFE-PEB, the Al wafer was preheated to 130°C so that the thermal perturbation induced by Al wafer was diminished. By use of this approach, the EFE-PEB and standard PEB can be considered to have identical thermal histories.

The standard PEB is 130°C, 90s. Again, two sets of EFE-PEB were tested with frequency 2.5Hz, AC 6.5V, DC 6.5V, DC upward and DC downward. Finally the wafers were developed in 0.263N TMAH for 60sec at room temperature.

Note that the upper boundary conditions for standard PEB and EFE-PEB are different. For standard PEB, the top surface of resist is directly open to air, while in EFE-PEB, the surface of resist is covered by Al wafer. The difference in boundary conditions is expected to have some effects on the PEB chemistry. On one hand, the close boundary in EFE-PEB will block outgas of volatile group and make the protection/deprotection

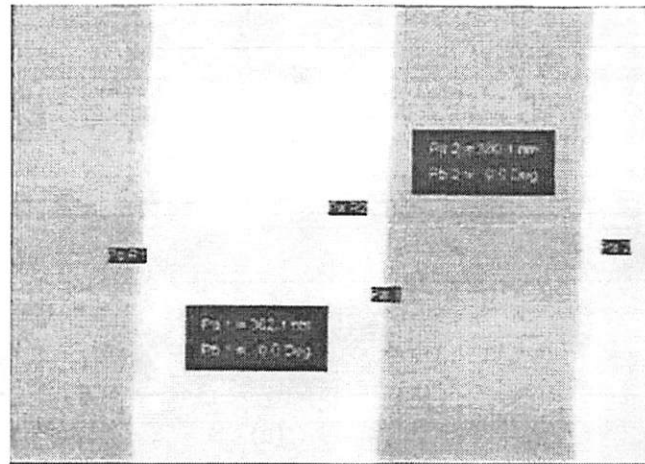
balance move to the direction of protection. Thus, the close boundary is expected to result in less deprotection than the open boundary in standard PEB. On the other hand, the close boundary means a second thermal source at the top, because the Al wafer was preheated to 130°C. This second thermal source will trigger more deprotection at the top compared with the open boundary, in which there exists only one thermal source at the bottom of resist. Since the resist chemistry was complicated by the different boundary conditions in standard and EFE-PEB, it is not fair to directly compare the resist profiles resulted from standard and EFE-PEB. However, by varying the polarity of the electric field and observing the resulted resist profiles, the impact of electric field on PEB can be deduced.

7.7 Experimental Results in KrF Lithography

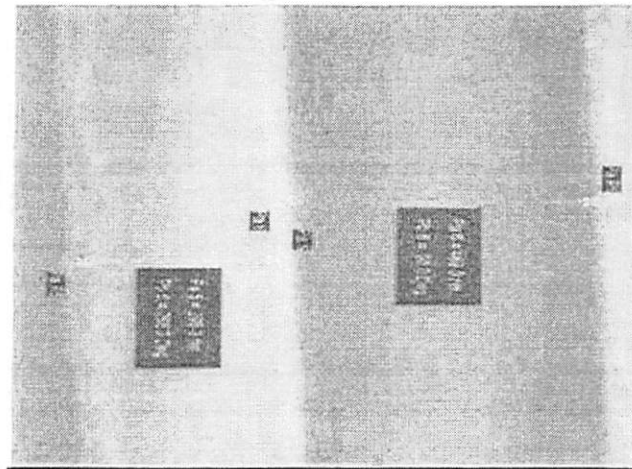
Figure 7-11 compares the L/S=400/400nm patterns obtained by KrF lithography. Both EFE-PEB and standard PEB lead to good resist patterns. Since no anti-reflective coating (ARC) was applied and σ is small, there exists a strong standing-wave effect on the resist sidewalls, indicated by the line edges. The AC/DC of EFE-PEB was not optimized to eliminate the standing-wave effect. However, the existence of the DC field lead to a better CD. Standard PEB gave L/S=295/469nm, while EFE-PEB gave L/S=362/380nm, reducing the lateral deprotection length by about 90nm.

Figure 7-12 compares the same patterns under standard PEB and upward EFE-PEB treatment. Since the acid at the bottom was driven away in the latter case, a narrower resist opening at the resist bottom is expected. This is confirmed by the SEM pictures, which show that the spacing at the resist bottom is 321nm in upward EFE-PEB while it is 395nm in standard PEB.

Since the downward and upward DC in EFE-PEB leads to different resist CDs on the top and at the bottom, it is clear that EFE-PEB has noticeable effect on resist profiles.



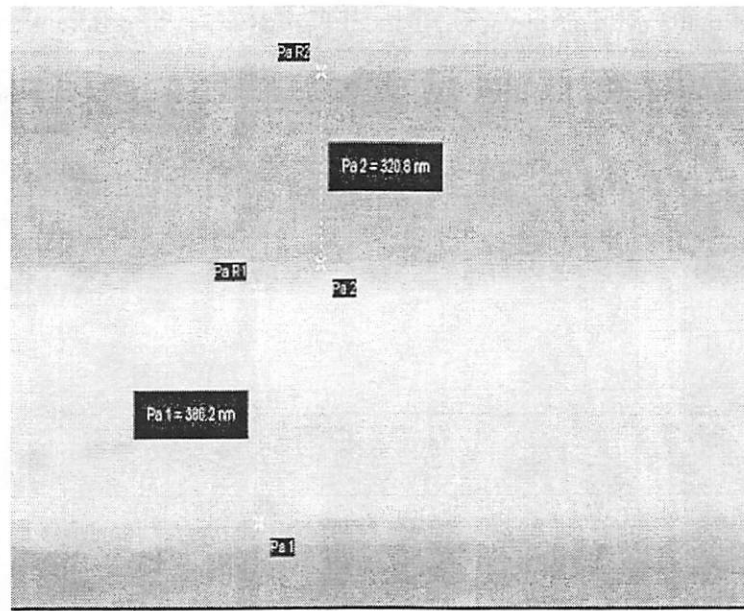
(a)



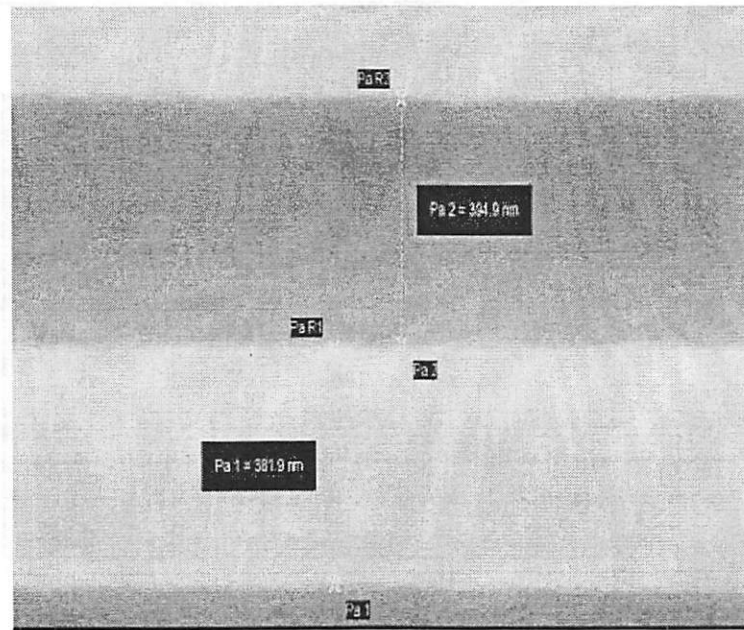
(b)

Figure 7-11 Comparison of EFE-PEB and Standard PEB in DUV lithography, 0.4 μ m L/S, dose 27mJ/cm².

Here (a) is EFE-PEB with 2.5Hz, 6.5AC, 6.5V DC downward. (b), standard PEB 130°C, 90sec.



(a)



(b)

Figure 7-12 Comparison of upward EFE-PEB and Standard PEB in DUV lithography, 0.4 μ m L/S, dose 27mJ/cm².

Here (a) is EFE-PEB with 2.5Hz, 6.5AC, 6.5V DC upward. (b), standard PEB 130°C, 90sec.

7.8 Conclusions

This chapter explored Electric-Field-Enhanced Post Exposure Bake, a methodology for enhancing the resist resolution and controlling resist profiles in electron-beam and KrF lithography based on confining the photoacid drift/diffusion by applying external electric field. Generally a high-voltage, low-frequency electric-field with a properly directed DC offset is desired to optimize the resist profile. And a short PEB time is also desired to optimize the resist profile. The electric-field enhanced PEB can reduce the PEB time requirement by 30%. Sharper corners were observed and the remaining resist lines were 40 to 70nm wider. The EFE-PEB treatment did not appear to improve the overall sensitivity. The reduced lateral diffusion/deprotection significantly improve the tolerance for over- and under-exposure and CD uniformity.

By controlling the polarity of the electric field, better vertical uniformities and clean resist sidewalls were observed and, in DUV lithography, the remaining resist lines were 70 to 90nm wider. The resist profiles can be aggressively controlled by adjusting the polarity, magnitude and frequency of the electric field. More experiments are expected to concept-prove the effectiveness of EFE-PEB in 157nm or EUV lithography. Furthermore, the optimum parameters of EFE-PEB can be derived from the mathematical model described in Chapter 6. Some experiments are expected to validate the optimization of EFE-PEB process.

8 Conclusions

8.1 Summary

This thesis addresses the problem of modeling and simulation useful for understanding factors responsible for various issues associated with the implementation of advanced lithography processes. Given the reduction in cost of computation and increase in cost of experimentation trend, the tools and methods will contribute to providing cost effective means of understanding physical aspects of processing steps to allow for process optimization.

Rigorous numerical algorithms and modeling approaches are described in this thesis to provide a general numerical framework for tackling complex models encountered in advanced optical lithography and identifying how process factors such as mask, lens and resist impact the lithographic resolution. A comprehensive model incorporating mask variation, lens imperfection and resist chemistry is absolute essential to understanding and balancing these process complexities for sub-200nm fabrication. This thesis initially discussed a methodology of modeling line-end shortening (LES) effects in KrF resists. SPLAT and STORM was linked to conduct optics and post exposure bake (PEB) simulation to obtain activated site concentration distribution, which directly determines dissolution rate. A threshold model was applied to calculate the pattern CDs. By fitting simulated CDs with experiment data, this methodology extracted the post exposure bake parameters and threshold activated site concentration. The method successfully predicted pattern CDs to RMS error within 10% of nominal linewidth. The method proved line-end shortening effects in 248nm resists resulted from both optical approximaty effects and

photoacid diffusion. In some high-diffusivity resists, for example, APEX-E, the PEB dominates the LES effects.

For KrF lithography, the imaging systems and resists are well developed. And simulation models have been proved very effective in predicting critical dimensions (CDs) and analyzing process factors. With ArF imaging technology rapidly maturing, the modeling of 193nm lithography becomes compellingly necessary for guiding manufacturing processes. The immaturity of ArF resists, however, presents formidable challenges to the modeling work. The main theme of this thesis is to develop a comprehensive modeling strategy so as to decompose the complexities of process factors involved in 193nm lithography.

The computational time complexity of PEB simulation is a main bottle neck for modeling lithography systems. This thesis presents a very fast algorithm for simulating coupled physical/chemical processes described by non-linear partial differential equation (PDE) systems. On the basis of Finite Difference Method (FDM), the algorithm uses high order partial differential expansion to represent unknown functions in PDE so that a time step 100 times larger than the conventional FDM is achieved during the simulation. For chemically amplified resist simulation, this algorithm is more than 10 times faster than conventional simulators using the Finite Element Method (FEM). Thus it enables the practical use of PEB simulation of Chemically Amplified Resists (CARs). The algorithm was implemented in a simulator named RIAR, standing for Rapid Imaging Algorithm for Resist. With the fast simulation capability of RIAR, the simulation of lithography process is essentially no longer a limiting factor. The main hinder of modeling 193nm lithography is believed to be developing and calibrating scalable and predictive models.

To effectively calibrate resist models and address the 2-dimensional effects such as corner rounding and bridging, an image processing algorithm which retrieves the physically fine contours of patterns from noisy SEM pictures, and then computes the difference of the extracted contours with those simulated by a given model. By fine tuning the parameters to minimize the difference between experimental and simulated contours, the model parameters can be effectively and efficiently extracted. This approach enables 2-dimensional calibration of lithography models, which is essential to modeling the printing of deep-100nm random logic devices.

Based on the fast PEB simulation algorithm and the image matching method, a systematic divide-and-conquer strategy was developed to identify the main process factors individually. The main factors affecting printing quality include mask accuracy, choice of imaging focal plane, lens aberrations, resist PEB process and resist dissolution mechanism. The actual mask CDs were measured and used in all simulations, which excludes the mask error effect. Comparing the mask CDs and wafer CDs, it is found that the unexpected isolated-dense line bias is mostly determined by mask CD variations and Mask Error Factor (MEF). Then by inspecting the CD vs. defocus curves of isolated and dense lines, the location of focal plane in the resist was determined. After adding lens aberrations, it was found that the actual focal plane location was 0.1mm lower than calculated under the assumption of aberration-free lens. The error of simulated CDs is reduced by 15% after including lens aberrations. It proves the importance of including lens aberrations in models, because they affect the choice of best focal plane significantly. Using the measured mask CDs, lens aberrations and the imaging location found above, the light intensity in resist of lines over full defocus-pitch-linewidth matrix

were simulated. A threshold light intensity model was used to determine the line CDs. The Root Mean Square (RMS) value of the simulation error was 5.26nm, or 5% of the smallest line width. Thus this single-threshold model proved adequate in predicting line CDs over full defocus-pitch-linewidth matrix.

The calibrated single-threshold resist imaging model was further used to simulate 2-dimensional patterns. The simulated images conform the experimental SEM pictures very well and the mismatched area is generally less than 15% of the pattern area. However, the line-end gaps predicted by this model were much larger than experimental. PEB and dissolution models were tested to identify the impact of these two resist processes separately. A PEB model in which the acid diffusivity, the deprotection rate constant and the threshold activated site concentration were tuned reduced RMS error of line-end gap prediction to 37nm at the cost of increasing linewidth prediction error from 5% to 27%. This indicates the large dissimilarity between line and gap behaviors is mostly not due to PEB. A trajectory dissolution model was developed in which the dissolvability of resist at a certain location is influenced by the neighboring peak light intensity. While keeping the error of line width simulation within 6nm, the dissolution model reduces the error of predicting gaps to 26nm over full doses-defocus matrix. The residual error may be due to the incompleteness of assumed trajectory dissolution simulation.

This thesis also investigates a novel resist processing technique named ‘electric-field-enhanced post exposure bake’, which uses alternating electric field to aggressively modify or control the profile of photoresist. The resist material becomes soluble in reactions catalyzed by protons generated by exposure. In this process, the presence of an alternating field leads to an order of magnitude greater arc length of the proton in the

preferred direction than in the unwanted lateral directions. A mathematical theory was presented and explained the necessities of alternating field. In experiments a resist profile improvement effect was clearly observed, which provided evidence for patent application. The method can significantly improve the resist resolution. More importantly, it provides a promising solution to the problem of lack of single layer resist facing 157nm and Extreme Ultraviolet (EUV) lithography. With this method, current commercial deep-UV resists could be used in 157nm and EUV lithography with little modification. A patent of this invention was filed by University of California on July 18, 2001.

8.2 Improvements and Extensions of Lithography Modeling

Rigorous simulation in lithography requires simulation capabilities of 3-dimensional effects. Optical lithography issues such as reflective notching, line end shortening, resist footing and T-topping require 3-dimensional simulators to capture their effects. Until the recent advances in numerical algorithms documented in the thesis of E. Croffie [10], rigorous 3-dimensional simulation of PEB effects using mechanistic based physical models presented a big challenge as these simulators took days due to the large increase in the number of nodes representing the 3-dimensional domain. With the algorithms presented in [10] and this thesis, 3-dimensional simulations are now practical. The RIAR algorithm can be further extended to 3D, which is believed to be able to generate more insights on resist processes. Combining this reaction/diffusion simulation with 3D dissolution model ought to be essential to modeling the low contrast 193nm resist in current use.

Bibliography

- [1] J. Lorenz, J. Pelka, H. Ryssel, A. Sachs, A. Seidl, and M. Svoboda, 'COMPOSITE, A Complete Modeling Program of Silicon Technology', IEEE Trans. Computer- Aided Design of Integrated Circuits and Systems. vol. CAD-4, no. 4, pp. 421-430, April 1985.
- [2] W. G. Oldham, S. N. Nandgaonkar, A. R. Neureuther, and M. M. O'Toole, 'A General Simulator for VLSI Lithography and Etching Process: Part I - Applications to Projection Lithography,' IEEE Trans. Electron Devices, vol. ED-26, no. 4, pp. 717-722 (1979).
- [3] Technology Modeling Associates, DEPECT-2, Technology Modeling Associates, 1990.
- [4] C. A. Mack, 'PROLITH: A Comprehensive Optical Lithography Model,' Proc. of SPIE, vol. 538, pp. 207-220 (1985).
- [5] W. Henke, D. Mewes, M. Weiss, G. Czech, and R. Schiessl-Hoyler, 'Simulation of Defects in 3-Dimensional Resist Profiles in Optical Lithography,' Microelectronic Engineering, vol. 13, pp. 497-501 (1991).
- [6] M. E. Law and R. W. Dutton, 'Verification of Analytic Point Defect Models Using SUPREM-IV,' IEEE Trans. CAD, vol. 7, pp. 181 -190 (1988).
- [7] User' s Guide for SPLAT version 5.0, UC Berkeley, ERL
- [8] Helmsen, J. J, Yeung, M.; Lee, D., Neureuther, A.R, 'SAMPLE -3D benchmarks including high NA and thin film effects', Proc. of the SPIE, vol.2197, (Optical/Laser Microlithography VII, San Jose, CA, USA, 2-4 March 1994.) 1994. p.478-88

- [9] M. Zuniga, 'Fundamental Mechanisms in Advanced Resist System in Optical Lithography', Ph.D. Thesis, University of California, Berkeley, May 1999.
- [10] E. Croffie, PhD thesis, UC Berkeley, 2001
- [11] Croffie, E.; Cheng, M; Neureuther, A.; Cirelli, R.; Houlihan, F.; Sweeney, J.; Watson, P.; Nalamasu, O.; Rushkin, I.; Dimov, O.; Gabor, "A. Overview of the STORM program application to 193 nm single layer resists", *Microelectronic Engineering*, vol.53, (no.1-4), pp 437-42
- [12] Vanderplaats, G. N., 'Numerical Optimization Techniques for Engineering Design', McGraw Hill, New York, 1984
- [13] M. A. Zuniga, G. Wallraff, E. Tomacruz, A.R. Neureuther, J. Vac Sci. Technol B. 1, 2862 (1993).
- [14] Mosong Cheng; Croffie, E.; Neureuther, A., 'Fast imaging algorithm for simulating pattern transfer in deep-UV resist and extracting post exposure bake parameters', Proceedings of the SPIE vol.3999, pt.1-2, (Advances in Resist Technology and Processing XVII, Santa Clara, CA, USA, 28 Feb.-1 March 2000.) pp. 854-64
- [15] Kudo, T.; Dammel, R.R.; Jun-Bom Bae; Rahman, M.D.; Woo-Kyu Kim; McKenzie, D.; Aemy, E.L.; Ng, W.; Padmanaban, M., 'Mechanistic studies on the CD degradation of 193 nm resists during SEM inspection', *Journal of Photopolymer Science and Technology*, vol.14, (no.3), Tech. Assoc. Photopolymers 2001. pp 407-17

- [16] Terry, M.; Smith, A.H.; Rebitz, K. "Gauging the performance of an in-situ interferometer", Proceedings of the SPIE, vol.4000, pt.1-2, (Optical Microlithography XIII, Santa Clara, CA, USA, 1-3 March 2000.) pp.1223-36
- [17] Malyan, B.; Balachandran, W. "Sub-micron sized biological particle manipulation and characterization", Journal of Electrostatics, vol.51-52, May 2001. pp 15-19
- [18] Sagues, F.; Lopez-Salvans, M.Q.; Claret, J. "Growth and forms in quasi-two-dimensional electrocrystallization", Physics Reports, vol.337, (no.1-2), Elsevier, Oct. 2000. pp 97-115.
- [19] Brodsky, C.; Byers, J.; Conley, W.; Hung, R.; Yamada, S.; Patterson, K.; Somervell, M.; Trinque, B.; Tran, H.V.; Sungseo Cho; Chiba, T.; Shang-Ho Lin; Jamieson, A.; Johnson, H.; Heyden, T.V.; Willson, C.G. "157 nm resist materials: Progress report", Journal of Vacuum Science & Technology B (Microelectronics and Nanometer Structures), vol.18, (no.6) Nov. 2000, pp 3396-401
- [20] T A. Brunner, Proc. of SPIE, Vol. 2726, pp 198-207, 1996
- [21] C A. Mack, "Line end shortening (lithography)", Microlithography World, Vol. 9, (No. 2), Spring 2000
- [22] J. Byers, Proc. SPIE, Vol. 2724, pp 156-162, 1996
- [23] M. Zuniga et al, J. Vac. Sci. Tech. B, Dec 1995 (2957)
- [24] E. Croffie et al, SPIE Vol. 3678, 1999
- [25] M. Cheng et al, SPIE Vol. 3999, pp. 854-864, 2000
- [26] F. H. Dill, "Optical Lithography", IEEE Trans. Electron Devices, ED -22, No. 7 (1975) pp.440-444.

- [27] F. H. Dill, W.P. Hornberger, P.S. Hauge, and J.M. Shaw, 'Characterization of Positive Photoresist', IEEE Trans. Electron Devices, ED-22, No. 7 (July, 1975) pp.445-452.
- [28] F.H. Dill, A.R.Neureuther, J.A. Tuttle, and E.J. Walker, 'Modeling Projection Printing of Positive Photoresists', IEEE Trans. Electron Devices, ED-22, No. 7 (1975) pp.456-464.
- [29] Zuniga, M, Neureuther, A., 'Post Exposure Bake Characterization and Parameter Extraction for Positive Deep-UV Resists through Broad Area Exposure Experiments', Proc. of the SPIE, Vol. 2724, 1996.
- [30] Zuniga, M., Neureuther, A., 'Reaction Diffusion Modeling and Simulation in Positive Deep Ultraviolet Resists', J. Vac. Sci. Tech. B, Dec 95 (2957).
- [31] Yeung, M.S.; Barouch, E. 'Use of rigorous three -dimensional electromagnetic simulation to evaluate the effectiveness of optical proximity correction for nonplanar lithography', Semiconductor Process and Device Performance Modelling. Symposium, Boston, MA, USA, 2-3 Dec. 1997. Warrendale, PA, USA: Mater. Res. Soc, 1998. p.173-9
- [32] C. A. Mack, 'Inside PROLITH: A Comprehensive Guide to Optical Lithography Simulation', FINLE Technologies, Austin, TX
- [33] Roberts, B.; Gould, C.; Smith, A.; Rebitz, K. 'Pattern placement errors: application of in-situ interferometer determined Zernike coefficients in determining printed image deviations', Proc. of SPIE vol.4181 (2000), pp25-32

- [34] Liao, H.; Palmer, S.R.; Sadra, K. "Variable -threshold optical proximity correction (OPC) models for high-performance 0.18- μm process", Proceedings of the SPIE vol.4000, pt.1-2, pp.1033-40
- [35] Cobb, N.; Zakhor, A.; Reihani, M.; Jahansooz, F.; Raghavan, V. "Experimental results on optical proximity correction with variable threshold resist model", Proceedings of the SPIE vol.3051, pp 458-68
- [36] B. Mortini et al, J. Vac Sci Tech. B, 15, 2534(1997)
- [37] M. Zuniga et al, Proc. SPIE 2724(1996)
- [38] Lo, C.W. et al., J. of Vac Sci & Tech B, vol.13, no.3, May-June 1995
- [39] Croffie, E.; Mosong Cheng; Neureuther, A. "Moving boundary transport model for acid diffusion in chemically amplified resists", Journal of Vacuum Science & Technology B (Microelectronics and Nanometer Structures), vol.17, (no.6) p3339-44
- [40] Croffie, E.; Cheng, M.; Zuniga, M.; Neureuther, A. "Efficient simulation of post-exposure bake processes in STORM", Proceedings of SPIE vol.3678, pt.1-2 1999, pp 1227-34.
- [41] M. de Berg ... et al., "Computational geometry: algorithms and applications", Berlin ; New York : Springer, c1997.
- [42] J. Crank et al, Diffusion in Polymers (Academic, London, 1987)
- [43] M. Cheng et al, Proc. SPIE, 3678(1999)
- [44] Capodici, L.; Torres, J.A.; Socha, R.; Hollerbach, U.; Chen, J.F.; van Os, C.; Granik, Y.; Toublan, O.; Cobb, N, "Effects of advanced illumination schemes on design manufacturability and interactions with optical proximity corrections", Proceedings of the SPIE vol.4181 pp.58-67

- [45] Jiangwei Li et al., 'Model based optical proximity correction including effects of photoresist processes', Proceedings of the SPIE vol.3051, p.643-51
- [46] C. R. Szmanda, R. Kavanagh, J. Bohland, J. Cameron, P. Trefonal, R. Blacksmith, Proc. SPIE, Vol 3678, 857-866, (1999).
- [47] Jae Lim, 'Two -Dimensional Signal and Image Processing', Prentice Hall, 1990
- [48] Donald Hearn and M. Baker, 'Computer Graphics', 2nd Ed., Prentice Hall, 1994
- [49] J.E. Dennis, Jr., Robert B. Schnabel. Englewood Cliffs, N.J., 'Numerical methods for unconstrained optimization and nonlinear equations', Prentice-Hall, c1983
- [50] Okoroanyanwu, Uet al, 'Integration considerations for 130 nm device patterning using ArF lithography', Proc. of the SPIE vol.4000, pp 423-34
- [51] Chang-Nam Ahn; Hee-Bom Kim; Ki-Ho Baik, 'Exposure latitude analysis for dense line and space patterns by using diffused aerial image model', Proc. of SPIE vol.4000, pp 665-75
- [52] Hong, J.-S.; Kim, H.-B.; Yune, H.-S.; Ahn, C.-N.; Koo, Y.-M.; Baik, K.-H. "Accuracy of diffused aerial image model for full-chip-level optical proximity correction", Proc, of SPIE vol.4000, pp 1024-32
- [53] J. Thackeray, M. Denison, T. Fedynyshyn, D. Kang, R. Sinta, Proc. Acs Symp. Ser., 614, 110, (1995).
- [54] Keeho Kim, private communications
- [55] Qizhi He; Mi-Chang Chang; Palmer, S.; Sadra, K., 'OPC methodology and implementation to prototyping of small SRAM cells of 0.18 mu m node logic gate levels', Proceedings of the SPIE vol.4000, pp 90-8

- [56] Maenhoudt, M.; Verhaegen, S.; Ronse, K.; Zandbergen, P.; Muzio, E. 'Limits of optical lithography', Proceedings of the SPIE vol. 4000, pp.373-87.
- [57] Kroyan, A.; Watson, G.P.; Cirelli, R.A.; Nalamasu, O.; Tittel, F.K, 'Effects of sub-resolution assist features on depth of focus and uniformity of contact windows for 193 μm lithography', Proceedings of the SPIE vol.3679 (1999), pp 630-8
- [58] Mack, C.A. 'Corner rounding and line-end shortening in optical lithography', Proceedings of the SPIE vol.4226 (2000), pp 83-92
- [59] M. Cheng, and A. Neureuther, "ArF imaging modeling by using resist simulation and pattern matching", Proc of SPIE, Optical Microlithography XIV, 2001
- [60] Maurer, W.; Dolainsky, C.; Thiele, J.; Friedrich, C.; Karakatsanis, P. 'Process proximity correction using an automated software tool', Proceedings of the SPIE vol. 3334, (1998), pp 245-53
- [61] Shane Palmer, Private Communications
- [62] C. A. Mack, 'Development of Positive Photoresist', J. Electrochemical Soc., Vol. 134, No. 1, pp 148-152
- [63] C. A. Mack, 'New Kinetic Model for Resist Dissolution', J. Electrochemical Soc., Vol. 139, No. 4, pp. 135-137
- [64] Viovy, J.-L. 'Electrophoresis of DNA and other polyelectrolytes: Physical mechanisms', Reviews of Modern Physics, vol.72, (no.3) July 2000. pp. 813-72
- [65] Hughes, M.P. "AC electrokinetics: applications for nanotechnology", Nanotechnology, vol.11, (no.2), June 2000. pp.124-32.

- [66] Hinsberg, W.; Hoffnagle, J.; Houle, F. 'Chemistry and physics of the PEB process in a CA resist', *Solid State Technology*, vol.43, (no.8), PennWell Publishing, Aug. 2000. p.95-6, 98, 100, 102
- [67] Miyake, Y.; Isono, M.; Sekiguchi, "A. Study of deprotection reaction during exposure in chemically amplified resists for lithography simulation", *Journal of Photopolymer Science and Technology*, vol.14, (no.3), Tech. Assoc. Photopolymers, 2001. pp 463-7.
- [68] Pain, L.; Scarfogliere, B.; Tedesco, S.; Gourgon, C.; Coulomb, J.P.; Morin, M.; Ribeiro, M, 'Reduction of post exposure delay time and contamination sensitivity in chemically amplified resists: Application for lithography using off-line environment', *Microelectronic Engineering*, vol.57-58, Sept. 2001. pp 511-16
- [69] Hansen, S.G, 'Examination of the relationships between photoresist dissolution and diffusion characteristics, lithographic predictors, and simulated lithographic performance', *Proceedings of the SPIE* vol.3999, pp. 899 -909
- [70] Croffie, E.; Mosong Cheng; Neureuther, A, 'Moving boundary transport model for acid diffusion in chemically amplified resists', *Journal of Vacuum Science & Technology B (Microelectronics and Nanometer Structures)*, vol.17, (no.6), Nov. 1999. p.3339-44
- [71] Akira Tokui et al, US Patent 5,158,861 and US Patent 5,258,266
- [72] Thackeray, J.; Fedynyshyn, T.H.; Kang, D.; Rajaratnam, M.M.; Wallraff, G.; Opitz, J.; Hofer, D. 'Correlation of UVIIHS resist chemistry to dissolution rate measurements', *Journal of Vacuum Science & Technology B (Microelectronics and Nanometer Structures)*, vol.14, (no.6), Nov.-Dec. 1996. p.4267-71

- [73] Pain, L.; Le Cornec, C.; Rosilio, C.; Paniez, P.J. 'Free volume variations during exposure and PEB of DUV positive resists: Effect on dissolution properties', Proceedings of the SPIE vol.2724 (1996), p.100-9
- [74] Tegou, E., 'Surface silylation chemistry and process issues', Journal of Photopolymer Science and Technology, vol.14, (no.3), Tech. Assoc. Photopolymers, 2001. p.495-502
- [75] M. Cheng et al, J. Vac Sci Tech. 18(6), Nov/Dec 2000
- [76] A. R. Eckert, W.M. Moreau, 'Fluorescence detection of photoacid in chemically amplified resists', Proc. SPIE-Int. Soc. Opt. Eng., (1997), 3049, 879-887.
- [77] U. Okoroanyanwu, J.D. Byers, T. Cao, S. E. Webber, C.G. Willson, 'Monitoring photoacid generation in chemically amplified resist systems,': Proc. SPIE-Int. Soc. Opt. Eng., (1998), 3333, 747-757.
- [78] G. Pohlars, J.C. Scaiano, R. Sinta, "A novel Photometric Method for the Determination of Photoacid Generation Efficiencies Using Benzothiazole and Xanthene Dyes as Acid Sensors", Chem. Mater. (1997) 9(12) 3222-3230,
- [79] J. Byers, J. Petersen, J. Sturtevant, 'Calibration fo Chemically Amplified Resist Models', Proc. SPIE-Int. Soc. Opt. Eng., (1996), 2724, 156-162.
- [80] C.G. Willson, H. Ito, J. Frechet, T. Tessier, and F. Houlihan, "Approaches to the Design of Radiation-Sensitive Polymeric Imaging Systems with Improves sensitivity and Resolution," J. Electrochem Soc., vol. 133, no. 1, pp181-187, 1986.
- [81] T.H. Fedynyshyn, J.W. Thackeray, J.H. Georger, M.D. Denison, J. Vac. Sci. Tech. B 3888 (1994).
- [82] D. Seligson, S. Das, H. Gaw, P. Pianetta, J. Vac. Sci. Technol B 6 2303, 1998.

- [83] H. Fukuda, S. Okazaki, 'Kinetic Model and Simulation for Chemical Amplification Resists,' J. Electrochem. Soc., vol. 137, no. 2, pp. 675-679, 1990.
- [84] T. Watanabe, Y. Yamashita, J. Vac. Sci. Technol. B 12(6) 3879 (1994)
- [85] R. Ferguson, J.M. Hutchinson, C.A. Spence, A.R. Neureuther, J. Vac. Sci. Technol. B 8(6) 1423 (1990).
- [86] R.A. Ferguson, 'Modeling and Simulation of Reaction Kinetics in Advanced Resist Processes for Optical Lithography', Ph.D. Thesis, Memorandum No. UCB/ERL M91/78, University of California, Berkeley, September 1991.
- [87] G.M. Wallraff, J.M. Hutchinson, W. Hinsberg, F. Houle, P. Seidel, R. Johnson, J. Vac. Sci. Technol. B 12(6) 3857 (1994)
- [88] R. R. McKean, U. Schaedeli, S.A. MacDonald, ACS Symp. ser 412, 27 (1989).
- [89] T. Yoshimura, Y. Nakayama, and S. Okazaki, J. Vac. Sci. Technol. B 10(6), 2615 (1992).
- [90] T.H. Fedynyshyn, C.R. Szmanda, R.F. Blacksmith, W.H. Houck, J.C. Root, J. Vac. Sci. Technol. B. 11(6) 2798 (1993).
- [91] W.D. Hinsberg, S.A. MacDonald, N.J. Cleak, C. Snyder, Proc. SPIE 2194 (1994).
- [92] P. Trefonas, M.T. Allen, Proc. SPIE 1872, 74, 1994.
- [93] J. S. Petersen, C.A. Mack, J.W. Thackeray, R. Sinta, T.H. Fedynyshyn, J.M. Morei, J.D. Byers and D.A. Miller, SPIE, Vol 2438, pp153-166, 1995.
- [94] L. Schlegel, T. Ueno, N. Hayashi, T. Iwayanagi, J. Vac. Sci. Technol. B 9 278 (1991).
- [95] S. Schlegel, T. Ueno, N. Hayashi, T. Iwayanagi, Micor. Eng. 11 (1991).

- [96] T. Yoshimura, H. Shiraishi, J. Yamamoto, S. Ozakaki, *Appl. Phys. Lett.* 63, 764, (1993).
- [97] J. Crank, "The Mathematics of Diffusion", New York, NY: Oxford University Press, 1975.
- [98] S. Postnikov, M. Stewart, H. V. Tran, M. Nierode, D. Medeiros, T. Cao, J. Byers, W. Hinsberg, S. Webber, C. G. Willson, to be published in *J. Vac. Sci. Technol.* Nov/Dec 1999.
- [99] R. W. Korsmeyer, S.R. Lustig, N. A. Peppas, *J. Polym. Sci. Phys. Ed.* Vol 24, 395- 408, Feb. 1986.
- [100] H. Fujita, A. Kishimoto, and K. Matsumoto, *Transactions of the Faraday Society*, Vol. 56, 424-437 (1960)
- [101] Y. Lei, E. Croffie, M. Cheng, A. Neureuther, Submitted to *Proc. SPIE* (2001).
- [102] G.M. Schmid, V.K. Singh, L.W. Flanagan, M.D. Stewart, S.D. Burns and C.G. Willson. *Proc. SPIE*, Vol. 3999 pp.675-685. (2000)
- [103] S. Pantas, "Finite Element Methods for Process Simulation Application to Silicon Oxidation", Ph.D. Thesis, Memorandum No. UCB/ERL M88/26, University of California, Berkeley, May 1988
- [104] F. M. Houlihan, T. Wallow, A. Timko, E. Neria, R. Hutton, R. Cirelli, J.M. Kometani, O. Nalamasu, E. Reichmanis, *J. of Photopolymer Sci. & Tech.* 10 (3), 1997
- [105] S. V. Postnikov, M. D. Stewart, H. V. Tran, M. A. Nierode, D. R. Medeiros, T. Cao, J. Byers, S. E. Webber, C. G. Willson, *J. Vac. Sci. Tech. B* 17(6), Nov/Dec 1999

- [106] Horn, M.W.; Maxwell, B.E.; Goodman, R.B.; Kunz, R.R. Journal of Vacuum Science & Technology B, Nov.-Dec. 1996, vol.14, (no.6):4207-11.
- [107] La Tulipe, D.C. Simons, J.P. Seeger, D.E., Proc. of the SPIE vol 2195 (1994) 372-78
- [108] Weib, M. Goethals, M. Microelectronic Engineering 30 (1996) 313-16.
- [109] Simakov, N.N. Mikroelektronika vol. 26 (30) Jan 1997.
- [110] McDonagh, D. Arshak, K. Arshak, A. Proc. of the SPIE vol.2195 (1994) 497-505.
- [111] R. Visser, J. Schellekens, M. Reuhman-Huisken, L Van Ijzendoorn, Proc. SPIE, Vol. 771 111-117 (1987)
- [112] J. Pelka, Microelectronic Engineering, 14, pp.269-281 (1991).
- [113] K. Miller, Lecture Notes for Numerical Solutions of Ordinary Differential Equations (Math 228A), University of California, Berkeley, Fall 1997.
- [114] G. N. Vanderplaats, Numerical Optimization Techniques for Engineering Design, McGraw Hill, New York, 1984.